FZR-427

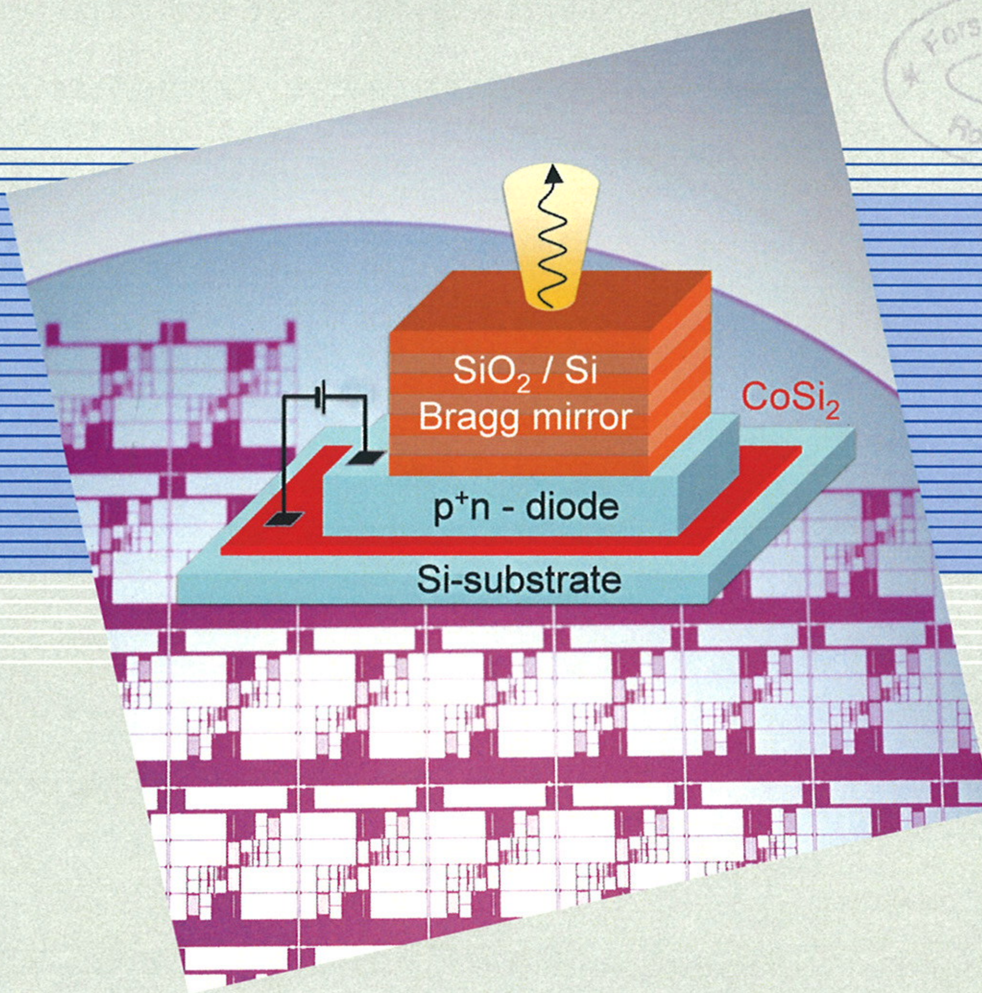

Wissenschaftlich-Technische Berichte
FZR-427 2005 · ISSN 1437-322X

Annual Report 2004

Institute of Ion Beam Physics and Materials Research

Forschungszentrum Rossendorf

Wissenschaftlich-Technische Berichte
FZR – 427
2005

Annual Report 2004

Institute of Ion Beam Physics and Materials Research

Editors:

J. von Borany, V. Heera, M. Helm,
H.-U. Jäger, W. Möller

Forschungszentrum
Rossendorf

Cover Picture:

The front figure shows a schematic sketch of a Si-based microcavity light-emitting diode. The infrared light ($\lambda \approx 1100$ nm) is generated at the boron doped p^+n-junction of the diode. The emission characteristics is determined by the cavity formed by the bottom mirror ($CoSi_2$) and the top Bragg mirror (stack of Si/SiO_2 layers).

For details see contribution at page 9.

Forschungszentrum Rossendorf e.V.
Institut für Ionenstrahlphysik und Materialforschung

Postfach 51 01 19
D-01314 Dresden
Bundesrepublik Deutschland

Direktoren	Prof. Dr. Wolfhard Möller	Prof. Dr. Manfred Helm
Telefon	+ 49 (3 51) 2 60 22 45	+ 49 (3 51) 2 60 22 60
Telefax	+ 49 (3 51) 2 60 32 85	+ 49 (3 51) 2 60 32 85
E-mail	w.moeller@fz-rossendorf.de	m.helm@fz-rossendorf.de

Internet http://www.fz-rossendorf.de/FWI

Preface by the Directors

The Institute of Ion Beam Physics and Materials Research (IIM) contributes to the "Structure of Matter" Research Program at the Forschungszentrum Rossendorf (FZR) with the fields "Ion-based Materials Research" and "Semiconductor Physics". It combines basic research and application-oriented studies in the fields of ion beam applications to materials and semiconductor research, with more than 100 scientists, engineers, technicians, and PhD and diploma students. The institute operates a national and international ion beam center, which, in addition to its own scientific activities, offers services and transfers know-how on ion beam techniques to universities, other research institutes, and industry. It is involved in the scientific exploitation of the new experimental facilities at FZR, the infrared free-electron laser at the 40 MeV superconducting electron accelerator ELBE and the Dresden High Magnetic Field Laboratory (HLD).

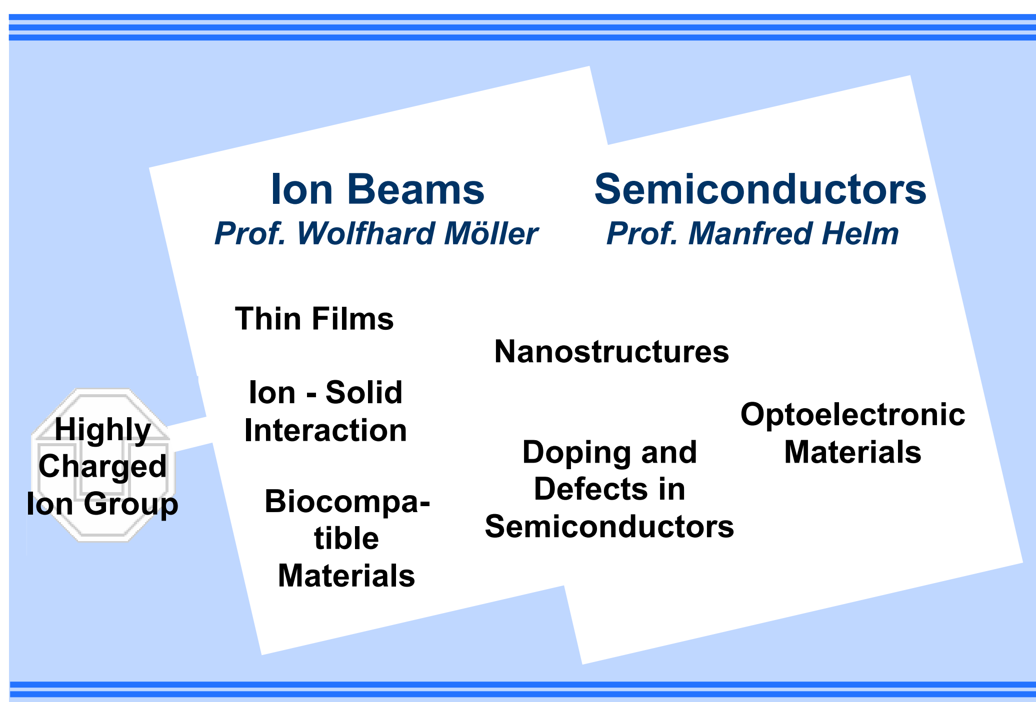

The diagram displays the 2004 R&D topics of the institute. Based on a recommendation by the Scientific Advisory Board of FZR, the topic "Biocompatible Materials" has been closed as an independent activity by the end of November 2004, and will be pursued within the Thin Film topic for cooperations and services only. Within the "Nanostructure" activity, a new group under Dr. habil. Jürgen Fassbender has been established in order to study ion bombardment effects on magnetism on a nanoscale, which also opened new and already fruitful cooperations within the Dresden Materials Research Community. The institute is in particular thankful to Dr. Fassbender as he decided not to accept a recent offer for a professorship at the University of Osnabrück. In contrast, the speaker of the "Optoelectronic Materials" topic and head of the Semiconductor Spectroscopy Division, Dr. Thomas Dekorsy, left the institute in December for a professorship at the University of Konstanz. We would like to thank him for his excellent contributions and the utmost pleasant cooperation during nearly five years, and wish him continued success at his new position.

In the present Annual Report, we hope to demonstrate that the institute has further expanded its scientific outcome as well as its collaborations and services. The number of publications in refereed international journals has been further increased (with a level of about 4.5 publications per scientific staff member in 2004). One patent has been issued, and nine patents have been submitted for approval. Six master or diploma students, and three PhD students finished their theses at the institute.

The institute would like to thank all partners and friends, and the organizations who supported its progress in 2004. Special thanks are due to the Executive Board of the Forschungszentrum Rossendorf, the Minister of Science and Arts of the Free State of Saxony, and the Minister of Education and Research of the Federal Government of Germany. Our partners from universities, industry and research institutes all around the world contribute essentially to the success of the institute, and play a crucial role for its further development. Last but not least, the directors would like to thank all staff of the institute for their active and excellent contributions in 2004.

Prof. Wolfhard Möller Prof. Manfred Helm

Contents

Selected Reports

Page

J. Potfajova, J.M. Sun, S. Winnerl, T. Dekorsy, W. Skorupa, B. Schmidt, M. Helm, S. Mantl and U. Breuer 9
Silicon Based Electrically Driven Microcavity LED

J.M. Sun, W. Skorupa, T. Dekorsy, M. Helm, L. Rebohle and T.Gebel 11
Efficient Ultraviolet Electroluminescence from a Gd-Implanted Silicon Metal-Oxide-Semiconductor Device

N. Georgiev, T. Dekorsy, M. Helm, M.P. Semtsiv, M. Ziegler, S. Dressler and W.T. Masselink 14
Above Room Temperature Operation of Short Wavelength (λ = 3.8 μm) Strain-Compensated $In_{0.73}Ga_{0.27}As$–AlAs Quantum-Cascade Lasers

T. Müller, K.-H. Heinig, W. Möller, C. Bonafos, H. Coffin, N. Cherkashin, G. Ben Assayag, S. Schamm, G. Zanchi, A. Claverie, M. Tencé and C. Colliex 18
Multi-Dot Floating-Gates for Nonvolatile Semiconductor Memories: Their Ion Beam Synthesis and Morphology

J. von Borany, M. Friedrich, M. Rüb, G. Deboy, J. Butschke and F. Letzkus 22
Application of Ultra-High Energy Boron Implantation for Superjunction Power (CoolMOS^{TM}) Devices

A. Rogozin, N. Shevchenko, M. Vinnichenko, F. Prokert, V. Cantelli, A. Kolitsch and W. Möller 26
Real-Time Evolution of the Indium Tin Oxide Film Properties and Structure During Annealing in Vacuum

B. Abendroth, R. Gago, F. Eichhorn and W. Möller 30
X-Ray Diffraction Study of Stress Relaxation in Cubic Boron Nitride Films Grown with Simultaneous Medium-Energy Ion Bombardment

D. Güttler, B. Abendroth, R. Grötzschel, W. Möller and D. Depla 34
Mechanisms of Target Poisoning during Magnetron Sputtering as Investigated by Real-Time in situ Analysis and Collisional Computer Simulation

B. Rellinghaus, O. Dmitrieva, M.O. Liedke and J. Fassbender 38
Ion Beam Induced Destabilization of Icosahedral Structures in Gas Phase Prepared FePt Nanoparticles

Short Contributions

Ion-Solid-Interaction 45

Thin Films 47

Magnetic Films 52

Biocompatible Materials 56

Nanostructures 58

Doping and Defects in Semiconductors 62

Optoelectronic Materials 67

Others 70

Equipment 71

Glossary 72

Statistics

Publications 77

Invited Talks 89

Conference Contributions 91

Lectures 104

Reports / Patents 106

Master / Diploma Theses 107

PhD Theses / Awards 108

Organization of Meetings 108

Laboratory Visits 108

Guests 110

ROBL-MRH Visitors 113

Marie Curie Fellows 115

Colloquium of the Institute 115

Other Seminars 116

Projects 117

Experimental Equipment 120

Services 122

Organigram 124

List of Personnel 125

Selected Reports

Silicon Based Electrically Driven Microcavity LED

J. Potfajova, J.M. Sun, S. Winnerl, T. Dekorsy, W. Skorupa, B. Schmidt, M. Helm, S. Mantl[1] and U. Breuer[1]

[1]*Forschungszentrum Jülich, D-52425 Jülich, Germany*

The realization of Si-based, electrically driven light emitters is a key requirement for the implementation of low-cost Si-based optoelectronics [1]. Realizing Si-based light sources in a process technology compatible with mainstream microelectronics technology is one of the big challenges of semiconductor technology. Due to its indirect bandgap Si has a low radiative recombination rate, leading to efficiencies of the bandgap electroluminescence (EL) in the range of 10^{-6} [2,3]. Recently, different approaches lead to an increase of the power efficiency of the bandgap EL by more than three orders of magnitude up to values of 0.1 % to 1 % [4,5,6]. These approaches are based on pn diodes, where either the non-radiative lifetime is increased by using high-purity float-zone Si, combined with surface texturing to improve the outcoupling efficiency [5], or where specific defects introduced by ion-implantation enhance the radiative recombination rate through carrier confinement effects [4,6]. However, the spectral width and temporal response of these devices still constrains their practical application. One possible route for a further enhancement of the efficiency of these devices is a photonic confinement of the emitting layer. III-V semiconductor based LEDs gained significantly in performance by incorporation into microcavities (MCs) [7]. Planar MCs enhance the brightness, efficiency and directionality of the emission from a high index material and lead to more than an order of magnitude increase in the spectral power density [8]. A MC consists of a cavity with $i \times \lambda_{MC}/2n$ thickness (i: integer, λ_{MC}: resonance wavelength of the MC, n: refractive index of the cavity material) embedded between two highly reflecting mirrors. For III-V LEDs molecular epitaxy growth allows the deposition of Bragg mirrors which act simultaneously as electrical contacts to the active layer. This is a technological problem for Si-based devices, where the Bragg mirrors have to be fabricated from insulating dielectric materials thus inhibiting to electrically drive the active layer. Previously, electrically driven MCs were realized, where the active layer and the Bragg mirror consisted of porous Si [9,10]. These devices suffered from the low stability of porous Si under high-voltage current injection. Here we present a proof-of-principle of an electrically driven MC based on bulk Si as active layer.

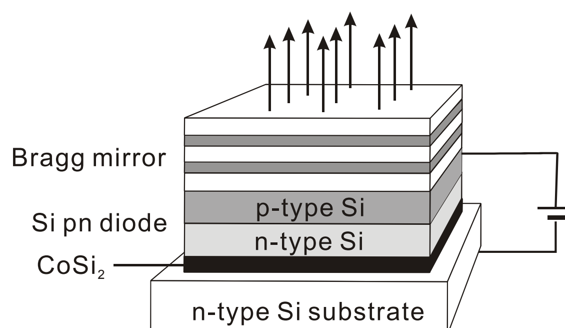

Fig. 1: Schematic sketch of the Si-based microcavity.

The device structure is schematically sketched in Fig. 1. It consists of a buried $CoSi_2$ layer, which acts as the bottom mirror and the bottom electrical contact, the active layer containing the pn diode, and a top Bragg mirror consisting of 2.5 pairs of Si/SiO_2. The $CoSi_2$ layer is formed by ion beam synthesis based on Co^+ implantation into n-doped (100) Si and subsequent annealing (1100°C for 20 s) [11]. The top crystalline Si layer is overgrown using molecular beam epitaxy to a total thickness of 370 nm, corresponding to $1 \times \lambda_{MC}/n$ at a wavelength of 1115 nm. The Si layer is uniformly n-doped (1.8×10^{17} cm^{-3}) by implanting P^+ ions and subsequent annealing. The Si pn diode is formed by B^+ ion implantation (25 keV energy, dose of 4×10^{15} cm^{-2}) and high temperature annealing (1050°C for 10 min) into the MBE grown n-doped Si top layer. An Al ring contact of 1 mm inner diameter is lithographically patterned into the evaporated contact layer. The top Bragg mirror is fabricated by sputter deposition of alternating SiO_2 layers of 185 nm thickness and amorphous Si layers of 75 nm thickness. Locally the top Bragg mirror is removed above the Al ring to contact the diode from the top, while the bottom diode contact is provided through the back to the low resistivity n-type substrate and the $CoSi_2$ layer.

Rather than being diode-like the current-voltage characteristic shows a nearly ohmic

behaviour with a resistivity of approx. 3 Ω. Secondary ion mass spectroscopy of the diode reveals that this is related to B diffusion from the projected range of 60 nm down to the $CoSi_2$ contact probably due to a high defect density of the MBE grown Si layer. Nevertheless, EL is only observed when a forward bias larger than 1.2 V is applied to the diode, as expected for current injection into the pn diode. In comparison to diodes with 0.1 % power efficiency prepared by the same technique on high-quality Si, the EL intensity of devices without top Bragg mirror at the same current densities dropped by two orders of magnitude due to the almost short-circuited pn diode.

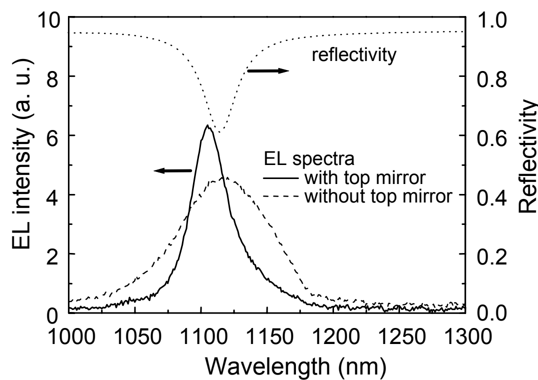

Fig. 2: Electroluminescence spectrum of Si pn diode with (solid line) and without (dashed line) top Bragg mirror. Reflectivity spectrum of the microcavity (dotted line).

Figure 2 depicts the room-temperature EL spectrum of devices without and with Bragg mirror at a current of 500 mA. Additionally the reflectivity spectrum measured within the Al ring contact of a diode is shown, exhibiting the clear signature of a microcavity. The top Bragg mirror has a reflectivity of 94 %. At the position matching λ_{MC} = 1115 nm the reflectivity drops to 60 %. This spectrum agrees with the modeling of the MC using a value of 75 % for the reflectivity of the $Si/CoSi_2$ interface. The bandgap EL spectrum of the device without Bragg mirror shows the same spectrum as previously reported for high-efficiency diodes [4,6]. The linewidth of the spectrum is 84 nm. With the top-Bragg mirror the linewidth is decreased to 35 nm while the peak intensity is significantly increased at λ_{MC}. The maximum of the EL is shifted by 10 nm to lower wavelengths as compared to the dip in the reflectivity spectrum. This shift is within the range of scattering of the reflectivity minimum position over the processed wafer due to non-uniformity of the layer thicknesses in the sputter-deposited Bragg mirror.

We demonstrated a proof-of-principle of an electrically driven Si microcavity LED [12]. Several possibilities for a further improvement of the output of the MC can be envisioned: Due to the B diffusion the pn junction is spread across the MC active layer; the optimum coupling of the light emission into the microcavity mode, is achieved, however, when the pn junction is placed in an antinode of the electric field distribution in the MC. This can be achieved by using rapid thermal annealing after the B^+ implantation, which prevents the strong B diffusion as observed in the present case. Further improvement is expected by better matching of the bottom and top reflectivity of the microcavity, e.g. with a SiO_2/Si_3N_4 top mirror, which allows more accurate balancing the top mirror reflectivity due to the lower refractive index contrast as compared to Si/SiO_2. An improvement of the top Si quality with a longer non-radiative lifetime could be gained by wafer bonding methods. A three dimensional confinement could be achieved by lateral patterning of the active layer of the MC into a photonic crystal structure.

References

[1] L. Canham, Nature, **408** (2000) 411

[2] E.Ö. Sveinbjörnsson, J. Weber, Appl. Phys. Lett. **69** (1996) 2686

[3] V.V. Kveder, E.A. Steinman, S.A. Shevchenko, H.G. Grimmeiss, Phys. Rev. B **51** (1995) 10520

[4] W.L. Ng, M.D. Lourenco, R.M. Gwilliam, S. Ledain, G. Shao, K.P. Homewood, Nature **410** (2001) 192

[5] M.A. Green, J. Zhao, A. Wang, P.J. Reece, M. Gal, Nature **412** (2001) 805

[6] J.M. Sun, T. Dekorsy, W. Skorupa, B. Schmidt, M. Helm, Appl. Phys. Lett. **83** (2003) 3885

[7] H. Benisty, H. De Neve, C. Weisbuch, IEEE J. Quantum Electron. **34** (1998) 1612

[8] N.E.J. Hunt, E.F. Schubert, R.A. Logan, G.J. Zydzik, Appl. Phys. Lett. **61** (1992) 2287

[9] M. Araki, H. Koyama, N. Koshida, Appl. Phys. Lett. **69** (1996) 2956

[10] S. Chan, P.M. Fauchet, Appl. Phys. Lett. **75** (1999) 274

[11] S. Mantl, Mater. Sci. Rep. **8** (1992) 1

[12] J. Potfajova, J.M. Sun, S. Winnerl, T. Dekorsy, W. Skorupa, B. Schmidt, M. Helm, S. Mantl, U. Breuer, Electron. Lett. **40** (2004) 904

Efficient Ultraviolet Electroluminescence from a Gd-Implanted Silicon Metal-Oxide-Semiconductor Device

J.M. Sun, W. Skorupa, T. Dekorsy, M. Helm, L. Rebohle[1] and T. Gebel[1]

[1]*Nanoparc GmbH, Dresden, Germany*

Light sources operating in the ultraviolet (UV) region are required for a number of applications, including solid-state lighting, biological agent detection, sterilization and covert communication. Strong UV light emission from AlGaN based emitters has been reported emitting in the UV range from 265-325 nm [1-3]. However, for the development of micro-light sources for on-chip analysis, such as bio-chips, biosensors, micro fluorescent displays etc., efficient silicon based micro-light sources are required which can be integrated into silicon integrated circuits. Silicon based UV light emitters are promising for such applications. Recently, light emitters incorporating rare earth Er^{3+}, Tm^{3+}, Tb^{3+} and Ce^{3+} doped Si-rich SiO_2 have been reported with emission in the infrared to blue-green spectral regions [4,5]. Strong blue-violet emission at 390 nm has been reported in Ge^+ implanted SiO_2 MOS structures [6]. Efficient silicon based UV light emitters at shorter wavelength from silicon device have not yet been reported for the time being. In this paper, we demonstrate a silicon based efficient UV light emitter based on a SiO_2:Gd MOS structure delivering a sharp emission peak at 316 nm from Gd^{3+} ions, which is comparable to the efficient UV emission of ZnF_2:Gd [7]. External quantum efficiencies above 1% are achieved with not fully optimized devices. Device sizes below 1 µm can be easily achieved with standard MOS technology.

Electroluminescence (EL) devices are prepared by standard silicon CMOS technology on 4-inch n-type silicon wafer with resistivity of 2-5 Ωcm. The structure consists of an active gate oxide area surrounded by a field oxide (1 µm). The active layer is a 100 nm thick thermally grown SiO_2 layer implanted with Gd^+ ions at two energies of 50 and 110 keV with doses of 5×10^{14} and $1 \times 10^{15}\ cm^{-2}$, respectively. After annealing at 800°C for 1 hour, a plasma treatment was performed in a mixture of oxygen/hydrogen (90/10) for 5 min. The gate electrode consists of a 100 nm thick indium-tin-oxide deposited by RF sputtering. Various shapes of MOS structures with different feature sizes in the range of 1 to 500 µm were fabricated for testing the function of the EL devices in dependence on the geometry.

EL spectra were measured on a MOS structure with 500 µm diameter with a constant current supplied by a sourcemeter (Keithley 2410). EL signals were recorded at room temperature with a monochromator and a photomultiplier. The absolute EL power from the device was measured using a calibrated optical power meter. The external EL power efficiency is calculated by integrating the total EL output power from the front surface. Photoluminescence (PL) and photo-luminescence excitation (PLE) spectra were also measured with the same system using UV excitation from a 75 W Xe lamp.

Figure 1 shows the PL and PLE spectra from the SiO_2:Gd gate oxide without ITO electrode on top. The PL spectrum under the excitation of 195 nm UV light shows a sharp peak at 316 nm arising from the transition of $^6P_{7/2}$ to $^8S_{7/2}$ of the Gd^{3+} ions [8]. The PLE spectrum of the 316 nm emission exhibits two excitation peaks at 195 and 274 nm. The peak at 195 nm corresponds to the excitation from $^8S_{7/2}$ to $^6G_{13/2}$ and the peak at 274 nm can be assigned to the $^8S_{7/2}$ to ^6I_J excitation of Gd^{3+} [9].

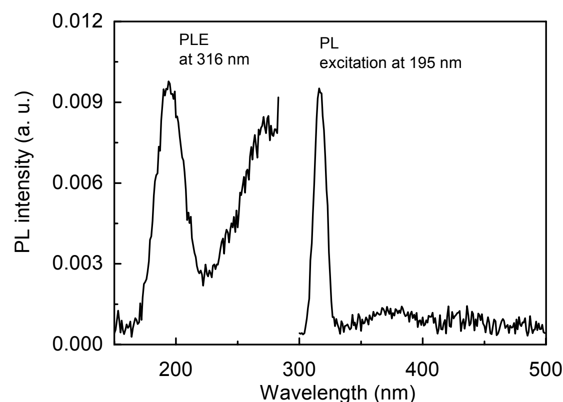

Fig. 1: PL and PLE spectra from the 100 nm SiO_2:Gd layer. The PL was excited by 195 nm UV light, and the PLE was measured with a detection wavelength of 316 nm.

Figure 2 shows the EL spectra of the SiO_2: Gd at an injection current of 100 µA for the MOS structure with a diameter of 500 µm. The spectra show a strong peak at 316 nm from the transition of the lowest excited states of $^6P_{7/2}$ to $^8S_{7/2}$ from the Gd^{3+} ions. Two broad peaks in the visible

range centered at 460 nm and 650 nm are observed at higher current injection, as shown in the insert. These bands have an intensity about three orders of magnitude lower than the 316 nm peak at the same injection current. The bands originate from neutral oxygen vacancies and non-bridging oxygen hole centers (NBOHCs) as typical network defects of the amorphous silicon dioxide created by the implantation process [10,11].

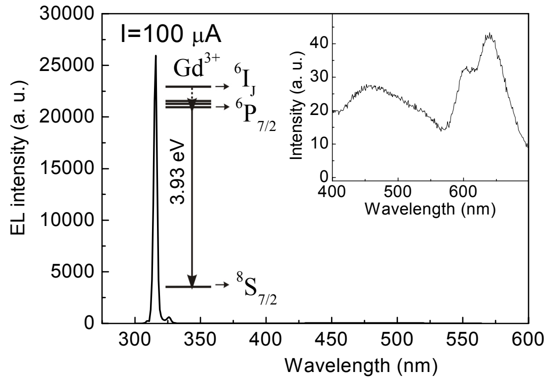

Fig. 2: EL spectrum of the SiO_2:Gd MOS device at 100 μA current and a sketch of the involved electronic transition. The inset shows the emission in the 400 nm to 700 nm region. Note that the intensity in this region is nearly three orders of magnitude lower than the emission at 316 nm.

In order to clarify the excitation process of the UV emission, we analyze the current-field characteristics of the device as shown in Fig. 3. The ratio of the injection current density and the square of the electric field, i.e. J/E^2, is plotted versus the reciprocal of the electric field which allows us to verify Fowler-Nordheim (F-N) tunneling injection of hot electrons at SiO_2/Si interface in the MOS structure expressed as $J/E^2 = A\ exp(-B/E)$, where A and B are constants [12]. This expression is valid in the range from 8.5 MV/cm to 10.3 MV/cm. The insert shows the EL intensity of the 316 nm peaks from Gd^{3+} as a function of the injected current of the MOS device. An external quantum efficiency of 1% is obtained for this device (with a power efficiency of 4-6×10^{-4}). The threshold electric field for detection of the UV is about 8.5 MV/cm, which is the same as the threshold electric field for F-N tunneling injection of the hot electrons into the conduction band of the SiO_2 for strong electric heating. According to the study of DiMaria et al. [13], under such high electric fields of 8.5-11 MV/cm as necessary for the operation of our devices, the average hot electron energy is above 4 eV with respect to the bottom of the conduction band edge of SiO_2; the average energy of the hot electrons is larger than the EL photon energy of 3.93 eV. Hence a large number of hot electrons are capable of generating efficiently UV light from Gd^{3+} by impact excitation in the SiO_2 host.

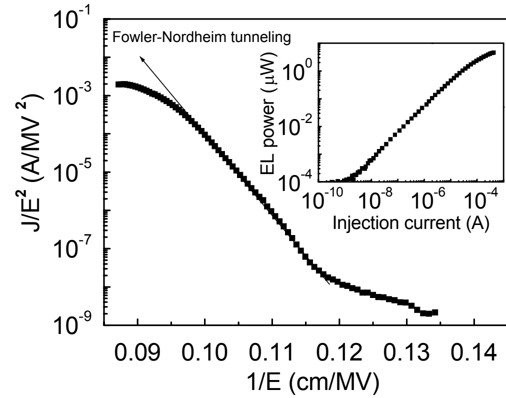

Fig. 3: The current density of the SiO_2:Gd MOS device divided by the squared electric field is plotted vs. the reciprocal electric field (Fowler-Nordheim plot of the current-field characteristic).The inset is the integrated EL power vs. the injection current.

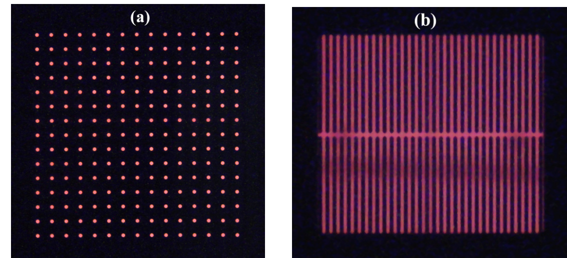

Fig. 4: CCD photograph of the EL from two different structures, (a) matrix of 15 × 15 dots with a diameter of 20 μm and spacing of 70 μm, (b) comblike structure with an EL strip width of 4 μm. Note the observed visible light is 2000 times weaker than the UV peaks, which is not observed by the CCD camera.

Figure 4 shows a matrix of 15 × 15 devices of a 20 μm diameter MOS structure operated with a total injection current of 100 μA and a high resolution comblike structure with EL strips of 4 μm width, both imaged with a Si CCD camera under a optical microscope. Note that only the visible part of the spectrum from the SiO_2 defect EL is observed, which is nearly three orders of magnitude weaker than the UV light. The smallest feature size is 2 μm which is limited by the capability of our lithography system. However, smaller sizes below 1 μm are possible for high-resolution display or biochip applications. Combination with R-G-B phosphors, efficient silicon-based UV light emitters can be better candidates for the fabrication of high-resolution full-color microdisplays as compared to ZnF_2:Gd thin-film EL devices, since the fabrication of silicon–based devices is fully compatible with standard MOS technology.

In summary, strong ultra-violet electroluminescence with external quantum efficiency above 1% was reported from an indium-tin oxide/ SiO_2:Gd/Si MOS structure for the first time [14]. The UV EL is generated by impact excitation of Gd^{3+} ions by hot electrons. External quantum efficiencies above 1% were obtained with room temperature for further optimization by changing the oxide thickness and Gd concentration. EL devices on a micrometer-scale can be fabricated employing standard CMOS technology.

Acknowledgements

The authors would like to thank I. Winkler and J. Schneider for the ion implantation, H. Felsmann, C. Neisser, and G. Schnabel for the processsing of the MOS structures.

References

[1] A.J. Fischer, A.A. Allerman, M.H. Crawford, K.H.A. Bogart, S.R. Lee, R.J. Kaplar, W.W. Chow, S.R. Kurtz, K.W. Fullmer, J.J. Figiel, Appl. Phys. Lett. **84** (2004) 3394

[2] A. Yasan, R. McClintock, K. Mayes, D. Shiell, L. Gautero, S.R. Darvish, P. Kung, M. Razeghi, Appl. Phys. Lett. **83** (2003) 4701

[3] A. Chitnis, J.P. Zhang, V. Adivarahan, M. Shatalov, S. Wu, R. Pachipulusu, V. Mandavilli, M.A. Khan, Appl. Phys. Lett. **82** (2003) 2565

[4] M.E. Castagna, S. Coffa, M. Monaco, A. Muscara, L. Caristia, S. Lorenti, A. Messina, Mat. Res. Soc. Symp. Proc. **770** (2003) I2.1.1

[5] S.Y. Seo, J.H. Shin, B.S. Bae, N. Park, J.J. Penninkhof, A. Polman, Appl. Phys. Lett. **82** (2003) 3445

[6] L. Rebohle, J. von Borany, R.A. Yankov, W. Skorupa, I.E. Tyschenko, H. Fröb, K. Leo, Appl. Phys. Lett. **71** (1997) 2809

[7] T. Senda, Y.-J. Cho, T. Hirakawa, H. Okamoto, H. Takakura, Y. Hamakawa, Japan. J. Appl. Phys. (Part 1) **39** (2000) 4716

[8] N. Miura, T. Sasaki, H. Matsumoto, Japan. J. Appl. Phys. (Part 2) **30** (1991) L1815

[9] R.T. Wegh, H. Donker, A. Meijerink, R.J. Lamminmäki, J. Hölsä, Phys. Rev. B **56** (1997) 13841

[10] L. Rebohle, J. von Borany, H. Fröb, W. Skorupa, Appl. Phys. B **70** (2000) 1

[11] A.N. Trukhin, M. Goldberg, J. Jansons, H.-J. Fitting, I.A. Tale, J. Non-Cryst. Solids **223** (1998) 114

[12] J.A. Lopez-Villanueva, J.A. Jimenez-Tejada, P. Cartujo, J. Bausells, J.E. Carceller, J. Appl. Phys. **70** (1991) 3712

[13] D.J. DiMaria, T.N. Theis, J.R. Kirtley, F.L. Pesavento, D.W. Dong, S.D. Brorson, J. Appl. Phys. **57** (1985) 1214

[14] J.M. Sun, W. Skorupa, T. Dekorsy, M. Helm, L. Rebohle, T. Gebel, Appl. Phys. Lett. **85** (2004) 3387

Above Room Temperature Operation of Short Wavelength (λ = 3.8 μm) Strain-Compensated $In_{0.73}Ga_{0.27}As$–AlAs Quantum-Cascade Lasers

N. Georgiev, T. Dekorsy, M. Helm, M.P. Semtsiv[1], M. Ziegler[1], S. Dressler[1] and W.T. Masselink[1]

[1]*Department of Physics, Humboldt-Universität of Berlin*
Newtonstrasse 15, D-12489 Berlin, Germany

Since their first realization, quantum-cascade lasers (QCLs) [1] have been demonstrated with emission wavelengths between 3.5 μm [2] and 100 μm [3]. The range of demonstrated room-temperature operation is somewhat smaller, being 4.5–16 μm [1]. Operation within the atmospheric window in the band between 2.9 and 5.3 μm is interesting for gas detection because a large number of molecules (e.g., NO, CO, CO_2, CH_2O, and SO_2) have characteristic absorption in this band. QCL operation in this band, especially near room temperature, remains challenging: Short wavelength emission requires a large conduction band discontinuity and narrow wells. Furthermore, the ability to operate the laser at higher temperatures requires that the conduction band edge in the barrier material lies much higher in energy than the upper lasing level to inhibit the thermally activated escape of carriers into the quasicontinuum. QCL materials with very high conduction band discontinuities [4] have been successfully used for lasers emitting at longer wavelength, but operation at short wavelengths and at higher temperatures have not yet been reported. The shortest wavelength QCLs to date have been demonstrated in the strain-compensated InP-based InGaAs/InAlAs system [2].

Within this system, the largest *Γ*-valley conduction band discontinuity can be reached using AlAs as the barrier. Already the introduction of thin AlAs blocking layers into a lattice-matched $In_{0.53}Ga_{0.47}As$-$In_{0.52}Al_{0.48}As$ design improves the temperature performance of a 5 μm QCL [5]. The use of pure AlAs barriers throughout the active region is more difficult due to its large lattice mismatch to InP. Recently we have successfully demonstrated the growth of and short-wavelength intersubband transitions in short-period $In_xGa_{1-x}As$-AlAs strain-compensated superlattices [6]. This letter describes the design and performance of an $In_{0.73}Ga_{0.27}As$-AlAs QCL with both short laser emission wavelength and high operation temperature.

The laser structure (HU1507) was grown using gas-source molecular-beam epitaxy (GSMBE) on a low-doped ($n = 2 \times 10^{17}$ cm^{-3}) InP:Sn substrate which also serves as a lower cladding layer. The epitaxy sequence consists of: 220 nm $In_{0.52}Ga_{0.48}$As:Si ($n = 5 \times 10^{16}$ cm^{-3}); then the 1.4 μm (total thickness), 30 periods active region; 220 nm $In_{0.52}Ga_{0.48}$As:Si ($n = 5 \times 10^{16}$ cm^{-3}); an 18 nm $In_{0.52}Ga_{0.48}$As:Si-$In_{0.52}Al_{0.48}$As:Si four-periods graded superlattice; then a 2.5 μm ($n = 1 \times 10^{17}$ cm^{-3}) InP:Si plus 0.8 μm ($n = 4 \times 10^{18}$cm^{-3}) InP:Si top cladding layer; and finally a 130 nm $In_{0.52}Ga_{0.48}$As:Si ($n = 1 \times 10^{19}$ cm^{-3}) top contact layer.

One period of the active region is illustrated and described in Fig. 1. The use of two-component $In_{0.55}Al_{0.45}$As-AlAs barriers in addition to pure AlAs barriers in the laser core allows us to tune the barrier thicknesses and the net strain almost independently. This solution provides an additional degree of flexibility in the band structure engineering in strain-compensated systems.

Figure 1 depicts the *Γ*-valley conduction band edge profile within a single period of the active region under an electric field of 76 kV/cm along with the calculated probability functions for confined electronic states. The confined state wave functions are obtained [7] within an effective mass approximation; to account for band nonparabolicity, we used an energy-dependent effective mass after Nelson et al. [8].

The lowest indirect valley in the described system of materials is the *L* valley in $In_{0.73}Ga_{0.27}$As. Its energy (indicated with a dashed line on Fig. 1) approximately coincides with the *Γ*-valley minimum in $In_{0.55}Al_{0.45}$As [9,10], which is ≈ 90 meV above the upper lasing state, ***2***. This energetic separation, corresponding to almost three LO phonon energies, is sufficient to effectively suppress thermally-activated *Γ*–*L* intervalley carrier leakage near room temperature.

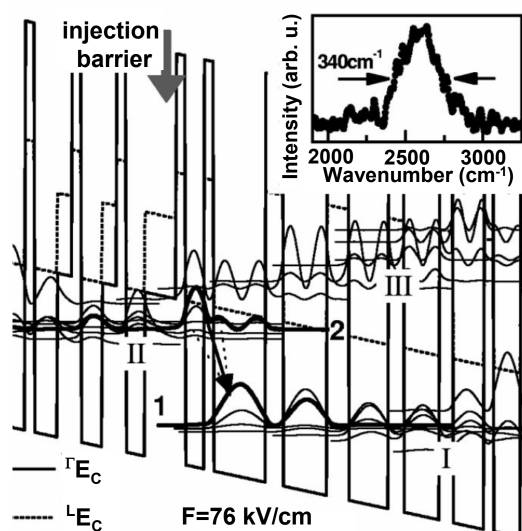

Fig. 1: Conduction band diagram and probability functions calculated within a single period of the active region with a 76 kV/cm electric field. The layer thickness in nm from left to right starting from the injection barrier (indicated by the bold straight arrow) are: 3.0/ **0.9**/ 1.8/ **0.9**/ 5.0/ **1.7**/ 4.2/ **2.1**/ 3.8/ **1.5**/ 3.4/ **1.3**/ 3.0/ **0.9**/ 2.6/ **0.9**/ 2.2/ *1.4*/ **0.9**/ 2.0/ *1.4*/ **0.9**/ 1.8. AlAs layers are in bold, $In_{0.73}Ga_{0.27}As$ layers are in roman, and $In_{0.55}Al_{0.45}As$ layers are in italics. Underlined layers are doped to 5×10^{17} cm^{-3}. The moduli square of the wave functions (***1*** and ***2***) responsible for the strongest laser transition are drawn with the thick lines. The inset shows a below-threshold electroluminescence spectrum of a 39 μm × 2 mm laser bar at 8 K.

The design of the active region is similar to the bound-to-continuum approach pioneered by Faist et al. [11], but the injection barrier is thinner (3.9 nm) than in a typical bound-to-continuum design. The consequence is that some states of the injector miniband *II* (separated by 1–10 meV from the upper lasing state ***2***) also spatially overlap with the lower lasing state ***1***. At 76 kV/cm, the dipole matrix elements of the resulting "parasitic" transitions (dashed arrows on Fig. 1) are as high as 0.29 nm, comparable to the 0.47 nm matrix element of the principal ***2***-to-***1*** transition (solid arrow on Fig. 1). These multiple transitions result in a broad gain spectrum, as reflected in the broad electroluminescence (inset in Fig. 1). Despite the broad gain, the design allows population inversion for more than one transition due to the high injection efficiency into the upper lasing states, the low carrier leakage into the miniband *III* and into the indirect valleys, and the diagonal character of the lasing transitions.

The grown structure was processed into a series of 28–44 μm-wide ridges using a combination of chemically assisted ion beam etching (CAIBE) and wet-chemical etching techniques. The substrate was thinned to 100 mm. Ti/Pt/Au contacts were then deposited on the top of the ridge and the bottom of the substrate and alloyed for 2 min at 430°C. The laser bars were then electrically insulated with bisbenzocyclobutene (BCB). Approximately 16-μm-wide windows were opened on the top of the ridges and 1–2 μm of gold was deposited on the insulated laser bars for electrical contact between the ridge and contact pad. Laser bars with length 1.5 and 2 mm were cleaved and mounted, epilayer up, on Au-plated copper submountings. The cleaved facets were left uncoated.

Processed laser bars were characterized using 100 ns current pulses at a repetition rate of 5 kHz. The lasers emit in the 3.7–4.2 μm spectral range; the shortest laser emission observed is 3.74 μm at 8 K for the 39 μm × 2.0 mm laser bar. For the 28 μm × 2.0 mm laser bar and at 8 K, the threshold current was 0.48 A (860 A/cm^2) with maximum peak power of 6 W per facet; at room temperature the threshold current density was 4.8 kA/cm^2 and the maximum peak power 240 mW per facet. Laser operation was achieved up to 330 K.

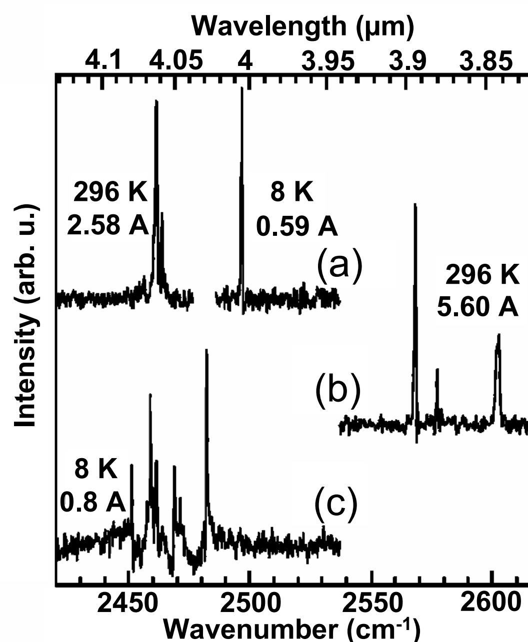

Fig. 2: High-resolution Fourier-transform emission spectra from (a) 34 μm × 1.5 mm; (b) 39 μm × 2.0 mm; and (c) 28 μm × 2.0 mm lasers at different heat-sink temperatures and currents, as indicated. The differing stripe lengths and widths are obtained from different locations from a 2 in. wafer.

Figure 2 shows high-resolution Fourier-transform spectra measured in the step-scan mode from three different laser-bars at a variety of temperatures and currents. Due to the narrow (3.9 nm) injection barrier, our design allows multi-wavelength operation, similar to the superlattice active-region design [1]. At currents just above threshold, only one transition has enough gain to lase; this primary emission from different laser

bars varies by up to 200 cm^{-1} due to a gradient of layer thickness across the 50 mm wafer. As the current is increased, first additional resonator modes separated from another by about 1 cm^{-1} appear and then, at the highest currents, other wavelengths due to the parasitic transitions described above and separated from the main transition by 20–40 cm^{-1} appear. The resulting laser mode structure [single mode, multimode (Fig. 2(a))], or multi-wavelength [Figs. 2(b) and 2(c)] depends on the drive current and temperature. Both single-color and multi-color operation modes are observed in all tested laser bars. We attribute the lasing at different wavelengths within the same structure to the different transitions depicted in Fig. 1 which are also responsible for the broader electroluminescence. X-ray diffraction spectra of the laser structure show sharp and well-defined satellites characteristic of high-quality material with little variation in periodicity; even so, sub-monolayer variations between different cascades would not be evident and could also result in lasing at different wavelengths.

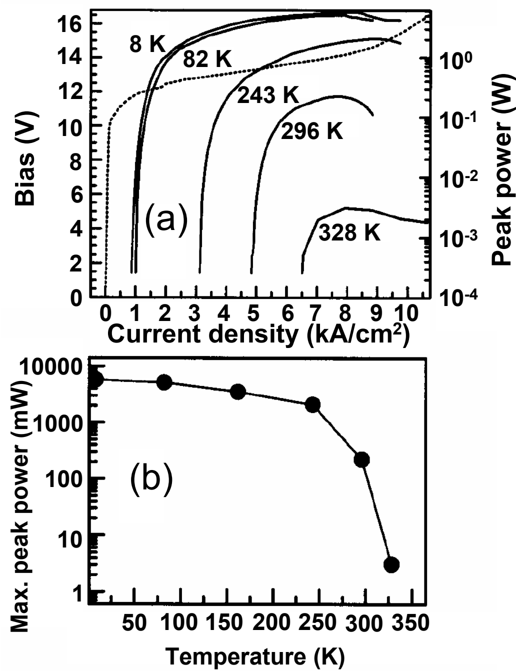

Fig. 3: (a) Pulsed optical power collected from a single facet of a 28 μm × 2 mm laser bar vs. current density at a number of heat-sink temperatures as indicated on figure. (The data have been corrected to account for the 40 % collection efficiency.) The dotted curve shows the current–voltage characteristic at a $T = 8$ K heat-sink temperature. The laser threshold bias ranges between 10.6 and 11.9 V for different temperatures, (b) maximal peak optical power collected from a single facet of a 28 μm × 2 mm laser bar vs. heat-sink temperature.

Figure 3 shows the optical output power performance of a 28 μm × 2 mm laser bar [see Fig. 2(c)] together with the low-temperature current-voltage (*I–V*) characteristics. At about 14 V bias (100 kV/cm electrical field) the *I–V* curve has a kink toward higher differential resistance which is accompanied by a drop in the optical output power. Our calculations show that even at 100 kV/cm the upper level remains well coupled to miniband *II* because the injection barrier is so thin. The drop in laser efficiency at high fields is due to the decoupling of the lower laser level ***1*** from the miniband *I* which reduces the extraction efficiency out of level ***1***.

As seen in Fig. 3(a), output power increases dramatically for current density between 840 and 920 A/cm^2 at 8 K. At 860 ± 20 A/cm^2 the output power is 1/4 mW per facet and is taken as the threshold current density. The threshold current densities (J_{th} = 860 A/cm^2 at 8 K) are the lowest values reported to date for QCLs emitting in the 3.5–5.0 μm spectral range and comparable to the best results at somewhat longer wavelengths [12]. An increased number of cascades could, of course, even further reduce J_{th}, with the threshold power density ($J_{th} \times V_{th}$) remaining approximately constant [1]. The measured threshold power density is 10 kW/cm^2 at 8 K and 43 kW/cm^2 at 273 K, among the lowest reported for this emission wavelength range.

Maximum peak power [Fig. 3(b)] at T = 296 K is 240 mW per facet, which is already sufficient for gas-sensing applications. This performance at room temperature is achieved through the incorporation of the AlAs barriers even without advanced heat-sinking technology (e.g., buried heterostructure, epilayer-down mounting [12], etc.). At temperatures above 300 K, the power decreases rapidly [Fig. 3(b)] due to the thermally activated carrier losses from the upper lasing state via scattering into the miniband *III* and into the *L* valleys of the $In_{0.73}Ga_{0.27}As$, and the thermal backfilling of the lower lasing state ***1***.

The characteristic temperature is measured to be T_0 = 119 K from the dependence of threshold current density on heat-sink temperature as depicted in Fig. 4. High T_0 is possible because of the high barriers as well as high indirect (*L*) valleys in the $In_{0.73}Ga_{0.27}As$ well. An advantage of the current design is that both of these conditions for high T_0 are simultaneously achievable. The measured output power implies efficiencies as high as 40% per cascade at low temperatures.

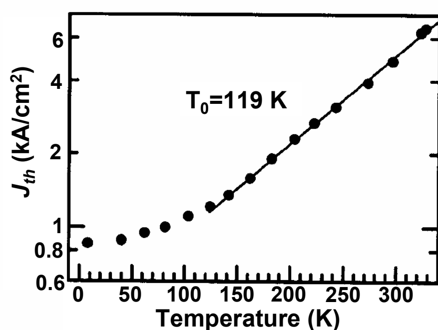

Fig. 4: Threshold current density, J_{th}, vs heat sink temperature for a 28 μm × 2 mm laser ($\lambda \approx$ 4.0 μm) in pulsed operation. The solid line is an exponential fit in the 140–328 K temperature range used to determine T_0. At a heat-sink temperature of 8 K, J_{th} = 0.860 kA/cm^2.

To conclude, we have demonstrated the design and implementation of a quantum-cascade laser emitting between 3.7 and 4.2 μm [13]. The design is based on strain-compensated $In_{0.73}Ga_{0.27}As$-AlAs on InP. At 8 K threshold current densities as low as J_{th} = 860 A/cm^2 are obtained. Laser operation in pulsed mode is achieved up to a temperature of 330 K with maximum single-facet output peak powers of 6 W at 8 K and of 240 mW at 296 K. At the same time, the large conduction-band discontinuity between the strained AlAs in the barrier and the strained $In_{0.73}Ga_{0.27}As$ well [7] allows short-wavelength laser emission.

Acknowledgements

The authors are grateful to Fraunhofer-Institut für Nachrichtentechnik Heinrich-Hertz-Institut, Berlin, for the chemical processing facilities; and to Dr. U. Müller for fruitful discussions. We are grateful to Deutsche Forschungsgemeinschaft for financial support within the “Forschergruppe 394.”

References

[1] C. Gmachl, F. Capasso, D.L. Sivco, A.Y. Cho, Rep. Prog. Phys. **64** (2001) 1533

[2] J. Faist, F. Capasso, D.L. Sivco, A.L. Hutchinson, S.-N.G. Chu, A.Y. Cho, Appl. Phys. Lett. **72** (1998) 680

[3] B.S. Williams, S. Kumar, H. Callebaut, Q. Hu, J.L. Reno, Appl. Phys. Lett. **83** (2003) 2124

[4] K. Ohtani, H. Ohno, Jpn. J. Appl. Phys., Part 2 **41** (2002) L1279

[5] Q.K. Yang, C. Mann, F. Fuchs, R. Kiefer, K. Köhler, N. Rollbühler, H. Schneider, J. Wagner, Appl. Phys. Lett. **80** (2002) 2048

[6] N. Georgiev, T. Dekorsy, F. Eichhorn, M. Helm, M.P. Semtsiv, W.T. Masselink, Appl. Phys. Lett. **83** (2003) 210

[7] Used parameters: the Γ-valley conduction-band discontinuity for $In_{0.73}Ga_{0.27}As$/AlAs and $In_{0.73}Ga_{0.27}As$/ $In_{0.55}Al_{0.45}As$ are 1.38 and 0.55 eV; the effective mass at the bottom of Γ valley and the nonparabolicity parameters for $In_{0.73}Ga_{0.27}As$, $In_{0.55}Al_{0.45}As$, and AlAs are: (0.035, 0.070, and 0.150) × m_0 and (12.8, 3.5, and 0.9) × 10^{-19} m^2.

[8] D.F. Nelson, R.C. Miller, D.A. Kleinman, Phys. Rev. B **35** (1987) 7770

[9] C.G. Van de Walle, Phys. Rev. B **39** (1989) 1871

[10] I. Vurgaftman, J.R. Meyer, L.R. Ram-Mohan, J. Appl. Phys. **89** (2001) 5815

[11] J. Faist, M. Beck, T. Aellen, E. Gini, Appl. Phys. Lett. **78** (2001) 147

[12] B. Ishaug, W.-Y. Hwang, J. Um, B. Guo, H. Lee, C.-H. Lin, Appl. Phys. Lett. **79** (2001) 1745

[13] M.P. Semtsiv, M. Ziegler, S. Dressler, W. T. Masselink, N. Georgiev, T. Dekorsy, M. Helm, Appl. Phys. Lett. **85** (2004) 1478

Multi-Dot Floating-Gates for Nonvolatile Semiconductor Memories: Their Ion Beam Synthesis and Morphology

T. Müller, K.-H. Heinig, W. Möller, C. Bonafos[1], H. Coffin[1], N. Cherkashin[1], G. Ben Assayag[1], S. Schamm[1], G. Zanchi[1], A. Claverie[1], M. Tencé[2] and C. Colliex[2]

[1]nMat Group, CNRS/CEMES, Toulouse, France [2]Université Paris-Sud-UMR 8502, Orsay, France

Metal-oxide-silicon field-effect transistors with an electrically isolated ("floating") gate layer embedded in the gate oxide are currently used as flash memories. The replacement of this floating-gate by a layer of discrete Si nanocrystals (NCs) [1] improves the performance of flash memories substantially [2]. The reduced probability for a complete discharging of the multi-dot floating-gate by oxide defects allows thinner tunnel oxides. In turn, this floating-gate will be charged/discharged by quantum mechanical direct electron tunneling (instead of defect-generating Fowler–Nordheim tunneling). The memory operation voltage can be reduced and scalability is improved. Using ion beam synthesis, the multi-dot floating-gate can be fabricated along with standard (CMOS) processing [3]. Si^+ ions are implanted at ultralow energies into the gate oxide, causing there a high Si supersaturation. During postimplantation annealing, this Si supersaturation leads to phase separation of elemental Si from SiO_2 [4]. Imaging this phase separation process is difficult. Transmission electron microscopy (TEM) has historically suffered from weak Z contrast between Si and SiO_2 phases. Recently, this problem was partially overcome by Fresnel imaging using under-focused bright field conditions [5]. Thus, the distance of the layer of phase separated Si from the transistor channel could be determined [6,7]. However, this technique fails to resolve the morphology of the phase separated Si. For instance, recent kinetic Monte Carlo (KMC) simulations of phase separation predict a pronounced fluence dependence of the precipitate morphology [4]. For low Si^+ fluences, spherical and isolated Si NCs form by nucleation and growth, while for higher Si^+ fluences spinodal decomposition occurs. The elongated, non-spherical Si structures, formed by spinodal decomposition, coalesce at even higher fluences to an interconnected, labyrinthine Si network. This investigation uses a scanning TEM (STEM) with an efficient parallel electron energy loss spectroscopy (PEELS) system, to confirm the predictions of the KMC simulations. The contrast problem of conventional TEM could be overcome by mapping Si plasmon losses, which differ from SiO_2. Comprehensive KMC studies and PEELS-STEM analysis have been performed to understand the complex process of phase separation in a thin buried layer.

To form Si NCs by phase separation, Si^+ ions have been implanted at 1 keV energy into 10 nm thick SiO_2 layers, which were thermally grown on (001) Si substrates. Using an AXCELIS GSD-ULTRA ultralow-energy implanter, fluences of 5×10^{15}, 1×10^{16}, and $2 \times 10^{16}\,cm^{-2}$ were implanted at room temperature. Surface charging due to implantation was compensated by a Xe plasma electron flood gun. The implanted samples were cleaned using a piranha solution and furnace annealed for 30 min in N_2 at 950°C. From all samples, cross sectional and plane view TEM specimens were prepared by the standard procedure of grinding, dimpling, and Ar^+ ion beam thinning. PEELS-STEM was performed on plane view samples using a scanning TEM VG-HB 501 operating at 100 kV that is equipped with a field emission cathode and a parallel Gatan 666 EELS spectrometer. Low-loss EELS spectra were recorded at each picture point, hence a spectrum image was acquired [8]. These spectra were fitted in the energy range of 15–30 eV by a weighted sum of two plasmon reference spectra, which were obtained from bulk Si and SiO_2. Potential size effects like shifts of the Si plasmon resonance of small Si NCs were not compensated. The gray level of the PEELS-STEM image pixels is given by the ratio of the intensity of the Si plasmon peak and the total intensity of the Si and SiO_2 plasmon peaks and, therefore, maps the Si bulk plasmons. Quantitative Si concentrations, however, cannot be given, only the relative Si content is imaged. In Fig. 1, such Si plasmon maps (on the left-hand side) are compared to plane view snapshots of KMC simulations (on the right-hand side). This atomistic approach to phase separation of excess Si in thin SiO_2 layers by atomistic simulations was recently described in detail in Refs. 4 and 9. The depth profiles of excess Si due to high fluence Si^+ ion implantation into thin gate oxides have been calculated by the binary collision program TRIDYN [10] accounting for the effects of ion erosion, target swelling, and ion beam mixing dy-

namically. The postimplantation phase separation during thermal treatment is described by a kinetic three-dimensional lattice Monte-Carlo program package [11,12].

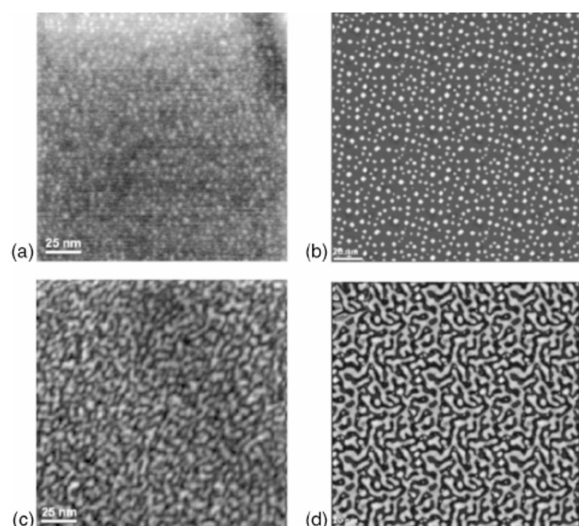

Fig. 1: Morphology of phase separated Si in SiO_2. Si plasmon maps by PEELS-STEM (a), (c) are compared to corresponding KMC simulations (b), (d). Nucleation of Si NCs is observed (a) for a Si fluence of $1 \times 10^{16}\,cm^{-2}$ and predicted with the same morphology for (b) $3 \times 10^{15}\,cm^{-2}$. Spinodal patterns are imaged (c) for $2 \times 10^{16}\,cm^{-2}$ and simulated (d) for $8 \times 10^{15}\,cm^{-2}$. Bright and dark regions correspond to Si and SiO_2 phases, respectively.

Taking the TRIDYN profiles of Si excess as well as Si solubility and diffusivity in SiO_2 as input, the program describes excess Si diffusion, precipitation, and Ostwald ripening in the thin SiO_2 layer under the constraints of the boundary conditions of a nearby Si / SiO_2 interface and a free SiO_2 surface. Here, we use a simplified version of the KMC program, i.e., only Ising-type nearest-neighbor interactions. It should be noted that KMC simulations with measured Si self-diffusivities [13,14] lead to too long annealing times or too high temperatures. Obviously, the diffusive Si mass transport by a mobile SiO_2 defect with local Si excess (that could either be named Si interstitial, SiO molecule [13], or oxygen vacancy [15]) does not necessarily follow the same mechanism as the $^{28}SiO_2$ / $^{30}SiO_2$ interface broadening, which was analyzed in self-diffusivity studies. In this study, the discrepancy between diffusive Si mass transport and Si self-diffusivity will not be discussed as our theoretical predictions aim at the reaction pathway of SiO_x decomposition rather than at a quantitative prediction of annealing time and temperature. Thus, KMC simulations utilize a relative time scale ”Monte Carlo steps” (MCS) that allows a posterior recalibration with realistic Si diffusivities [12].

Image processing of KMC simulation data allowed one to obtain KMC simulation snapshots that can be compared directly to PEELS-STEM or Fresnel images. In plane view, the simulation cell has been tripled laterally taking advantage of the periodic boundary conditions. The number of excess Si atoms in the vertical column below the pixel at (x,y) determines its gray level. The highest occurring number of Si atoms in such a column is assigned to white, whereas black means that no Si excess is found in the SiO_2 matrix.

No Si precipitates were observed in the sample for the lowest Si^+ fluence of $5 \times 10^{15}\,cm^{-2}$ (TEM images not shown here). For the medium Si^+ fluence of $1 \times 10^{16}\,cm^{-2}$, white spots in a dark background appear in the plane view Si plasmon map shown in Fig. 1(a) indicating spherical Si NCs embedded in the SiO_2 matrix. During thermal annealing, these NCs have formed by nucleation and growth in the Si enriched region of the implanted SiO_2 layer. The observed NCs are relatively small with an estimated mean diameter of 2.7 nm and have a high area density of $3.3 \times 10^{12}\,cm^{-2}$. A similar precipitate morphology with the same mean NC size and density is found in the KMC simulation snapshot of Fig. 1(b), but for a significantly lower Si^+ fluence of $3 \times 10^{15} cm^{-2}$ and a KMC simulation (annealing) time of 2100 kMCS. It should be noted that even this “medium” experimental Si^+ fluence of $1 \times 10^{16} cm^{-2}$ leads in the KMC simulation to the formation of coalesced poly-Si layer buried in the SiO_2 [4]. For the highest Si^+ fluence of $2 \times 10^{16}\,Si^+\,cm^{-2}$, the morphology of the phase separated Si has changed completely as observed in Fig. 1(c). A spaghetti-like network of white and black regions is found. This pattern clearly indicates that phase separation took place by spinodal decomposition. Even more, percolation is observed. Si precipitates are no longer spatially isolated, but an interconnected network of phase separated Si has formed. An equivalent morphology with the same typical distances as in Fig. 1(c) between the spinodal fingers is found in the KMC simulation snapshot of Fig. 1(d). This result was obtained for $8 \times 10^{15}\,Si^+\,cm^{-2}$ and a simulation time of 300 kMCS. Strikingly, the morphology agrees remarkably well between both images, while simulation snapshots for other fluences or annealing times deviate instead considerably from the morphology seen in Fig. 1(c).

Samples were studied additionally in cross section using a CM30 Phillips TEM equipped with a LaB_6 cathode operating at 300 kV. Fresnel imaging conditions were applied in order to achieve at least a weak contrast between Si and SiO_2 in cross sectional TEM (XTEM) images [5], i.e., images

were taken at out-of-Bragg alignment and under strongly underfocused bright field conditions.

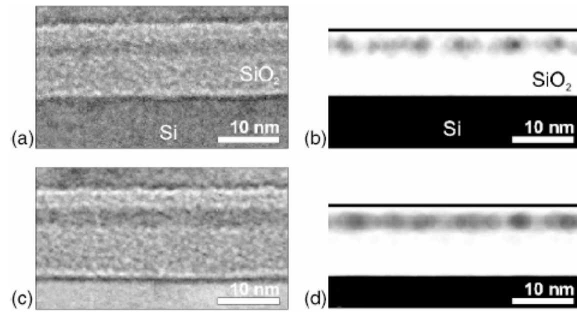

Fig. 2: Cross-section view of the layer of phase separated Si in SiO_2. Fresnel XTEM images for (a) $1 \times 10^{16}\,Si^+\,cm^{-2}$ and (c) $2 \times 10^{16}\,Si^+\,cm^{-2}$ are compared to cross-sectional KMC simulation snapshots for (b) $3 \times 10^{15}\,Si^+\,cm^{-2}$ and (d) $8 \times 10^{15}\,Si^+\,cm^{-2}$.

Details of the responsible contrast mechanism are given in Ref. 5. Figures 2(a) and 2(c) show the XTEM Fresnel images for fluences of $1 \times 10^{16}\,Si^+\,cm^{-2}$ and $2 \times 10^{16}\,Si^+\,cm^{-2}$, respectively. Cross section KMC simulation snapshots are displayed in Figs. 2(b) and 2(d) for $3 \times 10^{15}\,Si^+cm^{-2}$ (2100 kMCS) and $8 \times 10^{15}\,Si^+\,cm^{-2}$ (300 kMCS), respectively. Thereby, plane view image processing was applied to KMC cross section views with an inverted gray scale. In all images, the phase separated Si forms a single, sharp layer seen as gray band in the SiO_2 that is well separated from the SiO_2 / Si interface. Due to the extremely shallow Si excess profile obtained by low-energy Si^+ implantation, phase separation is quasiconfined to two dimensions. For $1 \times 10^{16}\,Si^+\,cm^{-2}$, Si precipitates align nicely in a thin layer, which is just a few nanometers thick, Fig. 2(a). When the Si^+ fluences are increased to $2 \times 10^{16}\,Si^+\,cm^{-2}$, the precipitate layer remains comparatively well localized in depth, Fig. 2(c), although the Si morphology observed in plane view has changed completely, Fig. 1(c). The total SiO_2 thickness is systematically smaller for the KMC simulations than for the corresponding Fresnel XTEM images. Nevertheless, the distance between the Si / SiO_2 interface and the phase separated Si agrees nicely for experiment and simulation.

Bright and dark regions correspond to Si and SiO_2 phases, respectively. The Si fluences in our KMC simulations were chosen in order to obtain morphologies of phase separated Si which are similar to experimental ones. This adjustments of our simulation reveals a strong discrepancy between experimental and theoretical Si fluences. More Si than theoretically predicted has to be implanted. Not all Si that has nominally been implanted into the SiO_2 is available for phase separation. The reason for the missing Si excess might be twofold. (i) Recent time of flight secondary ion mass spectroscopy measurements on low-energy, low-fluence $^{30}Si^+$ as-implanted SiO_2 samples indicate that only a fraction of about 0.5–0.7 of the nominal Si^+ fluence has been implanted into the SiO_2 [16]. (ii) It is known that (Si or Ge) NC formation in very thin SiO_2 films is extremely sensitive to humidity absorbed by the as-implanted (damaged) glass network [17] as well as to oxidants being present in the annealing ambient [18]. Thus, a considerable amount of the implanted Si might become oxidized during annealing. This explains also why no NCs have been observed by TEM for the lowest Si^+ fluence of $5 \times 10^{15}\,cm^{-2}$. The implanted Si has been oxidized completely during the thermal annealing. At the same time, oxidation of the implanted Si leads to a volume expansion that increases the overall SiO_2 layer thickness [6]. This swelling of the SiO_2 due to Si oxidation can be seen in the XTEM images of Figs. 2(a)–2(c) if compared to the KMC simulation snapshots, Figs. 2(b) and 2(d), which just include the SiO_2 expansion due to the incorporated Si atoms [9]. Here, the KMC simulations do not account for oxidation and the swelling caused by it. To do so, a multicomponent KMC approach (Si + O) is needed. Though samples have been annealed under fixed experimental conditions, the KMC simulation snapshots of corresponding Si patterns refer to different simulation times. Two reasons might be responsible for this discrepancy in the evolution speed. At first, the oxidation of a substantial part of implanted Si might influence the kinetics, and second, the Si bulk diffusion in SiO_2 might differ substantially from the Si diffusion at the Si / SiO_2 interface. Studies that investigate this point are under way.

Summarizing, extensive studies on low-energy ion beam synthesis of multi-dot Si floating-gates embedded in thin SiO_2 layers have been presented [19]. The morphology of this floating-gate layer is imaged by PEELS-STEM. A direct comparison to kinetic three-dimensional lattice Monte Carlo simulation snapshots have been made and show a remarkable agreement between the atomistic simulations and the PEELS-STEM images. A strong fluence dependence of the precipitate morphology is confirmed. For low Si^+ fluences, isolated Si NCs form by nucleation and growth, while high fluences lead to spinodal pattern. Predicted and measured morphologies agree remarkably well. However, the predicted fluences are lower than the experimental ones. A substantial fraction of the implanted Si is lost by parasitic oxidation with atmospheric humidity.

Acknowledgements

This work was supported by the European Commission through the Growth project G5RD/2000/00320 - NEON.

The presented results have been recently published as T. Müller et al., Appl. Phys. Lett. **85** (2004) 2373.

References

[1] S. Tiwari, F. Rana, H. Hanafi, A. Hartstein, E.F. Crabbe, K. Chan, Appl. Phys. Lett. **68** (1996) 1377

[2] S. Tiwari, J.A. Wahl, H. Silva, F. Rana, J.J. Welser, Appl. Phys. A: Mater. Sci. Process. **71** (2000) 403

[3] E. Kapetanakis, P. Normand, D. Tsoukalas, K. Beltsios, Appl. Phys. Lett. **80** (2002) 2794

[4] T. Müller, K.-H. Heinig, W. Möller, Appl. Phys. Lett. **81** (2002) 3049

[5] G.B. Assayag, C. Bonafos, M. Carrada, P. Normand, D. Tsoukalas, A. Claverie, Appl. Phys. Lett. **82** (2003) 200

[6] M. Carrada, N. Cherkashin, C. Bonafos, G. Benassayag, D. Chassaing, P. Normand, D. Tsoukalas, V. Soncini, A. Claverie, Mater. Sci. Eng. B **101** (2003) 204

[7] C. Bonafos, M. Carrada, N. Cherkashin, H. Coffin, D. Chassaing, G. Ben Assayag, A. Claverie, T. Müller, K. H. Heinig, M. Perego, M. Fanciulli, P. Normand, D. Tsoukalas, J. Appl. Phys. **95** (2004) 5696

[8] C. Jeanguillaume, C. Colliex, Ultramicroscopy **28** (1989) 252

[9] T. Müller, K.-H. Heinig, W. Möller, Mater. Sci. Eng. B **101** (2003) 49

[10] W. Möller, W. Eckstein, Nucl. Instr. Meth. B **2** (1984) 814

[11] K.-H. Heinig, T. Müller, B. Schmidt, M. Strobel, W. Möller, Appl. Phys. A: Mater. Sci. Process. **77** (2003) 17

[12] M. Strobel, K.-H. Heinig, W. Möller, Phys. Rev. B **64** (2001) 245422

[13] M. Uematsu, H. Kageshima, Y. Takahashi, S. Fukatsu, K.M. Itoh, K. Shiraishi, U. Gösele, Appl. Phys. Lett. **84** (2004) 876

[14] D. Mathiot, J.P. Schunck, M. Perego, M. Fanciulli, P. Normand, C. Tsamis, D. Tsoukalas, J. Appl. Phys. **94** (2003) 2136

[15] J. Song, L.R. Corrales, G. Kresse, H. Jonsson, Phys. Rev. B **64** (2001) 134102

[16] M. Perego, M. Fanculli, G. Ben Assayag, A. Claverie, private communication

[17] B. Schmidt, D. Grambole, F. Herrmann, Nucl. Instr. Meth. B **191** (2002) 482

[18] S. Oswald, B. Schmidt, K.-H. Heinig, Surf. Interface Anal. **29** (2000) 249

[19] T. Müller, K.-H. Heinig, W. Möller, C. Bonafos, H. Coffin, N. Cherkashin, G. Ben Assayag, S. Schamm, G. Zanchi, A. Claverie, M. Tencé, C. Colliex, Appl. Phys. Lett. **85** (2004) 2373

Application of Ultra-High Energy Boron Implantation for Superjunction Power (CoolMOS^{TM}) Devices

J. von Borany, M. Friedrich, M. Rüb[1], G. Deboy[2], J. Butschke[3] and F. Letzkus[3]

[1] *Infineon Technologies Austria AG, Villach, Austria*
[2] *Infineon Technologies AG, München*
[3] *Institut für Mikroelektronik, Stuttgart*

High-voltage superjunction devices (SJDs), firstly realized by Infineon's CoolMOS^{TM} technology, are a novel class of power devices which break the physical limit of silicon with respect to the area-specific turn-on-resistance value ($R_{on} \times A$) [1]. Such SJDs consist of a modified vertical MOSFET structure characterized by additional deep pillar-like p-type regions formed inside the n$^{(-)}$ epi-layer below the transistor gate, see Fig. 1. Charge compensation between p- and n-type regions leads to an electron accumulation in the drift layer between the p-type columns which results in a reduction of $R_{on} \times A$ up to a factor of 10 without any loss in the blocking capability. SDJs were introduced into the market between 1998 and 2000 [2–4]. On a commercial scale the vertical stack is presently fabricated with a high effort by repeated cycles of n-type epi-layer growth, masked boron implantation at common energies and subsequent diffusion. There are numerous suggestions for alternative technologies, most of them involving a deep trench structure [5,6]. The novel approach described in this contribution uses ultra-high energy boron implantation to form the p-type pillars. This concept represents a major simplification of SJDs fabrication since the overall number of process steps is drastically reduced.

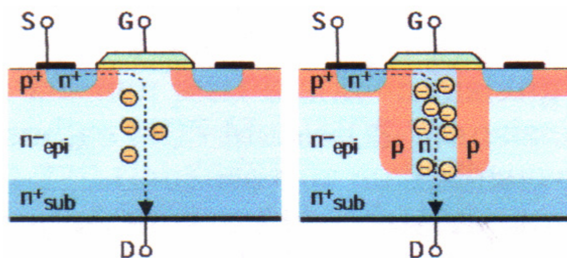

Fig. 1: Schematic cross-section view of a classical MOSFET (left) and a CoolMOS^{TM} power device (right).

The fabrication of CoolMOS^{TM} devices including high-energy boron implantation has been investigated based on the conventional Infineon's MOSFET power device technology. ∅ 6" Si (001) wafers with a n$^{(-)}$-type epi-layer ($\rho \sim 2\,\Omega$ cm) of approx. 40 µm thickness have been used. For the patterned implantation of high-energetic boron ions, reusable Si stencil hardmasks were developed by IMS Stuttgart [7]. The hardmasks were fabricated from SOI wafers (500 nm buried oxide, 22 µm SOI). In order to ensure safe masking even for 25 MeV boron ions (R_p = 34 µm) an additional thick epitaxial Si layer was grown to realize a total thickness of the SOI film of 45 µm.

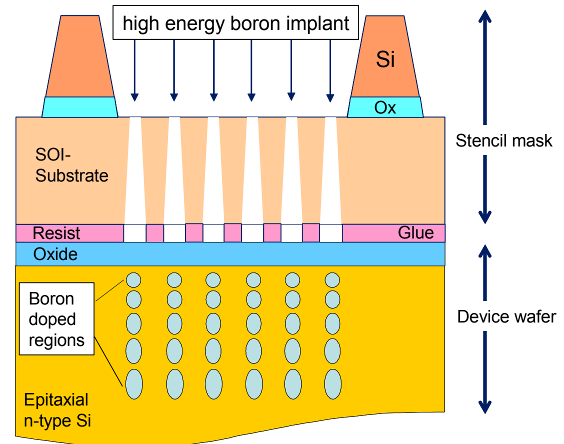

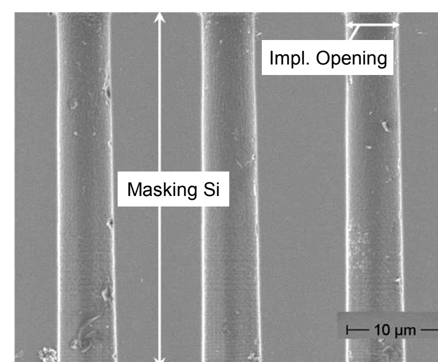

Fig. 2: Sketch of the mask/wafer stack as used for ultra-high energy boron implantation; the lower part of the figure shows a cross-sectional SEM image of the etched Si stencil mask.

Using a trench etch process with sidewall passivation (gas chopping technique), deep trenches of typical 6.4 µm diameter and 45 µm depth (aspect ratio: 7:1) with a taper angle of 89.8° were etched into the SOI film. Subsequently the wafer

rear side was patterned and etched with alkaline based anisotropic etch chemistry (KOH/TMAH) where the buried oxide acts as an etch stop layer. Mechanical stability was achieved by an optimized backside patterning forming a grid of thick stabilizing elements. The stencil mask and the wafer were connected by a photoresist based gluing technique. The schematic arrangement of the stack and an SEM image of the stencil mask is shown in Fig. 2.

The ultra-high energy boron implantation was carried out at the 5 MV tandem accelerator of the Ion Beam Center at FZR. A five-fold implantation sequence with boron energies between 2.5 and 25 MeV and fluences from $5 \times 10^{12} - 1 \times 10^{13}\,cm^{-2}$ per implantation step was applied. The wafer temperature was kept below 100°C by using an appropriate beam current to avoid any replacement of the stencil mask during implantation. Due to the large aspect ratio of the stencil mask openings the implantation has to be performed under normal incidence conditions with a total deviation of the ions incidence angle distribution (including misalignment of the beam and/or the wafer) across the fully implanted 6" wafer of less than ± 1°. With a two-dimensional electrostatic scanning (f ~ 1 kHz) this demand could be fulfilled due to the large distance of approx. 8 m between the scanning plates and the implantation chamber, and a precise alignment of the beam axis and the wafer position.

To enable an exact alignment of the subsequent photolithography steps for gate or source patterning relative to the boron doped regions with an accuracy of <1 µm, an additional masked Si implantation (1.2 MeV, $5 \times 10^{14}\,cm^{-2}$) was carried out into the SiO_2 layer. After the removal of the stencil mask, an isotropic etching in buffered HF decorates the implanted area due to an increased etching rate of the implanted oxide [8].

A crucial point of ultra-high energy implantation is the radiation generation, as the Coulomb barrier energy for B in Si is about 12 MeV. Hence, for energies above this value particle (n, p, α) and γ-ray emission during implantation occurs and radioactive activation of the stencil mask and the wafer has to be kept in mind. Table 1 summarizes the main nuclear reaction channels. The permanent radiation level during the implantation is high. Typical dose rates during a boron implantation at 25 MeV (measured in a distance of 30 cm outside the chamber) amount to 2.2 mSv/h and 1.0 mSv/h (per 0.1 pµA) for neutrons and γ-rays, respectively, which vary linearly with the ion current. Therefore, the ultra-high energy boron implantation requires a suitable shielding of the wafer chamber and/or a separate radiation controlled area for wafer processing.

Table 1: Main nuclear reaction channels for 25 MeV boron ions with different isotopes of silicon. β-, β+, EC (electron capture), IT (isomeric transition) denote the different decay modes, respectively.

	Chan.	Nucleus	σ (barn)	T 1/2	Decay	Final Isotop
28Si	pα	34 S	104,3	stable		34 S
	2p	37 Cl	48,7			37 Cl
	np	37 Ar	217,7	35.0 d	EC	37 Cl
	nα	34 Cl 34m Cl	33,7	1.53 s 32.0 min	β+ β+ (53%) IT (47%)	34 S 34 S 34 S
29Si	np	38 Ar	174,3	stable		38 Ar
	npα	34 S	125,2			34 S
	nα	35 Cl	112			35 Cl
	2np	37 Ar	43,3	35.0 d	EC	37 Cl
	2np	38 K 38m K	29,4	7,61 min 0,93 s	β+ β+	38 Ar 38 Ar
30Si	2np	38 Ar	129,7	stable		38 Ar
	2np	39 K	72,8			39 K
	nα	36 Cl	187,4	$3.0 x 10^5$ y	β- (98%) EC (2%)	36 Ar 36 S
	np	39 Ar	132,7	269 y	β-	39 K

During implantation various stable isotopes of Al, P, S, Cl, and Ar are produced in the near-surface region (≤20 µm depth). For a cross section of σ=100 mbarn and a fluence of $1 \times 10^{13}\,cm^{-2}$ their concentration is $<5 \times 10^{13}\,cm^{-3}$ which should not deteriorate the device properties.

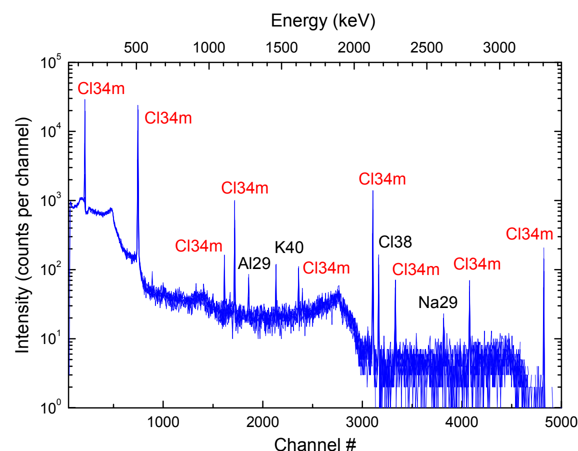

Fig. 3: γ-spectrum of a virgin 4" Si wafer fully implanted with boron 25 MeV, $2 \times 10^{12}\,cm^{-2}$, measured with a Ge detector. The total activity of the wafer immediately after implantation corresponds to 1.1 kBq/cm².

After implantation, the radiation level drops significantly, but due to the generation of radioactive isotopes (see Table 1) a certain radiation level is still present for some time. The γ-spectrum of Fig. 3 reveals that the most relevant contribution of the radiation from an activated wafer results from

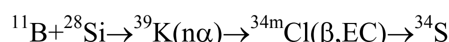

$$^{11}B + ^{28}Si \rightarrow ^{39}K(n\alpha) \rightarrow ^{34m}Cl(\beta,EC) \rightarrow ^{34}S$$

with a tabulated half-life time of 32 min. Time dependent radiation measurements reveal that a dose rate of <10 µSv/h (necessary to continue wafer processing) is achieved for a boron implant-

ation of 25 MeV, 5×10^{12} cm^{-2} (∅ 4” Si wafer, fully implanted) within approx. two hours. If the implantation sequence of the lot starts with the highest energy usually the mask/wafer stack can be handled immediately after implantation without further decay time. Thus, the main restriction for the use of ultra-high energy ion implantation results from the intense radiation level during implantation. However, a careful selection of main beamline and endstation materials is necessary to avoid long-term activation.

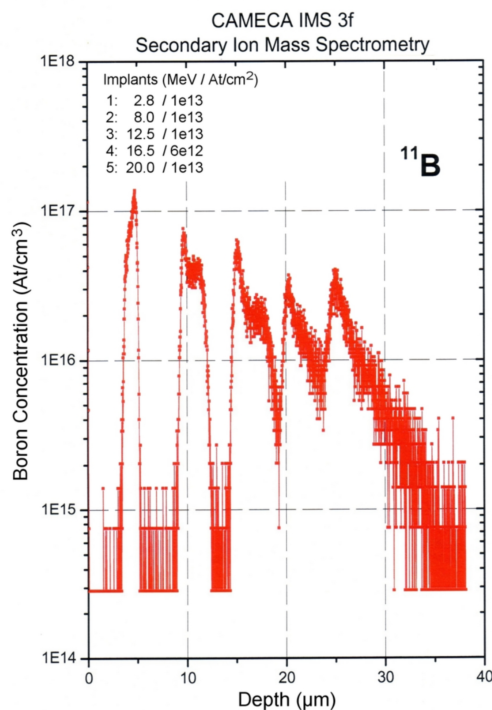

Fig. 4: SIMS depth profile of a five-fold boron implant using energies between 2.8 and 20 MeV.

Figure 4 shows an as-implanted boron profile measured by SIMS. The well separated boron doped regions of the five-fold implantation sequence can be easily distinguished. Each peak shows a characteristic distribution with contributions from channeled and dechanneled ions. The strong influence of (axial) channeling is evident as the implantations were performed under normal incidence conditions. Whereas for the lowest energy the peak distribution is mainly determined by channeled ions the influence of the channeling decreases with increasing energy. This effect can be explained by the energy dependence of the critical angle. Hobler [9] calculated the critical angles for boron channeling along the Si [100] axis to 0.8° or 0.2° for 1 or 25 MeV, respectively, which corresponds qualitatively to the measured SIMS profile. Due to the unknown angle distribution of the incident ions and the influence of the stencil mask a further detailed discussion is not possible.

CoolMOS™ device structures require the formation of continuously p-type doped pillars. Therefore, after implantation the wafers were heat-treated at 1150°C for several hours to connect the local doped boron regions by diffusion. For an annealing of 6 h at 1150°C the boron diffusion length is ~ 2.1 µm which enables the formation of continuous boron columns. For such annealing parameters the radial broadening of the boron pillars is not anymore determined by the ion straggling (ΔR_{rad}<1 µm). In addition, the heat treatment ensures the electrical activation of the dopands and the annealing of the radiation damage. Figure 5 shows the depth distribution of the carrier concentration after annealing measured with spreading resistance profiling. It confirms the formation of a continuous p-type region with $n \sim 10^{16}$ cm^{-3} in a depth between 2 and 40 µm and a sufficient spatial variation in the carrier concentration.

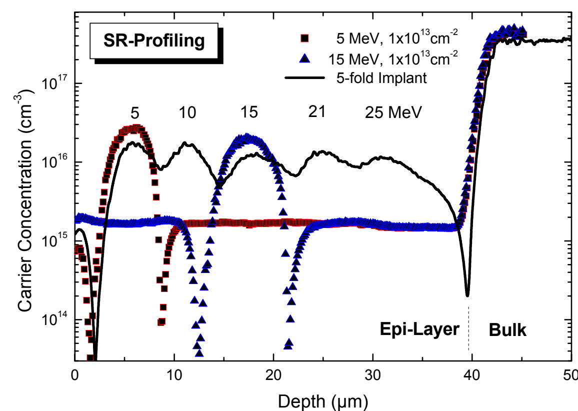

Fig. 5: Spreading resistance profile of two single boron implants of 5 and 15 MeV and a five-fold boron implantation with energies between 5 and 25 MeV. Different fluences have been applied for the single- and the multi-implants. The n-type epi-layer has a thickness of 40 µm and a concentration of 2×10^{15} cm^{-3}.

MOSFETs with an active chip area of 21.05 mm² have been fabricated which corresponds to a nominal 20 A product. The electrical device characterization clearly demonstrates that the high-energy implantation process yields fully functional high-voltage transistors. For the best run the wafers yield a median value of the blocking voltage of 556 V and a ($R_{on} \times A$) value of typically 3.85 Ω mm². The reverse leakage currents measured on fully processed wafers are very low (<1×10^{-8} A/cm^2 @ 25°C; <1×10^{-5} A/cm^2 @ 150°C), smaller than the values given in Infineon´s data sheets for comparable CoolMOS products [10]. These low reverse current values reveal that the damage due to high-energy boron bombardment is well annealed and the small amount of “contaminants” fabricated by ion-beam induced activation does not deteriorate the device proper-

ties. A more detailed description of the device properties are given in Ref. 8.

In summary, ultra-high energy boron implantation shows a technological way towards lower ($R_{on} \times A$) values in agreement with further MOSFET size shrinkage rules. In order to establish ultra-high energy implantation as a volume production technology still various questions have to be addressed. Among the open questions stencil mask and radiation features belong to the most important issues. The use of a separate projection stencil mask seems necessary to reduce the number of required masks, to enable higher beam currents and to avoid the process steps for stack fabrication and separation. An increase of the number of implantation steps (with tailored fluences) is easily possible to optimize the doping profile along the column depth. In such a way the thermal budget can be lowered which corresponds to a reduction in the radial diffusion broadening. As no long-term activation is present the radiation issue is no hindrance for production technology. Moreover, if the boron energy is limited to values < 12 MeV (i.e. epitaxy and high-energy implantation is performed in two subsequent cycles), the radiation emission can be significantly reduced or even avoided. Nevertheless it is worthwhile to address all the problems since this technology is one of the few candidates capable of strongly reducing wafer costs for SJDs.

Acknowledgements

The authors would like to thank M. Kaden from the VKTA Rossendorf for performing the γ-spectrometry measurements and H. Strack and G. Miller of Infineon Technologies for valuable discussions and support. This work was supported by the Bundesministerium für Forschung und Technologie of the Federal Republic of Germany under contract No. 01M3121 which is gratefully acknowledged.

References

[1] G. Deboy, L. Lorenz, M. März, Elektronik (1998) 42

[2] G. Deboy, M. März, J.-P. Stengl, H. Strack, J. Tihanyi, W.Weber, Tech. Digest IEDM 98, San Francisco, USA, 1998, p. 683

[3] L. Lorenz, G. Deboy, A. Knapp, M. März, Proc. ISPSD 1999, Toronto, Canada, 1999, p. 3

[4] M. Saggio, D. Fagone, S. Musumeci, Proc. ISPSD 2000, Toulouse, France, 2000, p. 65

[5] T. Minato, T. Nitta, A. Uenisi, M. Yano, M. Harada, S. Hine, Proc. ISPSD 2000, Toulouse, France, 2000, p. 73

[6] M. Rüb, D. Ahlers, J. Baumgartl, G. Deboy, W. Friza, O. Häberlein, I. Steinigke, Proc. ISPSD 2003, Cambridge, UK, 2003, p. 203

[7] J. Butschke; A. Ehrmann, B. Höfflinger, M. Irmscher, R. Käsmaier, F. Letzkus, H. Löschner, J. Mathani, C. Reuter, C. Schomburg, R. Springer, Microelectr. Engin. **46** (1999) 473

[8] M. Rüb, M. Bär, G. Deboy, F.-J. Niedernostheide, M. Schmitt, H.-J. Schulze, A. Willmeroth, Proc. ISPSD 2004, Kitakyushu, Japan, 2004, p. 455

[9] G. Hobler, Rad. Effects and Defects in Solids **139** (1996) 21

[10] http://www.infineon.com/coolmos

Real-Time Evolution of the Indium Tin Oxide Film Properties and Structure During Annealing in Vacuum

A. Rogozin, N. Shevchenko, M. Vinnichenko[1], F. Prokert, V. Cantelli, A. Kolitsch and W. Möller

[1]*Physics Department, Kyiv National Taras Shevchenko University, Kyiv 01033, Ukraine*

Indium tin oxide (ITO) is widely applied as a transparent conductive oxide coating. A standard and successful industrial route of production is its deposition by magnetron sputtering from a compound (oxide) target [1]. To increase cost efficiency, it would be preferable to sputter reactively from a metal target at sufficiently high partial pressure of oxygen. However, under this condition, a satisfactorily low resistivity of the films cannot readily be obtained, [2] so that a deposition on heated substrates or post-deposition annealing is necessary. So far, the annealing processes for reactively sputtered ITO [3,4] have only been studied for metal-rich films, in contrast to comprehensive studies after magnetron sputtering from ceramic targets [5-10]. Moreover, mainly isothermal heat treatment is considered in the literature, although annealing using a temperature ramp is of more relevance for practical application. Several investigations report on real-time *in situ* monitoring of the ITO film resistivity and reflectivity [9,10], which is used for an indirect characterization of the crystalline structure of the films. This approach requires simplifying assumptions on the linear dependence of the resistivity or reflectivity on the crystalline fraction, and the stability of the film roughness during annealing. Direct investigations of the influence of heat treatment on the ITO film structure are so far limited to post-annealing studies by X-ray diffraction (XRD) and scanning or transmission electron microscopy [3-5,7,8,11].

Annealing of ITO is known to be very efficient in increasing the carrier concentration. It can be quite reasonably explained by the Frank–Köstlin model [12] which accounts for tin donor activation at elevated temperatures. However, this model is valid only for crystalline ITO. The amorphous-to-crystalline transition in ITO during annealing is often assumed as the reason for this activation, but the physics behind the experimental observation is not clear. In the present letter we report the results of a real-time *in situ* investigation of the film properties and the structure evolution during annealing in vacuum.

The films are produced by reactive pulsed middle frequency magnetron sputtering using the facility and procedure described in Ref. 13. The chamber was pumped to a base pressure of 4×10^{-4} Pa before deposition. The deposition runs were carried out for 2.5 min at an Ar flow of 30 sccm (partial pressure 1.2 Pa) and O_2 flow of 64 sccm (0.3 Pa). The films are grown on Si (100) substrates ($24 \times 12 \times 0.3$ mm^3) covered with SiO_2 (510 nm), which were not heated externally during deposition. The average thickness of the deposited films is 130 nm. The as-deposited films show no crystalline peaks in the XRD patterns and are considered as amorphous.

The post-deposition annealing of identical ITO samples was carried out at two different experimental setups, the **RO**ssendorf **B**eam **L**ine (ROBL) at the European Synchrotron Radiation Facility in Grenoble, [14] and the ITO deposition facility at Forschungszentrum Rossendorf [13]. In both cases the total pressure of the residual gas was below 6×10^{-4} Pa. During annealing the sample was placed on a boralectric heater (Tectra, Germany). The sample temperature was controlled by a standard K-type thermocouple. In contrast to previous investigations [3-10] on isothermal annealing, in present work the annealing temperature T_a was gradually increased from 20 to 330°C at a constant rate of approximately 5 K/min. In both experimental setups, the resistivity of the ITO films was monitored *in situ* by the four point probe technique.

In order to study the evolution of the ITO film structure in real time, a UHV annealing chamber, equipped with an X-ray transparent beryllium dome, was mounted on a six-circle goniometer. The X-ray diffraction experiment was performed in Bragg–Brentano geometry within the range of scattering angles of 27-37°. The incident X-ray beam was monochromatized to 8.048 keV ($\lambda = 0.154$ nm). A multi-channel position sensitive detector allowed a fast scan acquisition time of 100 s. The XRD data were evaluated by the PeakFit software (Jandel Scientific).

A spectroscopic rotating compensator ellipsometer (M-2000, J.A Wollam Inc, USA) was used at FZR for *in situ* monitoring of the evaluation of the film optical properties. The ellipsometer is installed at the deposition chamber which is equipped with fused silica windows at angle of light incidence of 70.7° with respect to the surface normal. The spectra of conventional spectroscopic ellipsometry (SE) parameters (Ψ, Δ) [15] within the probing photon energy range of 1.2–3.3 eV were regularly recorded at 6 s intervals. The data were acquired and evaluated by the WVASE® software. A multilayer model [ambience/roughness layer/bulk ITO layer /SiO_2/Si] was fitted to the measured (Ψ, Δ) spectra in ten different time intervals. The effect of elevated temperature on the optical properties of Si is accounted for by calibration at ten different temperatures. The dielectric function of the surface roughness layer was modeled as a 50/50 vol.% mixture of the ITO layer and voids, applying the Bruggeman effective medium approximation (EMA). The dielectric function of bulk ITO was parameterized in the Drude-Lorentz approach [15], which allows estimation of the free electron density N_{Dr} at a given temperature [16].

After increasing the annealing temperature T_a up to 250 ± 10°C, the XRD patterns show only a broad amorphous peak around 32°, indicating the absence of any structural changes below this temperature. The evolution of the XRD patterns with annealing temperature within the range 200-320°C is shown in Fig. 1. At $T_a = 250$°C, the (222) and (400) peaks of crystalline In_2O_3 phase start to appear. Their intensity increases strongly as T_a increases by approximately 30°C, pointing to a rapid crystallization of the ITO film. The film becomes completely crystalline at $T_a \geq 280$°C with a stable structure above. The calculation of the texture coefficient by known equations [17] shows that the film exhibits a weak (222) fibre texture in this state. The size of coherently diffracting domains was estimated by the Scherrer formula to 65 ± 4 nm.

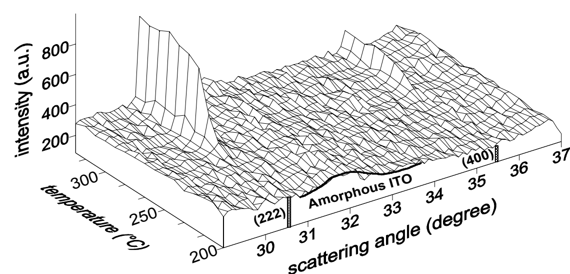

Fig. 1: Evolution of XRD patterns during annealing in vacuum.

The observed temperature of crystallization of 250°C is significantly larger than published values ranging from 150 to 200°C, which are often cited [9,10]. However, the latter are deduced from post-deposition XRD studies of ITO layers produced on heated substrates [18]. During deposition, additional activation may occur due to plasma-surface interaction including fast ion bombardment, which might promote the crystallization at lower temperatures.

The temperature dependence of XRD integral intensity of the In_2O_3 (222) peak ($I_{(222)}$) (Fig. 2(a)) has the typical S-like shape, being characteristic for the enhancement of the crystalline fraction during the amorphous-to-crystalline transition. The observed EMA roughness enhancement can be mainly related to the film crystallization because it occurs within the identical temperature range of 250-280°C.

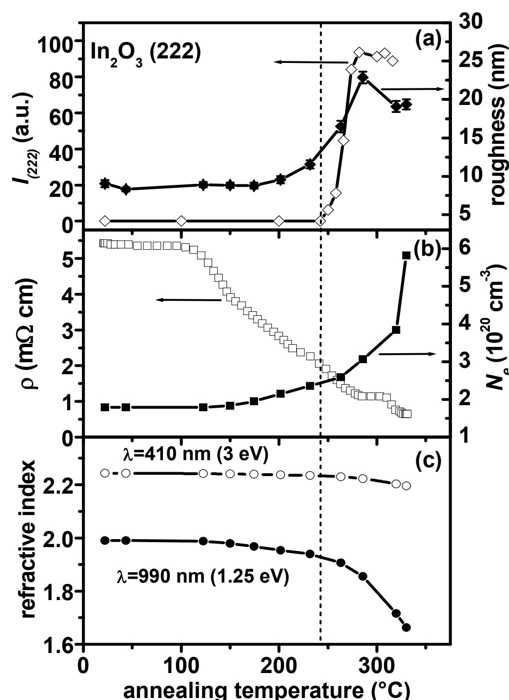

Fig. 2: The temperature dependence during annealing of the XRD integral intensity of the In_2O_3 (222) peak ($I_{(222)}$) along with the EMA roughness (a), resistivity and free electron density N_{Dr} (b), and refractive index at two wavelengths (c).

Defining the degree of crystallization by $f = I_{(222)}/I_{C(222)}$, where $I_{C(222)}$ is the integral intensity measured at complete crystallization, its time dependence is analyzed by using the Kolmogorov–Johnson–Mehl–Avrami equation [19-21]

$$f = 1 - \exp(-K\ t^n),$$

where n is a kinetic exponent and K is a rate constant. A linear fit of the function $-\ln(1\text{-}f)$

plotted versus the acquisition time on a double-logarithmic scale, yields $n = 2.99 \pm 0.23$. Under the condition that the coherently diffracting domain size is smaller than the film thickness, this kinetic exponent indicates a three-dimensional crystallization process.

The observed temperature dependences of the resistivity in Fig. 2(b) and ellipsometry (Ψ, Δ) parameters (not shown here) indicate several stages with features at $T_a = 110$, 150, 280 and 310°C, in contrast to the more simple two-stage behavior of the resistivity and single–stage behavior of the reflectivity observed during isothermal annealing [9,10]. The temperature behavior of N_{Dr} in the Fig. 2(b) qualitatively agrees with a decrease of the resistivity, except in the temperature range of 280-310°C.

The refractive index in Fig. 2(c) decreases at increasing annealing temperature above 150°C. An even stronger decrease is observed above $T_a = 250$°C that relates to the free electron density behavior. The absolute values of the refractive index agree with the results reported elsewhere [22,23]. The decrease of the refractive index is ascribed to the enhancement of N_{Dr} [22].

From the stability of the film resistivity and refractive index it can be concluded that neither the free electron density nor the structure of the ITO films change during the first 20 min of annealing, corresponding to a temperature below $T_a \sim 120$°C. According to literature [11], the resistivity also does not change during isothermal annealing in vacuum at $T_a = 125$°C for the same time. At higher temperatures (120-240°C) the free electron density rises in the amorphous ITO (Fig. 2(b)). According to Ref. 10, the increase of the free electron density can be attributed to the creation of oxygen vacancies due to relaxation of distorted In-O bonds in the amorphous phase. Since Sn is known not to be electrically active in amorphous ITO [6,24] and does not affect the free electron density, any creation of substitutional Sn in the amorphous film can be neglected.

As the resistivity decreases faster than N_{Dr} increases, the free electron mobility can be assumed to be enhanced. However, due to the fit parameter correlation, it was not possible to extract from the SE data reliable values of the mobility in the whole temperature range, although the results suggest a mobility enhancement within the range 120-240°C.

The fast enhancement of the free electron density, N_{Dr}, after the beginning of crystallization ($T_a \sim 250$°C) can be explained by the onset of Sn donor activation [9,10,24] in a growing crystalline phase. However, the SE is sensitive to the free electron density enhancement even in crystalline grains which are electrically insulated or have bad contact to each other [23]. These grains do not contribute to resistivity decrease until they are electrically connected. Possibly such connections are a reason for the drop of resistivity ($T_a > 310$°C) after a plateau observed at increasing N_{Dr} within the temperature range 280-310°C.

The comparison of the graphs in Fig. 2 clearly shows that at constant heating rate the resistivity and optical properties depend non-linearly on the crystalline fraction. This is in contrast to the linearity which is often assumed in the literature. A reason for this discrepancy might be the change of surface roughness in this particular case, which renders reliable monitoring of the film structure evolution by indirect techniques extremely difficult.

In summary, the structure and properties of ITO films deposited by reactive magnetron sputtering have been monitored in real time during annealing in vacuum, using three complementary *in situ* techniques. The direct observation of the structure yields a crystallization temperature of 250°C. Even in the amorphous state the film resistivity decreases significantly at increasing temperature, probably due to relaxation of distorted In-O bonds in the amorphous phase, which leads to a free electron density enhancement by the creation of oxygen vacancies. The rapid crystallization is accompanied by film roughening and leads to a further decrease of the resistivity due to Sn donor activation.

The present results have been previously published as A. Rogozin *et al.*; Appl. Phys. Lett. **85** (2004) 212.

References

[1] B.G. Lewis, D.C. Paine, MRS Bull. **25** (2000) 22

[2] R.B.H. Tahar, T. Ban, Y. Ohya, Y. Takahashi, J. Appl. Phys. **83** (1998) 2631

[3] A.J. Steckl, G. Mohammed, J. Appl. Phys. **51** (1980) 3890

[4] S. Chaudhuri, J. Bhattacharyya, A.K. Pal, Thin Solid Films **148** (1987) 279

[5] Y. Shigesato, S. Takaki, T. Haranoh, J. Appl. Phys. **71** (1992) 3356

[6] Y. Shigesato, D.C. Paine, Appl. Phys. Lett. **62** (1993) 1268

[7] M. Higuchi, S. Uekusa, R. Nakano, K. Yokogawa, Jpn. J. Appl. Phys. **33** (1994) 302

[8] S. Takayama, T. Sugawara, A. Tanaka, T. Himuro, J. Vac. Sci. Technol. A **21** (2003) 1352

[9] C.W. Ow-Yang, D. Spinner, Y. Shigesato, D.C. Paine, J. Appl. Phys. **83** (1998) 145

[10] D.C. Paine, T. Whitson, D. Janiac, R. Beresford, C. Ow Yang, B. Lewis, J. Appl. Phys. **85** (1999) 8445

[11] H. Morikawa, M. Fujita, Thin Solid Films **339** (1999) 309

[12] G. Frank, H. Köstlin, Appl. Phys. A: Solids Surf. **27** (1992) 197

[13] A.I. Rogozin, M.V. Vinnichenko, A. Kolitsch, W. Möller, J. Vac. Sci. Technol. A **22** (2004) 349

[14] W. Matz, N. Schell, G. Bernhard, J. Claussner, W. Oehme, F. Prokert, T. Reich, R. Schlenk, D. Pröhl, H. Funke, F. Eichhorn, M. Betzl, S. Dienel, V. Brendler, A. Denecke H. Krug, W. Neumann, G. Hüttig, P. Reichel, U. Strauch, J. Synchrotron Rad. **6** (1999) 1076

[15] B. Johs, J.A. Woollam, C.M. Herzinger, J. Hilfilker, R. Synowicki, C.L. Bungay, Crit. Rev. Opt. Sci. Technol. **CR72** (1999) 29

[16] I. Hamberg, C.G. Granqvist, J. Appl. Phys. **60** (1986) R123

[17] H.-E. Cheng, M.-H. Hon, J. Appl. Phys. **79** (1996) 8047

[18] S. Muranaka, Y. Bando, T. Takada, Thin Solid Films **151** (1987) 355

[19] A. Kolmogorov, Izv. Akad. Nauk SSSR, Ser. Matem. **1** (1937) 355

[20] W. Johnson, R. Mehl, Trans. AIME **135** (1939) 416

[21] M. Avrami, J. Chem. Phys. **7** (1939) 1103

[22] B.N. De, Y. Zhao, P.G. Snyder, J.A. Woollam, T.J. Coutts, X. Li, Thin Solid Films **39**, (1989) 647

[23] D. Mergel, Z. Qiao, J. Phys. **D 35** (2002) 794

[24] J.R. Bellingham, W.A. Phillips, C.J. Adkins, J. Phys. Condens. Matter **2** (1990) 6207

X-Ray Diffraction Study of Stress Relaxation in Cubic Boron Nitride Films Grown with Simultaneous Medium-Energy Ion Bombardment

B. Abendroth, R. Gago, F. Eichhorn and W. Möller

Cubic boron nitride (cBN) is, next to diamond, the second hardest material known. In contrast to diamond, cBN does not react with ferrous metals and is stable against oxidation up to 1300°C [1]. Thus, cBN is a very promising material for tribological applications. The growth of cBN films has been demonstrated using a variety of physical and chemical vapor deposition processes (for detailed review articles, see Refs. 1 and 2). In general, all deposition processes have in common that a low energy ion bombardment (~ 100–500 eV) is required for the nucleation and growth of the cBN [3]. As a consequence of this low energy ion bombardment, the films exhibit very high intrinsic compressive stress (exceeding -10 GPa), which limits the adhesion and the maximum film thickness [1].

In order to reduce the stress in cBN films, several relaxation methods have been reported [4]. Among them, a promising option is the use of ion implantation into regions well below the film surface (30 keV–1 MeV) [5,6]. Following this approach, the combination of sequential *in situ* ion implantation and film growth has been shown as a method to produce thick films (> 1 μm) [7]. This study has been successfully extended to simultaneous medium-energy ion implantation during the growth by ion beam assisted deposition [8,9] and magnetron sputtering (MS) [10]. In these investigations, it was found that the stress relaxation is controlled by the flux and energy of the medium-energy ions implanted during the growth. Particularly, the amount of stress release correlates with the number of atomic displacements generated by the medium-energy ion impacts. Post deposition annealing has also been demonstrated to reduce stress in cBN thin films [11,12], but is less efficient than ion implantation [6,12]. Annealing additional to medium energy ion implantation, however, was found to reduce efficiently the structural degradation, which accompanies the ion implantation process [6,13].

Despite the effective stress release upon medium-energy ion bombardment, the relaxation mechanisms are not well identified. One way to quantify the film stress evolution and to monitor the stress relaxation during the film growth is to measure *in situ* the substrate curvature during deposition by means of laser deflection [14]. However, the measurement of the substrate curvature yields the film stress on a macroscopic level (sum of intrinsic, interface, and thermal stresses), which makes it difficult to discern between the contribution of different relaxation mechanisms. The aim of this work was to study the stress relaxation induced by simultaneous medium-energy ion bombardment during the growth by MS on an atomic scale by means of x-ray diffraction (XRD) using high-brilliance synchrotron radiation and, in this way, identify possible mechanisms involved.

The cBN thin films were prepared by radio frequency MS in Ar/N_2 (35% and 100% N_2) discharge. A negative dc substrate bias (-150 V) in combination with negative high voltage (HV) pulses (2-8 kV) were used to enable cBN nucleation and growth and simultaneously achieve stress relaxation. Prior to the nucleation of cBN a ~ 50 nm hexagonal BN (hBN) buffer layer was deposited to improve the adhesion and the total film thickness was 150 nm. For comparison, one sample was produced without medium energy ion bombardment. To prevent delamination, the total thickness of this sample was limited to ~ 50 nm. The evolution of the stress during deposition was monitored with *in situ* substrate bending measurements by laser deflection. The details of sample preparation and *in situ* stress measurement are given in Ref. 10. The value of residual stress for the films considered in this work and the preparation parameters are shown in Table 1. The data show a clear correlation between the stress level and the amount of ion damage induced by the medium-energy ions. The dynamic ion damage that is produced during the HV pulses is expressed in terms of displacements per atom (dpa). The number of dpa was calculated for each sample from the total number of displacements per incoming ion as obtained by SRIM [15] (with the energy of N^+ being half that of Ar^+), the ion flux, which depends on the HV pulse frequency, and the growth rate (5 nm/s). Additionally, a sample prepared with medium-energy ion implantation

Table 1: Medium-energy ion bombardment parameters during MS deposition and the computed ion induced damage. The measured intrinsic stress values derived from *in situ* cantilever bending are also included and correlate with the degree of ion induced damage.

Pulse voltage (kV)	Pulse frequency (kHz)	Stationary damage (dpa)	Stress (GPa)	Comments
		0	-9.0 ± 0.1	cBN with high stress
-8	2.8	0.5	-2.6 ± 0.1	100% N2 discharge
-4	2.8	0.7	-1.7 ± 0.1	Ar + N2 discharge
-8	2.8	1.2	-1.6 ± 0.1	Ar + N2 discharge
-8	2.8	1.2	…	Ar + N_2 discharge annealing at 900°C

(1.2 dpa) was annealed at 900°C after deposition as a reference sample with no or very low stress.

XRD measurements were performed at the **RO**ssendorf **B**eam **L**ine (ROBL) [16] at the European Synchrotron Radiation Facility (ESRF). The experiments were done under grazing incidence to minimize the signal coming from the Si substrate. The wavelength of the incident x-ray was 1.2 Å (10.3 keV) and the angle of incidence (θ) was set to 0.2°, slightly above the critical angle for total internal reflection ($\alpha_c = 0.19°$) to enhance the intensity of the signal. For each sample in-plane (2ω) and out-of-plane (2θ) scans were performed. In this way, lattice planes oriented perpendicular and parallel, respectively, to the surface can be detected and a biaxial stress in the samples can be mapped.

Figure 1 shows the data recorded in-plane (a) and out-of-plane (b) detector scans for cBN samples produced with different medium-energy ion damage. The sample grown without HV pulses (lowest curve in Figs. 1(a) and 1(b)) is used as a reference representing a nonrelaxed cBN film and, hence, with high compressive stress. In the in-plane geometry, the Bragg peaks related to the hBN (002) and cBN (111) reflections are identified. The hBN signal originates mainly from the hBN buffer layer. In the out-of-plane geometry, the hBN (002) peak vanishes due to the preferential orientation of this buffer layer with the *c* axis parallel to the substrate, which is typical for hBN grown under low energy ion bombardment [17]. The cBN (111) diffraction peak in all samples is more intense in the out-of-plane than in the in-plane scan, indicating a preferential orientation of the cBN(111) planes parallel to the surface. This texture is more pronounced in the sample grown without HV pulses (nonrelaxed) and it is attenuated with the addition of medium-energy ion bombardment.

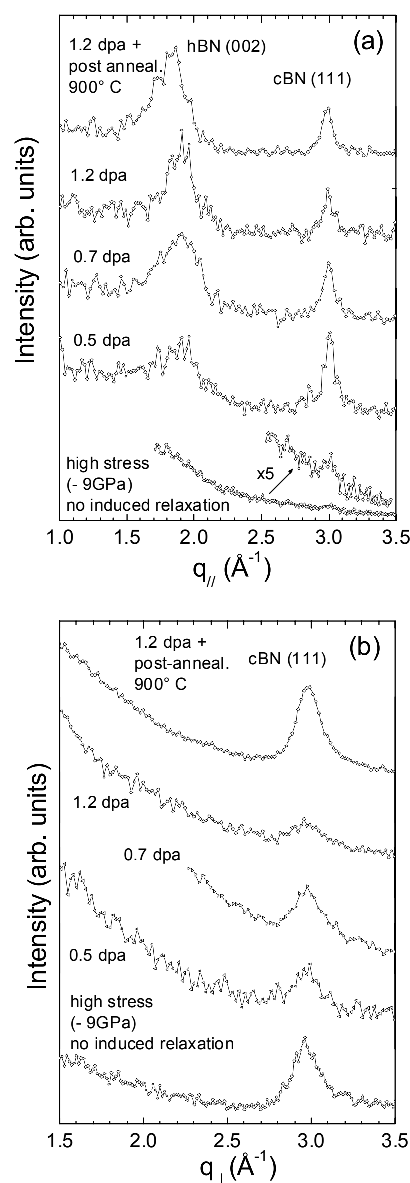

Fig. 1: In-plane (a) and out-of-plane (b) diffraction pattern of BN thin films with different ion induced damage and stress relaxation. The in-plane spectrum of the nonreleased sample shows a very low intensity due to the small film thickness (50 nm).

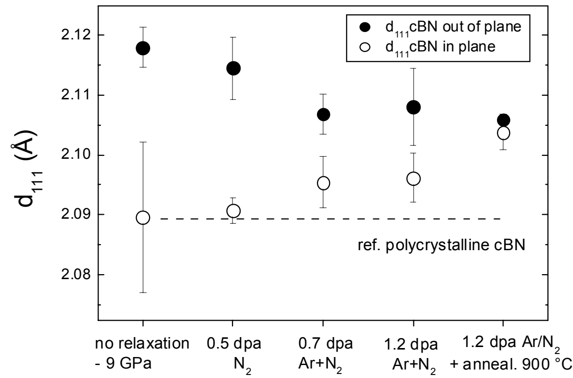

Fig. 2: cBN (111) lattice spacing measured in the in-plane (•) and out-of-plane (o) geometries for samples with different degree of ion-induced damage and stress relaxation. For comparison, the values of polycrystalline cBN, a nonrelaxed cBN thin film and a cBN thin film that is stress free after annealing at 900°C are shown.

Figure 2 shows the cBN (111) lattice distances, *d*(111), obtained from the fitting of the diffraction patterns of Fig. 1. Due to the high texture for the sample grown without HV pulses and its low thickness, the error in the fitted in-plane cBN(111) peak position is larger than for the other samples. For comparison, the tabulated *d*(111) value of polycrystalline cBN (Ref. 18) is also included. Even under compressive stress, the in-plane *d*(111) values from the cBN films are larger than for the cBN powder reference. This is most likely due to the nanocrystalline structure and incorporation of defects as a result of the deposition process. The *d*(111) interplanar distance is larger in the out-of-plane than in the in-plane direction, indicating a pronounced biaxial state of compressive stress. For the additionally annealed sample, the isotropic lattice spacing, with equal in-plane and out-of-plane values, indicates a complete relaxation of the structure. Upon the thermal treatment, apart from annealing of defects, the residual stress can also be partially accumulated at the interface due to the fact that above 600°C plastic deformation occurs in the Si substrate [19]. In any case, the results show that the combination of post-annealing and medium-energy ion bombardment can be efficiently used to produce stress-free cBN by MS. For the samples grown under medium-energy ion bombardment, the in-plane and out-of-plane *d*(111) distances converge towards the value of the annealed sample with increasing ion-induced damage, in agreement with the macroscopic stress values displayed in Table 1. This is a clear indication that the ion bombardment leads to a strain relaxation at an atomic scale and within the cBN grains.

The size of the cBN grains is ~3 nm and ~6 nm for the out-of-plane and in-plane directions, respectively, as determined from the full width at half maximum (FWHM) of the cBN (111) reflection. These values are not affected by the ion bombardment nor by the annealing procedure, the latter in agreement with the observations by Donner *et al*. [11]. Hence, it can be stated that the medium-energy ion bombardment does not induce an amorphization nor a phase transformation of the cBN crystalline grains. High stability of the cBN phase against ion bombardment has also been reported by Eyhusen *et al.* [20]. Therefore, the observed macroscopic stress relaxation is mainly caused by a strain relaxation due to the removal of point defects within the cBN grains and not by a phase transformation into hBN. This process is likely the result of the thermal spikes induced by the medium-energy ion impacts, where the ratio of newly formed defects and annealed defects is very low for the considered ion energies [21]. The thermal spikes are also implied in the analytical model of ion-induced stress formation in thin films by Davis [22], to explain the stress reduction at higher ion energies. Therefore the stress in the cBN is effectively released by the medium energy-ion bombardment, although additional displacements are introduced.

Complementary to the results presented in this paper, infrared (IR) spectroscopy revealed a significant increase of hBN for ion damage values exceeding 1 dpa [10]. This phase transformation is not detected in the XRD analysis and could be understood considering the presence of an x-ray amorphous phase with mixed sp^2/sp^3 bonding that is less stable upon ion bombardment than the nanocrystalline cBN grains. In fact, it has been shown that a mixture of sp^2/sp^3 phases is not stable upon ion irradiation and transformation towards sp^2 occurs above a certain ion dose threshold [20]. Therefore, the increase in the hBN content detected by IR spectroscopy for large dpa must be attributed to a phase transformation in the amorphous matrix and not to a decrease of the cBN crystalline phase. In any case, this phase transformation can be minimized by using working conditions leading to an ion damage below the threshold value (1 dpa) while inducing similar amount of stress relaxation, as shown in Fig. 2. The results also indicate that the optimum ion-damage threshold could be increased and the relaxation process is more efficient by enhancing the crystallinity of the cBN phase during the growth.

In conclusion, XRD analysis has shown that effective stress relaxation in cBN thin films upon simultaneous medium-energy ion bombardment during the growth process takes place at an atomic scale. The crystalline cBN phase is very stable

under ion bombardment and the stress relaxation occurs within the cBN grains. The main path of stress relaxation seems to be annihilation of interstitials and atomic rearrangements as a result of the thermal spikes induced by the medium-energy bombardment. However, additional post-deposition annealing is required for complete relaxation of the structure. The stress relaxation process could be more efficient by operation under conditions leading to a higher crystallinity of the cBN phase.

Acknowledgements

We would like to acknowledge the financial support from the ESRF for the synchrotron experiments under project number ME-706. The help of Dr. N. Schell as local contact and the technical assistance of U. Strauch at ROBL are also much appreciated. The work at FZR has been supported by Deutsche Forschungsgemeinschaft (DFG) under contract No. FU 303/2-2.

The present results have been recently published as B. Abendroth *et al.*, Appl. Phys. Lett. **85** (2004) 5905.

References

[1] P.B. Mirkarimi, K.F. McCarty, D.L. Medlin, Mater. Sci. Eng. R. **21** (1997) 47

[2] W. Kulisch, S. Ulrich, Thin Solid Films **423** (2003) 183

[3] H. Hofsäss, S. Eyhusen, C. Ronning, Diam. Relat. Mater. **13** (2004) 1103

[4] J. Ullmann, A.J. Kellock, J.E.E. Baglin, Thin Solid Films **341** (1999) 238

[5] J. Ullmann, J. Baglin, E. Kellock, J. Appl. Phys. **83** (1998) 2980

[6] C. Fitz, W. Fukarek, W. Möller, Thin Solid Films **408** (2002) 155

[7] H.-G. Boyen, P. Widmayer, D. Schwertberger, N. Deyneka, P. Ziemann, Appl. Phys. Lett. **76** (2000) 709

[8] C. Fitz, A. Kolitsch, W. Möller, W. Fukarek, Appl. Phys. Lett. **80** (2002) 55

[9] R. Gago, M. Vinnichenko, B. Abendroth, A. Kolitsch, W. Möller, J. Vac. Sci. Technol. A **21** (2003) 1739

[10] B. Abendroth, R. Gago, A. Kolitsch, W. Möller, Thin Solid Films **447** (2004) 131

[11] W. Donner, H. Dosch, S. Ulrich, H. Erhardt, D. Abernathy, Appl. Phys. Lett. **73** (1998) 777

[12] C. Fitz, A. Kolitsch, W. Fukarek, Thin Solid Films **389** (2001) 173

[13] X.W. Zhang, H.-G. Boyen, P. Ziemann, M. Ozawa, F. Banhardt, M. Schreck, Diam. Relat. Mater. **13** (2004) 1144

[14] C. Fitz, W. Fukarek, A. Kolitsch, W. Möller, Surf. Coat. Technol. **128-129** (2000) 474

[15] J. Ziegler, J. Biersack, U. Littmark, The Stopping and Range of Ions in Solids, Pergammon Press, New York, 1985

[16] W. Matz, N. Schell, G. Bernhard, F. Prokert, T. Reich, J. Claußner, W. Oehme, R. Schlenk, S. Dienel, H. Funke, F. Eichhorn, M. Betzl, D. Pröhl, U. Strauch, G. Hüttig, H. Krug, W. Neumann, V. Brendler, P. Reichel, M.A. Denecke, H. Nitsche, J. Synchrotron Rad. **6** (1999) 1076

[17] D.L. Medlin, T.A. Friedmann, P.B. Mirkarimi, P. Rez, M.J. Mills, K.F. McCarty, J. Appl. Phys. **76** (1994) 295

[18] Joint Committee on Powder Diffraction Standards (JCPDS), pattern 25-1033

[19] K. Yasutake, J. Murakami, M. Umeno, H. Kawabe, Jap. J. Appl. Phys. **21** (1982) L288

[20] S. Eyhusen, I. Gerhards, H. Hofsäss, C. Ronning, M. Blomenhofer, J. Zweck, M. Seibt, Diam. Rel. Mat. **12** (2003) 1877

[21] F. Seitz, J. Koehler, Solid State Phys. **3** (1956) 305

[22] C. Davis, Thin Solid Films **226** (1993) 30

Mechanisms of Target Poisoning during Magnetron Sputtering as Investigated by Real-Time *in situ* Analysis and Collisional Computer Simulation

D. Güttler, B. Abendroth, R. Grötzschel, W. Möller and D. Depla[1]

[1]*Dept. Solid State Sciences, University of Ghent, Gent, Belgium*

Magnetron sputtering [1-3] is one of the most frequently applied tools for the deposition of high-quality functional coatings. For high-rate deposition, sputtering of compound films is often performed in the "reactive" mode [4,5], where a metal target is exposed to a discharge in a rare gas with some fraction of reactive gas (such as oxygen or nitrogen) added. The performance of reactive sputtering is, however, impeded by the effect of target "poisoning", which means that a compound film is not only formed on the substrate as desired, but also on the sputter target, which results in a significantly reduced sputter yield and, thereby, reduced deposition rate. A further consequence of poisoning is a hysteresis of the reactive gas partial pressure at increasing/decreasing reactive gas flow, and, associated to this, an unstable operation regime between high and low target uptake at constant partial flow of the reactive gas, which often requires additional means of stabilization in practical applications [4,6]. These phenomena have been quantitatively described by a global stationary analytical model [7,8] taking into account the reactive gas balance and a saturable reactive gas chemisorption on the surface of both the target and the other surrounding surfaces including the substrate. These models have been validated semi-quantitatively (e.g., Refs. 4, 9 and 10) by comparing their predictions to experimental findings, which relate the external process parameters such as ingoing flow and partial pressure of the reactive gas to the film deposition rate and stoichiometry. Recently, it has been proposed that, in addition to surface adsorption, ion implantation affects the target uptake [11]. This has also been studied by collisional computer simulation in dynamic mode [12] using the TRIDYN [13,14] code. So far, however, no direct experimental evidence has been given on the presence and the amount of the reactive gas uptake in the target during the reactive sputtering process. Even *ex situ* measurements after deposition [15] would not allow for unambiguous conclusions, as at least a fraction of the uptake might have transient character, as, e.g., due to diffusion and/or desorption. A further complication arises from the laterally inhomogeneous plasma-surface interaction at the target, which is due to the toroidal shape of a magnetron plasma, and the corresponding formation of the erosion "race track". Therefore, an experiment has been designed which allows for real-time *in situ* analysis of the reactive element uptake at the target surface, with the aims (i) to perform for the first time quantitative measurements of the reactive gas uptake in the target during the sputtering process and at varying lateral positions on the surface, (ii) to demonstrate the predicted hysteresis effect also for the target uptake, and (iii) to identify any transients of the target uptake after switching off the plasma.

A standard magnetron sputter configuration was installed in an ultrahigh vacuum chamber attached to the beam line system of a 5 MV tandem ion accelerator. A planar circular DC magnetron of 2" diameter was equipped with a 99.995% purity titanium target and positioned in front of a grounded stainless steel substrate plate at a distance of 10 cm. Due to differential pumping, a beam line pressure of $< 10^{-6}$ mbar was maintained at an operating pressure around 3×10^{-3} mbar in the processing chamber. A fixed argon flow of 10.4 sccm and a variable nitrogen flow up to 2 sccm were admitted using flow controllers. The partial pressures of the gases were measured by means of a quadrupole mass spectrometer, which was calibrated in pure Ar and N_2, respectively. The magnetron was operated in constant current mode at $I = 0.3$ A, resulting in a target voltage around 340 V. The analysing beam of 1.8 MeV D^+ ions with a typical current of 40 nA was directed onto the target surface through a small hole in the substrate plate. The size of the beam spot was 1.5×2 mm^2. A tilt mechanism at the magnetron suspension allows for the analysis of different radial positions on the target surface. The α particle yields from the $^{14}N(d,\alpha_0)^{12}C$ and $^{14}N(d,\alpha_1)^{12}C^*$ nuclear reactions were measured by means of a surface barrier detector behind a second hole in the substrate plate. The detector was covered by a thin metal foil in order to prevent any contact with the plasma. In addition, a moveable holder with additional exchangeable foils was

installed between the substrate plate and the detector to prevent the latter from film deposition which would cause an excessive energy loss of the emitted α particles. Due to the high *Q* value of the employed nuclear reaction, background-free energy spectra are obtained at ~ 9 and ~ 6 MeV for the α_0 and α_1 reaction channels. The integral yield of the peaks is proportional to the areal density of nitrogen in the target surface. The calibration of the areal density was performed by means of a Ti sample implanted with $(1 \pm 0.02) \times 10^{17}$ N^+/cm^2 at 150 keV resulting in a mean depth of 200 nm. By time-dependent analysis of the nitrogen areal density with the magnetron switched off, it was assured that there is no release of nitrogen induced by the analysing ion beam. Due to the low cross section of the nuclear reaction, the convenience of the present experiment is hampered by long analysis times of 30 min and more, which still yield no more than about 100 counts of the α spectra. This, however, does not deteriorate other than the statistical quality of the results as all measurements have been performed in stationary state.

Figure 1(a) displays the evolution of the nitrogen uptake in the centre of the race track at varying nitrogen gas flow, as obtained during magnetron sputtering. (The variation of the nitrogen uptake across the entire area of the target is less than about ± 50 %.) As in the evolution of the nitrogen partial pressure (Fig. 1(b)), the expected transition from metallic to poisoned mode at low and high nitrogen flow, respectively, is observed, being accompanied by the hysteresis effect. Whereas the partial pressure data are in qualitative agreement with findings described in literature (e.g., Ref. 16), the dynamic reactive gas uptake is measured for the first time during magnetron processing. The results are qualitatively consistent with earlier predictions by analytical modelling [7,8]. However, the absolute nitrogen content at high nitrogen flow significantly exceeds the areal density of one adsorbed monolayer, which indicates that other mechanism than surface adsorption only govern the nitrogen uptake. This will be further discussed below.

When comparing the target nitrogen content during magnetron operation and after switching off the magnetron, no nitrogen loss was observed within the experimental errors in any of the experiments. This is also shown in Fig. 1 for selected data. This indicates the absence of a significant mobile fraction of incorporated nitrogen in addition to the chemically bound one, and is in contrast to the interpretation of target voltage measurements after switching off the magnetron [17], which, however, were performed for the reactive sputtering of compounds other than TiN.

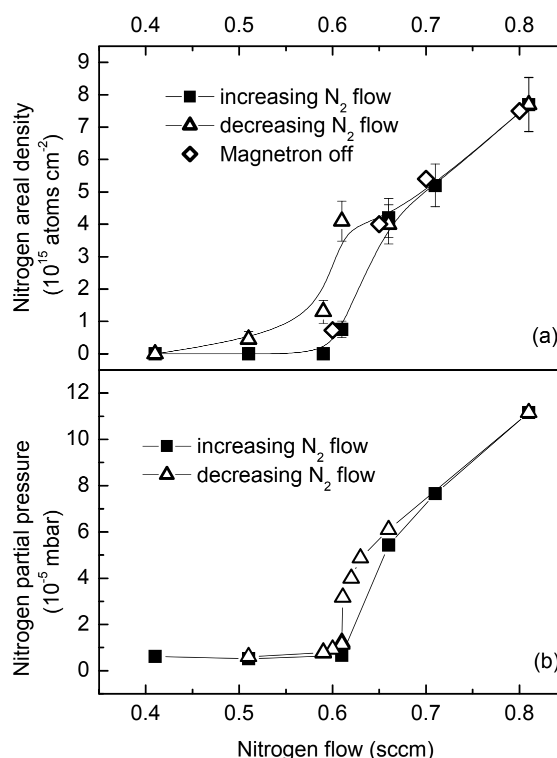

Fig. 1: Nitrogen uptake of the target surface (a) and nitrogen gas partial pressure (b) during sputter magnetron operation, at increasing (full squares) and decreasing (open triangles) nitrogen flow. The argon gas flow was 10.4 sccm. Location of the analysis is the centre of the race track. The diamonds denote the respective nitrogen uptake after switching off the magnetron.

Figure 2 shows the nitrogen partial pressure during operation and the target uptake measured after switching off the magnetron. At increasing nitrogen flow, the target uptake saturates around 1.05×10^{16} N/cm^2. Again, this number clearly exceeds one adsorbed monolayer. This contradiction to earlier models [7,8] can be explained by ion implantation of reactive ions into the target surface. In order to quantify this effect, dynamic collisional computer simulations have been performed using the TRIDYN [13,14] program for different ratios of the nitrogen and argon partial pressures. Due to similar electron impact ionisation cross sections for Ar and N_2 [18], the relative yields of Ar^+ and N_2^+ ions from an Ar/N_2 low-temperature plasma are roughly equal to the relative partial pressures. Ar^+ ions enter the target surface with the full energy eU_T, with e denoting the elementary charge and U_T the target voltage (the small addition due to the plasma potential is neglected). In contrast, for each N_2^+ ion two energetic nitrogen atoms enter at $eU_T/2$. Additionally, 0.25 N^+ ions impinge on the surface at full energy per each incident N_2^+ ion, which is typical for this kind of discharges, see, e.g., Refs. 19 and 20. From the target current, the laterally averaged total ion flux can be estimated to about

1×10^{17} cm^{-2} s^{-1}, as secondary electron emission is small [21]. Furthermore, there are two possible sources of thermal nitrogen atoms available for adsorption. At an N_2 admixture of 10 % and a total pressure of 0.3 Pa, the neutral molecules deliver a flux of 1.5×10^{17} cm^{-2} s^{-1} nitrogen atoms to the surface, with an unknown sticking coefficient. Alternatively, atomic nitrogen originates from the electron-induced dissociation in the plasma. The corresponding surface flux is expected to be significantly smaller than from the molecules, but difficult to quantify. Therefore, three series of calculations have been performed, (i) with the neutral nitrogen flux neglected, (ii) with the neutral nitrogen flux given by the reactive gas molecules at unity sticking, and (iii) with an N^0/N_2^+ ratio of 2. The latter choice is in correspondence to the cross sections for electron impact ionisation and dissociation of N_2 [22], and in rough agreement with the N^0/N_2^+ density ratio in the plasma, which is given in Ref. 20 for an Ar/N_2 plasma at an, however, tenfold higher total pressure. In this way, the composition of the incident flux is defined for a varying partial pressure ratio. Any uptake of Ar ions is neglected. The bulk concentration of nitrogen is limited to stoichiometric TiN, with excess nitrogen being modelled to be reemitted into the vacuum by infinitely fast diffusion. An initial target depth spacing of 0.25 nm is chosen, which corresponds to about one monolayer of Ti in the virgin state, so that the limitation of the nitrogen concentration at the surface corresponds to a saturable adsorption at about one monolayer. The surface binding energies of nitrogen and titanium, which determine the sputtering yields critically, are varied with the surface composition according to a formalism described in Ref. 23, which balances the surface binding energies with the sublimation energy of Ti, the molecular binding energy of nitrogen, and the formation energy of the TiN compound. The results of the computer simulation are shown in Fig. 2. Reasonable agreement with the experimental data is achieved when both implantation of energetic ions and surface adsorption of thermal nitrogen atoms are included, with an N^0/N_2^+ ratio of 2. In contrast, the experimental data cannot be reproduced by simulations with energetic ions only. On the other hand, assuming the full flux of reactive gas to the surface being available for reaction overestimates the nitrogen uptake at low nitrogen flux considerably. The saturated nitrogen content at high nitrogen flow corresponds to a TiN layer of 2.5 nm thickness. The ~10 % deviation from the experimental data is consistent with the uncertainty of ion ranges in compounds.

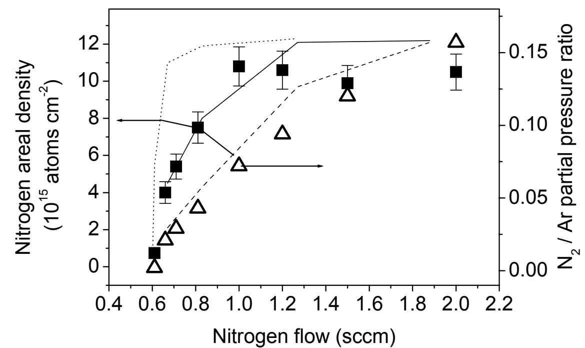

Fig. 2: Nitrogen-to-argon partial pressure ratio (right scale, open triangles) and nitrogen areal density at the target surface (left scale, full squares) at increasing reactive gas flow, as obtained after switching off the magnetron. Location of analysis is the center of the racetrack. The nitrogen areal density has also been calculated by TRIDYN computer simulation, with different N_2/Ar partial pressure ratios, with the relation between reactive gas flow and partial pressure ratio as given by the experimental data, and for nitrogen ion implantation and full sticking of the nitrogen molecules corresponding to an atomic nitrogen flux with $N^0/N_2^+ = 15$ (dotted line), nitrogen ion implantation and an atomic nitrogen flux with $N^0/N_2^+ = 2$ (solid line), and nitrogen ion implantation only (dashed line). At high N_2/Ar partial pressure ratio, the calculated areal density corresponds to 2.5 nm of stoichiometric TiN.

The collisional computer simulation describes the stationary nitrogen depth profiles as resulting primarily from the adsorption and recoil implantation of thermal nitrogen atoms, ion implantation of energetic ions, and sputtering. The comparison to the experimental results suggests that both ion implantation and surface adsorption are effective. The significance of ion implantation is basically consistent with the recent suggestion by Depla *et al.* [11] that ion implantation has to be taken into account for the description of plasma-target interaction during magnetron sputtering, and with very recent analytical modelling of the reactive sputtering kinetics taking into account ion implantation [12]. In addition, the satisfactory fit with the intermediate N^0/N_2^+ flux ratio of 2 might indicate that mainly N^0 constitutes the adsorbed nitrogen flux, rather than N_2. This, however, would have to be further corroborated by an improved knowledge about the individual fluxes and sticking coefficients.

The integrated content of nitrogen in the target surface amounts to roughly 10^{17} atoms. At the given pressure and a nitrogen relative partial pressure of 10%, the number of nitrogen atoms in the gas volume of a 5 liter reactor amounts to about 10^{17} as well. Compared to earlier understanding with an adsorbed monolayer only, this ratio of the target and gas nitrogen inventories is largely enhanced. With respect to practical applications,

this might be of importance in particular for the understanding of transient phenomena.

In summary, a deeper understanding on the plasma-target interaction during reactive magnetron sputtering has been achieved by means of real-time *in situ* target analysis and collisional computer simulation. The stationary uptake of nitrogen in a titanium target, which is laterally non-uniform across the target, results from a balance of nitrogen surface adsorption, nitrogen ion implantation, and sputtering caused by nitrogen and argon ions. There is no evidence of a mobile fraction of nitrogen which would be released after switching off the plasma.

Acknowledgements

The authors are indebted to R. de Gryse and S. Berg for helpful comments and critical discussions, and A. Rogozin and M. Mäder for assistance in setting up the experiment and ion beam analysis, respectively.

The present results have been previously published as D. Güttler *et al.*, Appl. Phys. Lett. **85** (2004) 6134.

References

[1] R.F. Bunshah, Handbook of Deposition Technologies for Films and Coatings, Noyes Publ., Park Ridge, 1984.

[2] P.Eh. Hovsepian, D.B. Lewis, W.-D. Münz, Surf. Coat. Technol. **133** (2000) 166

[3] J.M. Schneider, S. Rhode, W.D. Sproul, A. Matthews, J. Phys. D **33** (2000) R173

[4] I. Safi, Surf. Coat. Technol. **127** (2000) 203

[5] A.A. Voevodin, P. Stevenson, C. Rebholz, J.M. Schneider, A. Matthews, Vacuum **46** (1995) 723

[6] T. Wallendorf, S. Marke, C. May, J. Strümpfel, Surf. Coat. Technol. **174-175** (2003) 222

[7] S. Berg, H-O. Blom, T. Larsson, C. Nender, J. Vac. Sci. Technol. A **5** (1987) 202

[8] T. Larsson, H-O. Blom, C. Nender, S. Berg, J. Vac. Sci. Technol. A **6** (1988) 1832

[9] E. Kusano, J. Appl. Phys. **70** (1991) 7089

[10] R. Mientus, K. Ellmer, Surf. Coat. Technol. **116** (1999) 1093

[11] D. Depla, R. De Gryse, Surf. Coat. Technol. **183** (2004) 184; **183** (2004) 190; **183** (2004) 196

[12] O. Kappertz, D. Rosen, T. Nyberg, I. Katardjiev, S. Berg, Int. Conf. on Metallurgical Coatings and Thin Films, San Diego, California, USA, 2004

[13] W. Möller, W. Eckstein, Nucl. Instr. Meth. B **2** (1984) 814

[14] W. Möller, W. Eckstein, J.P. Biersack, Comp. Phys. Comm. **51** (1988) 355

[15] L. Combadiere, J. Machet, Surf. Coat. Technol. **82** (1996) 145

[16] A.F. Hmiel, J. Vac. Sci. Technol. A **3** (1985) 592

[17] D. Depla, R. De Gryse, Vacuum **69** (2003) 529

[18] H.S.W. Massey, E.H.S. Burhop, Electronic and Ionic Impact Phenomena, Oxford University Press, London, 1956

[19] J. Neidhardt, L. Hultman, B. Abendroth, R. Gago, W. Möller, J. Appl. Phys. **94** (2003) 7059

[20] F. Debal, J. Bretagne, M. Jumet, M. Wautelet, J.P. Dauchot, M Hecq, Plasma Sources Sci. Technol. **7** (1998) 219

[21] M.A. Lewis, D.A. Glocker, J. Jorne, J. Vac. Sci. Technol. A **7** (1989) 1019

[22] Y. Itikawa, M. Hayashi, A. Ichimura, K. Onda, K. Sakimoto, K. Takayanagi, M. Nakamura, H. Nishimura, T. Takayanagi, J. Phys. Chem. Ref. Data **15** (1986) 985

[23] W. Möller, M. Posselt, TRIDYN_FZR User Manual, Report FZR-317, Forschungszentrum Rossendorf, 2001

Ion Beam Induced Destabilization of Icosahedral Structures in Gas Phase Prepared FePt Nanoparticles

B. Rellinghaus[1], O. Dmitrieva[2], M.O. Liedke and J. Fassbender

[1]*Leibniz Institute for Solid State and Materials Research, IFW Dresden, Helmholtz-Strasse 20, D-01069 Dresden, Germany*

[2]*Experimentalphysik, Universität Duisburg-Essen, D-47048 Duisburg, Germany*

Multiply twinned FePt nanoparticles with icosahedral structures were prepared by DC magnetron sputtering in argon. The icosahedral structure of these particles is known to be very stable against structural transformations into both the face-centered cubic phase (fcc, *A1*) and the chemically ordered tetragonal $L1_0$ phase upon in-flight or post-deposition thermal annealing. Irradiation of these multiply twinned FePt particles with 5 keV He ions, however, resulted in a transformation into predominantly single crystalline fcc particles at high ion fluences of $f > 10^{17}$ ions/cm^2. Adjacent particles were observed to coalesce under the effect of He irradiation, and the size of individual particles was found to be slightly reduced, which indicates a high atomic mobility owing to temporarily enhanced defect concentrations caused by the ion bombardment. Strikingly, there was no indication for the occurrence of $L1_0$ ordered FePt nanoparticles upon ion irradiation in these samples.

Owing to its large magneto-crystalline anisotropy energy, $L1_0$ ordered tetragonal FePt is among the most intensively discussed materials when it comes to pushing the superparamagnetic limit towards minimum particle sizes for future ultra-high density magnetic data storage media [1]. Depending on the preparation technique, however, the formation of the $L1_0$ thermodynamic equilibrium phase is often impeded by either a lack of thermodynamic driving forces or a lack of diffusivity. Unfortunately, the thermodynamic driving force is largest for low temperatures, whereas the diffusivity is largest for high temperatures [2]. As an immediate consequence of this dilemma, narrow particle size distributions, periodic particle arrangements, the formation of the $L1_0$ phase, and perpendicular magnetic textures as required for data storage applications have only been partially realized, so far. The simultaneous fulfilment of all these requirements has not yet been achieved. One approach to overcome theses difficulties is the attempt to reduce the kinetic ordering temperature (e.g. by adding a third element such as Cu, Ag, Au) to temperatures at which inter-particle sintering does not yet set in [3]. This would allow for maintaining the periodic particle arrangement as obtained from wet-chemical preparation techniques upon thermal annealing. Alternatively, the potential of ion irradiation for the promotion of the $L1_0$ order in intermetallic thin films and nanoparticles by virtue of the creation of enhanced defect concentrations is investigated [4,5]

In order to provide better control of the formation of the $L1_0$ phase, a thorough understanding of both the thermodynamic equilibrium phases and the ordering kinetics at the nanometer length scale is essential though still lacking. E.g., in contrast to bulk FePt alloys, the observation of FePt multiply twinned particles (MTPs) with icosahedral, decahedral, and more complex structures are observed [6-8]. Strikingly, these MTPs were found to be stable even upon post-deposition thermal annealing at temperature of up to T_{ann} = 1000°C [8]. On the other hand, when the formation of MTPs is suppressed by varying the preparation conditions, thermal annealing is known to promote the formation of $L1_0$ order in FePt nanoparticles [6]. Therefore, investigations which aim at understanding the relative stability and the transformations of different structural phases in FePt nanoparticles are of substantial interest to the community.

FePt nanoparticles were prepared by DC magnetron sputtering from FePt alloy targets in argon at elevated pressures of p_{Ar} = 0.5 mbar. The primary particles are carried in a continuous gas flow through a tube furnace where they can be exposed to annealing temperatures of up to T_{ann} = 1000°C prior to being deposited onto amorphous carbon films. Experimental details are published elsewhere [6]. Structural investigations were carried out with high resolution transmission electron microscopy (HRTEM) utilizing a Philips Tecnai F20 microscope (200 kV, field emission gun), and the composition of the particles was determined by energy dispersive X-ray spectrometry (EDXS) using an EDAX Phoenix system equipped with a sapphire detector. Some of the He deposited particles were then irradiated with 5 keV

ions at fluences in the range 1×10^{16} ions/cm^2 $\leq f \leq$ 3×10^{17} ions/cm^2 at room temperature (RT). For the ion bombardment, a commercial VG Microtech EX05 ion source is used which is attached to an ultra high vacuum system. The base pressure during He ion irradiation is 5×10^{-8} mbar. The ion fluence is set by measuring the ion current in a Faraday cup and varying the exposure time. The effect of the ion bombardment on the crystal structure of the FePt nanoparticles was determined from a comparison of the HRTEM result before and after irradiation.

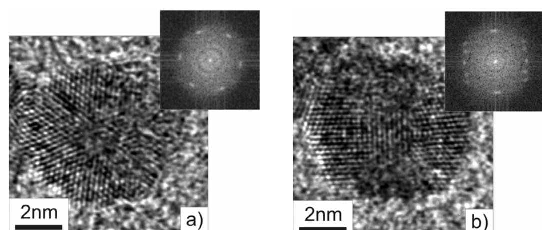

Fig. 1: As-prepared $Fe_{42}Pt_{58}$ nanoparticles from the gas phase: Multiply twinned particles of icosahedral structure as seen along one of their 3-fold (Fig. 1a) and along a 2-fold symmetry axes (Fig. 1b), respectively. The inserts show the Fourier transform of the original image.

Recently, it has been shown that FePt nanoparticles with concentrations in the vicinity of the stoichiometric composition are predominantly multiply twinned particles (MTPs) of icosahedral structure when they are prepared and annealed in the gas phase at $p_{Ar} = 0.5$ mbar and $T_{ann} = 600$°C [8]. Figure 1 shows exemplarily the HRTEM micrographs of two typical $Fe_{42}Pt_{58}$ nanoparticles as obtained from a preparation under these conditions. The depicted particles are icosahedral MTPs as seen along one of their 3-fold (Fig. 1a) and one of their 2-fold symmetry axes (Fig. 1b), respectively. The symmetry is nicely reflected in the power spectra as obtained by Fourier transform of the original images (see inserts in Fig 1). The mean diameter of the as-deposited particles was d_P = 6.2 nm.

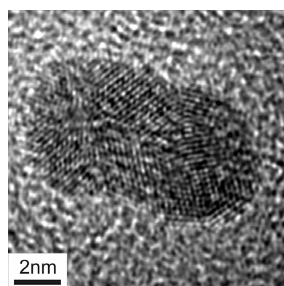

Fig. 2: Adjacent $Fe_{49}Pt_{51}$ nanoparticles after exposure to 5 keV He irradiation at an intermediate fluence of f = 3×10^{16} ions/cm^2: Onset of sintering.

Figure 2 shows the typical HRTEM image of two adjacent $Fe_{49}Pt_{51}$ particles ($p_{Ar} = 0.5$ mbar, $T_{ann} = 600$°C) which have been exposed to 5 keV He ion irradiation at a moderate fluence of f = 5×10^{16} ions/cm^2. It is obvious from Fig. 2 that the particles are mutually connected via a pronounced sintering neck. Whereas in the case of as-deposited particles, adjacent icosahedra are known to exhibit minimum contact areas [8], the observation of sintering necks in the ion irradiated particles reveals that the He irradiation treatment promotes the onset of inter-particle sintering at RT. This is attributed to the formation of vacancies during the ion irradiation. Nonetheless, the signature of the icosahedral structure in the primary particles the dumbbell-shaped particle dimer in Fig. 2 is composed of is still present. This indicates that the irradiation induced defect concentration is too small to allow for a structural phase transformation at RT.

This situation is changed upon increasing the fluence to values as high as $f = 3 \times 10^{17}$ ions/cm^2. In Fig. 3, two typical HRTEM micrographs are presented which are obtained from the $Fe_{42}Pt_{58}$ particles depicted in Fig. 1 after being irradiated with 5 keV He ions at $f = 3 \times 10^{17}$ ions/cm^2. The particles are no longer MTPs but rather single crystal fcc. Although polycrystalline fcc particles (with few remaining twin boundaries) are also observed in this sample, it is noteworthy to state that there are virtually no MTPs present in the irradiated sample. The mean diameter of the irradiated particles is observed to be reduced to $d_P^{irr} = 5.2$ nm. This size reduction is ascribed to irradiation induced sputtering of the particles. A simple model calculation utilizing the Monte Carlo method within the SRIM software package [9] was carried out to provide evidence for this interpretation. Assuming a continuous $Fe_{42}Pt_{58}$ thin film with a thickness of $d = 4.1$ nm (i.e. the thickness with the same volume-to-projection-area ratio as compared to a spherical particle with $d_P = 6.2$ nm) supported by 10 nm of carbon, a sputtering yield of 0.07 atoms/ion was obtained.

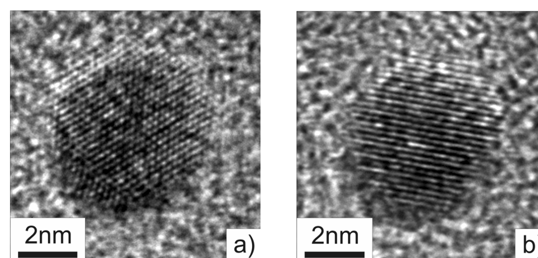

Fig. 3: $Fe_{42}Pt_{58}$ nanoparticles after exposure to 5 keV He irradiation at a maximum fluence of $f = 3 \times 10^{17}$ ions/cm^2. The previously multiply twinned particles have transformed into fcc single crystals.

With the given fluence and particle size ($f = 3 \times 10^{17}$ ions/cm^2, $d_P = 6.2$ nm) the relative number of sputtered atoms per particle was estimated to be as high as 70 %. On the other hand, the measured reduction of the particle diameter is equivalent to a loss of only 40 % of the atoms. Within such an oversimplified estimation, however, the agreement is to be considered satisfying in order to support the assumption.

Although the defect concentration as imposed by an ion fluence of $f = 3 \times 10^{17}$ ions/cm^2 apparently increases the atomic diffusivity temporarily to an extent that allows for structural transformations in the FePt nanoparticles at RT, no $L1_0$ ordered particles have been observed. This observation is in contrast to the bulk phase diagram [10], theoretical calculations [11], and thermodynamic investigations in thin films [12], based on which the $L1_0$ phase is expected to be energetically favored over the fcc phase by some 0.1 eV/atom. Furthermore, although no theoretical investigations are available for FePt, a reduction in size is generally expected to result in a stabilization of the icosahedral over the fcc structure in materials which are fcc in their bulk form (see, e.g., [13]).

There are two possible origins for the experimental findings reported in this paper. Recently, both experimental and theoretical investigations point to the existence of a critical particle size limit below which the $L1_0$ phase is no longer the thermodynamic equilibrium phase in FePt [14]. This energetic de-favourization is owed to the increasing weight of surface energy contributions (surface free energy, segregation energy, interfacial energy) to the total energy of the finite size particle. Depending on the method of investigation, this critical particle size is estimated to lie in the range 1.5 nm $\leq d_P^* \leq$ 6 nm. Secondly, kinetic aspects may be of increasing importance at these length scales. Whereas in FePt thin films, ion irradiation is found to promote the formation of $L1_0$ order, irradiation of FePt nanoparticle under identical conditions does not result in the ordered phase [5]. Since the sputtering process that comes along with the ion irradiation is element specific and tends to remove more iron atoms than platinum atoms, the He ion irradiation results in a shift of the elemental composition of the FePt nanoparticles towards a more Pt-rich concentration. As a consequence, the remaining alloy approaches the borderline of the $L1_0$ stability region in the phase diagram. Concurrently, the thermodynamic ordering temperature is reduced and the chemical driving force for the $L1_0$ ordering will be significantly reduced.

FePt nanoparticles were prepared from the gas phase under conditions at which these particles are predominantly icosahedral MTPs. It has been shown that irradiation with 5 keV He ions at fluences of $f = 3 \times 10^{17}$ ions/cm^2 leads to a structural transformation into poly and (preferentially) single crystal fcc particles. The observed reduction in particle size was shown to be due to sputtering effects during the ion irradiation. Most strikingly, the chemically ordered $L1_0$ phase which is the thermodynamic equilibrium structure in the according bulk material, was not observed. This indicates that either kinetic effects dominate over thermodynamic equilibrium energetics or the $L1_0$ structure is no longer the equilibrium phase for FePt nanoparticles with sizes of roughly 5 nm.

Acknowledgements

The authors are indebted to Dr. K.-H. Heinig for valuable discussions. Financial support for part of this work by the Deutsche Forschungsgemeinschaft within SFB 445 is gratefully acknowledged.

References

[1] D. Weller, A. Moser, IEEE Trans. Mag. **35** (1999) 4423; D. Weller, A. Moser, L. Folks, M.E. Best, W. Lee, M.F. Toney, M. Schwickert, J.-U. Thiele, M.F. Doerner, IEEE Trans. Mag. **36** (2000) 10

[2] T.J. Klemmer, C. Liu, N. Shukla, X.W. Wu, D. Weller, M. Tanase, D.E. Laughlin, W.A. Soffa, J. Magn. Magn. Mater. **266** (2003) 79

[3] T. Maeda, A. Kikitsu, T. Kai, T. Nagase, J.I. Akiyama, Appl. Phys. Lett. **80** (2002) 2147; S. Kang, J.W. Harrell, D.E. Nikles, Nano Lett. **2** (2002) 1033

[4] D. Ravelosona, C. Chappert, V. Mathet and H. Bernas, Appl. Phys. Lett **76** (2000) 236; H. Bernas, J.-Ph. Attane, K.-H. Heinig, D. Halley, D. Ravelosona, A. Marty, P. Auric, C. Chappert, Y. Samson, Phys. Rev. Lett. **91** (2003) 077203

[5] S. Matsumura, T. Horiuchi, K. Yasuda, M. Watanabe, T. Masumoto, $L1_0$-conference, Copper Mountain, CO, USA, 15.-20.08.2004

[6] S. Stappert, B. Rellinghaus, M. Acet, E.F. Wassermann, J. Cryst. Growth **252** (2003) 440

[7] B. Rellinghaus, S. Stappert, M. Acet, E.F. Wassermann, J. Magn. Magn. Mater. **266** (2003) 142

[8] S. Stappert, B. Rellinghaus, M. Acet, E.F. Wassermann, Proc. Mat. Res. Soc. Vol. **704** (2002) 73

[9] J.F. Ziegler, J.P. Biersack, U. Littmark, The stopping and Range of Ions in Solids, Pergamon Press, New York, 1985; SRIM-code: http://www.srim.org

[10] T.B. Massalski, J.L. Murray, L.H. Bennet, H. Baker (eds.), Binary Phase Diagrams, ASM International, Materials Park, Ohio, 1986, p. 1096

[11] J. MacLaren, $L1_0$ conference, Copper Mountain, CO, USA, 15.-20.08.2004

[12] K. Barmak, J. Kim, S. Shell, E.B. Svedberg, J.K. Howard, Appl. Phys. Lett. **80** (2002) 4268

[13] C.L. Cleveland, U. Landman, J. Chem. Phys. **94** (1991) 7376

[14] Y.K. Takahashi, T. Koyama, M. Ohnuma, T. Ohkubo, K. Hono, J. Appl. Phys. **95** (2004) 2690; O. Mryasov, B. Yang, $L1_0$ conference, Copper Mountain, CO, USA, 15.-20.08.2004

Short Contributions

Ion-Solid-Interaction

S. Facsko
D. Kost
Z. Pešić[1]
R. Hellhammer[1]
N. Stolterfoht[1]

Relaxation of hollow atoms below the SiO_2 surface

The secondary electrons emitted during the interaction of highly charged ions with solid surfaces carry detailed information about the complex interaction mechanism. We studied the emission of electrons from Ne^{9+} interacting with thin SiO_2 films. The typical LMM and KLL Auger electrons resulting from the last steps in the neutralisation process of the ions are observed on top of a broad secondary electron background. Comparing the electron spectra at different thickness from 100 nm to 5 nm a continuous shift to lower energy is observed. In addition, at extrapolated zero thickness the Auger electron energy is still shifted by 30 eV for the KLL and 20 eV for the LMM peak compared to a metallic surface. Two mechanisms were identified for this: the macroscopic charging of the SiO_2 surface induces a linear shift with thickness, whereas the weaker screening of the Ne ions in the SiO_2 film causes the residual shift at zero thickness.

Collaboration: [1]Hahn-Meitner Institut, Bereich Strukturforschung, Berlin

D. Kost
S. Facsko
Z. Pešić[1]
R. Hellhammer[1]
N. Stolterfoht[1]

Potential energy retention and reemission of highly charged ions

A major interest in the interaction of highly charged ions with solid surfaces lies in the study of the dissipation channels for the potential energy. In order to support former calorimetric measurements of the retained potential energy, we have determined the fraction of the potential energy which is reemitted by the secondary electrons. Double differential electron spectra were measured at three different emission angles for Ar^{8+} with kinetic energies of 500 – 1800 eV incident onto Au. The total amount of energy was obtained by integrating over the electron energy and the emission angle. A fraction of reemitted potential energy by the secondary electrons of 15% is obtained being almost independent on their kinetic energy. The results are in good agreement with the calorimetric measurements, thus confirming that secondary electrons carry the predominant part of reemitted potential energy.

Collaboration: [1]Hahn-Meitner Institut, Bereich Strukturforschung, Berlin

S. Facsko
T. Bobek[1]
A. Stahl[1]
H. Kurz[1]
T. Dekorsy

Dissipative continuum equation for the self-organized nanopatterning of semiconductor surfaces by ion beam erosion

A continuum model, based on the damped Kuramoto-Sivashinsky equation, has been applied for the simulation of the occurrence and evolution of uniform and ordered dot patterns during ion beam erosion of semiconductor surfaces. This continuum equation reproduces the morphology evolution successfully, including the appearance of regular dot structures under normal incidence of ions and the saturation of the dot pattern in time. In addition, depending on the value of the damping parameter α, three different regimes of morphology evolution were identified: smoothing of the surface for large values of α, hexagonal dot patterns for a narrow range of α around 0.25, and kinetic roughening, typically for the undamped Kuromoto-Sivashinsky equation, for low values of α. All of these morphology evolutions are also found in ion beam erosion experiments. The origin of the damping term is proposed to be a first approximation to a novel term in the continuum equation describing the redeposition of sputtered particles which play a significant role at high aspect rations of the formed structures.

Collaboration: [1]Institut für Halbleitertechnik, RWTH Aachen

C. Neelmeijer
D. Jembrih-Simbürger[1]

Art Nouveau glass work studied non-destructively by IBA

Art Nouveau glass fragments from Tiffany/USA and Loetz/Austria were selected and characterized at the external proton beam. Previous studies

M. Mäder[1]
M. Schreiner[1]

(PIXE-RBS) already identified thin tin containing glass top layers as the origin of iridescence. Further X-ray and γ-ray (PIXE / PIGE) investigations were performed for glass bulk analysis and of glass overlay identification. Loetz used potash-lime silica glass as bulk material whereas the Tiffany bulk glass was of borosilicate type containing around 40 wt% of lead oxide. Silver (0.1 – 0.4 wt% Ag_2O) was always found in the uppermost glass material. Until now it has not been clarified whether the addition of silver contributes to the phenomenon of iridescence.

Collaboration: [1]Wissenschaften und Technologie in der Kunst, Akademie der bildenden Künste Wien, Österreich

Thin Films

R. Gago
M. Vinnichenko[1]
H.U. Jäger
A.Yu. Belov[2]
I. Jiménez[3]
N. Huang[4]
H. Sun[4]
M.F. Maitz

Evolution of sp^2 networks with substrate temperature in amorphous carbon films: experiment and theory

The evolution of sp^2 hybrids in amorphous carbon (a-C) films deposited at differrent substrate temperatures was studied experimentally and theoretically. The bonding structure of a-C prepared by filtered cathodic vacuum arc was assessed by the combination of visible Raman spectroscopy, x-ray absorption spectroscopy and spectroscopic ellipsometry. The experimental results show a transition from tetrahedral a-C (ta-C) to sp^2-rich structures at ~ 250°C. The sp^2 hybrids are mainly arranged in small olefinic (chain-like) clusters and graphitic structures are only promoted for sp^2 fractions above 80%. Molecular-dynamics simulations of the growth process with a modified version of the Brenner potential reproduce the preferred pairing of sp^2 sites in ta-C as well as the pronounced formation of rings for sp^2 fractions > 80%. However, the theoretical results do not predict the dominance of sixfold rings in sp^2-rich samples.

Collaboration: [1]Physics Department, Kyiv Taras Shevchenko University, Ukraine; [2]Technische Universität Dresden, Institut für Werkstoffwissenschaft; [3]Instituto de Ciencia y Tecnología de Polímeros, Madrid, Spain; [4]College of Materials Science and Engineering, Southwest Jiaotong University, Chengdu, China

A.Yu. Belov[1]
H.U. Jäger

Relaxation kinetics in amorphous carbon films: an insight from atomic scale simulation

Using molecular-dynamics techniques and a hydrocarbon potential of Brenner with an increased carbon-carbon interaction range, the kinetics of relaxation processes in tetrahedral amorphous carbon films (ta-C) with high sp^3 fractions was studied. Annealing at a temperature of 1000 K reduces both film stress and energy exponentially with annealing time, satisfying a simple rate equation. The exponential dependency can be interpreted in terms of structural transformations in the amorphous carbon networks. The relaxation times for the energy and stress do not coincide, indicating that some atomic rearrangements in the networks may reduce their energy without changing the stress. The relaxation constant for energy was found to be in the range of 0.5 – 0.7 ns, which considerably exceeds an estimate of 10 ps for the thermalization stage of the subplantation model for ta-C film formation by energetic C ions.

Collaboration: [1]Technische Universität Dresden, Institut für Werkstoffwissenschaft

A.Yu. Belov[1]
H.U. Jäger

Formation and evolution of sp^2 clusters in amorphous carbon networks as predicted by molecular dynamics annealing simulations

A theoretical comparative study of clustering of sp^2-bonded atoms in as-deposited and annealed tetrahedral amorphous carbon (ta-C) networks was performed. The “as-deposited ta-C films” were annealed in the temperature range of 600 – 1200 K, using molecular-dynamics. Size and type of the sp^2 clusters in the films were analyzed as a function of the annealing temperature as well as the model parameters for stress and temperature control. An essential finding of the study is that at a density less than 3.0 g/cm^3 the structure of ta-C can become unstable with respect to formation of large sp^2 clusters.

Collaboration: [1]Technische Universität Dresden, Institut für Werkstoffwissenschaft

G. Abrasonis
R. Gago
M. Vinnichenko[1]
A. Mücklich
U. Kreissig
A. Kolitsch

On the synthesis of fullerene-like CN_x by IBAD: role of film-forming species, ion bombardment and film growth rate

Carbon nitride CN_x ($0 \le x \le 0.28$) thin films, deposited by ion assisted sputtering (IAS) with various sputtering beam compositions at different temperatures and by electron beam evaporation of graphite with simultaneous low-energy nitrogen ion assistance (LE-IBAD), have been studied by the means of

W. Möller

infrared, Raman and X-ray near edge absorption spectroscopies, spectroscopic ellipsometry, ERDA and TEM. Nitrogen concentration in the films increases with the nitrogen content in the sputtering beam and decreases with temperature. The IAS film density variation with the composition presents two regimes: up to 150°C the density decreases with nitrogen content in the sputtering beam, while at temperatures above 150°C the density increases with nitrogen content. The promotion of the formation of pyridine-like and nitrile configurations are observed in the films prepared by IAS while nitrile groups are prevailing in the films prepared by LE-IBAD. Films grown at high growth rates (0.1 – 0.2 nm/s) by LE-IBAD are completely amorphous while the films grown at low growth rates (0.01 nm/s) by IAS can be characterized by small (~ 1-2 nm) ordered straight and curved domains embedded in the amorphous matrix. The microstructure of the films is a consequence of several concurrent processes such as temperature induced ordering and growth of graphene sheets, the nitrogen induced defect formation at the edges of graphite clusters due to pyridine-like configurations, and the film growth rate. The results suggest that one of the principal roles of the assisting low energy ion bombardment is the promotion of the growth of graphene sheets provided that the film growth rate is not too large.

Collaboration: [1]Department of Physics, Kyiv National Taras Shevchenko University, Kyiv Ukraine

T.W.H. Oates
L. Ryves[1]
F.A. Burgmann[2]
B. Abendroth
M.M.M. Bilek[1]
D.R. McKenzie[1]
D.G. McCulloch[2]

Ion-implantation induced phase transformation in carbon and boron nitride thin films

The mechanisms behind energetic ion-impact induced stress reduction in ta-C and BN thin films have been investigated by real-time *in-situ* spectroscopic ellipsometry and *ex-situ* electron microscopy. Highly stressed carbon and boron nitride films were grown by filtered cathodic vacuum arc and RF magnetron sputtering, respectively, and subsequently implanted by 5 – 10 keV Ar ions. In both cases the films were observed to expand due to a reduction in the density of the ion modified layer. Electron microscopy of the carbon films showed that this reduction in density is associated with a conversion of diamond-like bonding to graphite-like bonding. *In-situ* stress measurements performed on the boron nitride films revealed a simultaneous reduction in stress with expansion of the material.

Collaboration: [1]University of Sydney, School of Physics, Australia; [2]RMIT University, School of Applied Sciences, Australia

K. Graupner[1]
S. Peter[1]
D. Grambole

Investigations towards high-rate deposition of hard diamond-like carbon films

Amorphous, hydrogenated carbon films (a-C:H) were prepared by PECVD (13.56 MHz rf-plasma) from the source gases methane and acetylene with the aim to enable high growth rates while keeping films with high hardness (25 ± 3 GPa). The films were characterized in terms of deposition rate, micro-hardness, hydrogen content and surface roughness. The NRA analysis of the films deposited at 200°C substrate temperature revealed an homogenous hydrogen content across the whole film thickness. The hydrogen concentration of films deposited at pressures from 2 Pa to 15 Pa was determined to 29 at.% for films deposited with the source gas methane and between 22 ÷ 32 at.% using acetylene plasma. The investigations confirm that the film hardness and the hydrogen content of the films are determined by the ratio between the flux of energetic C_xH_y ions and the flux of film forming neutrals.

Collaboration: [1]Institut für Physik, Technische Universität Chemnitz

P. Danesh[1]
B. Pantchev[1]
K. Antonova[1]
E. Liarokapis[2]
B. Schmidt
D. Grambole
J. Baran

Hydrogen bonding and structural order in hydrogenated amorphous silicon prepared with hydrogen-diluted silane

The compositional and structural evolution of hydrogenated amorphous silicon (a-Si:H) films during PECVD with hydrogen-diluted silane has been studied. The total hydrogen concentration and its silicon-bonded fraction have been characterized by means of NRA and infrared (IR) spectroscopy, respectively. The content of molecular hydrogen is below the detection limits of the measurements. Hydrogen is uniformly distributed throughout the film thickness, and the IR absorption modes at 2000 cm^{-1} (monohydrides) and 2100 cm^{-1} (polyhydrides or clustered monohydrides) remain unaltered. For films deposited at a low substrate temperature of 150°C, Raman spectroscopy reveals an improved ordering of the amorphous network on the short and medium range scale at increasing film thickness. At an enhanced substrate temperature of 270°C, the tendency of structural improvement is seen only on the medium range scale.

Collaboration: [1]Institute of Solid State Physics, Bulgarian Academy of Sciences, Sofia, Bulgaria; [2]Physics Department, National Technical University, Athens, Greece

S.Y. Chun[1]
A. Chayahara[2]
M. Posselt

Limitations on ultra-thin multilayers: pulsed cathodic arc and computer simulation

Nanoscale metallic multilayers were deposited by pulsed double-cathodic arc deposition and examined by XTEM. The individual layer thickness was varied from a few to tens of angstroms. TRIDYN computer simulations were performed for a better understanding of the nanoscale deposition process. For higher ion fluences (> $10^{16}cm^{-2}$) and larger bilayer thicknesses (> 2 nm), the periodicity of the multilayers is satisfactory. However, the results of the simulations for lower ion fluences and smaller bilayer thicknesses reveal that the individual layers are intermixed and diffused. The experimental results are in good agreement with the simulations. In the present case the lower limit of the bilayer period is approx. 2 nm.

Collaboration: [1]Department of Advanced Materials Science and Engineering, Mokpo National University, Jeonnam, South Korea; [2]National Institute of Advanced Industrial Science & Technology, Osaka, Japan

M. Beckers
N. Schell
R.M.S. Martins
W. Möller

Texture development during growth of $Ti_{1-X}Al_XN$ thin films studied by *in-situ* x-ray diffraction

To improve the understanding of the relationship between deposition parameters, microstructure, and performance of $Ti_{1-x}Al_xN$ thin films *in-situ* XRD studies *during* the film growth were performed using the deposition chamber installed at ROBL. All films were deposited by reactive co-sputtering from Ti and Al targets; one series at constant x = 0.06 varying substrate temperature, bias voltage, and nitrogen partial pressure and thus growth rate. In another series, x was systematically varied from 0 to 0.73 while keeping all other parameters constant. Values of x < 0.15 and high deposition rates lead to a typical cross-over behavior between initial (002) and final (111) preferred orientation. Reducing the deposition rate leads to (002) preferred orientation practically independent of film thickness and substrate temperature. Yet, suppressing collisionally-induced atomic N on the sample surface by applying a positive bias voltage, recovers a (111) preferred orientation. Keeping the deposition rates low, (111) preferred orientation can also be induced by increasing x above 0.15, which in the presence of atomic N can be explained by its higher adatom mobility. Increasing x towards the AlN segregation threshold at x = 0.60 leads to extremely hard nanocomposite TiAlN/AlN, and pushing x further to 0.73 leads to highly stressed AlN with an a-axis off-plane texture.

Supported by DFG

F. Allenstein[1]
A. Mogilatenko[1]
R. Grötzschel
G. Beddies[1]
H.-J. Hinneberg[1]

Influence of aluminium on the growth of nickel disilicide on Si(001)

For an improved lattice matching between Si and nickel silicide the influence of aluminum incorporation on the growth of nickel disilicide layers was investigated. Thin films of 10 to 20 nm thickness with different atomic ratios of Ni and Al were co-deposited by magnetron sputtering and then annealed at temperatures between 500 and 900°C using RTA in nitrogen atmosphere. RBS/channeling, SEM, TEM, XRD, AES and sheet resistance measurements were performed to characterize the deposited films. The forming temperature of thin epitaxial nickel disilicide layers decreases from 750°C without Al to lower than 500°C at an atomic ratio of Ni : Al = 9 : 1. The interface roughness also decreases rapidly with a higher amount of Al. Annealing of pure Ni layers creates pyramidal shaped nickel disilicide islands, whereas at an atomic ratio of Ni : Al = 4 : 1 nearly smooth epitaxial nickel disilicide layers are grown, featuring a low level of misfit dislocations as indicated by the low χ_{min} value of 0.04 in the channeling spectra.

Collaboration: [1]Institut für Physik, Technische Universität Chemnitz

R.A. Yankov
E. Richter

Efficient oxidation protection of γ-TiAl alloys by ion implantation of halogens

For the development of an efficient, commercially viable process for enhancing the high-temperature (> 700°C) oxidation resistance of γ-TiAl alloys, the plasma immersion ion implantation (PIII) route has been further developed. The ion fluence per pulse has been determined for Cl implantation. Metal contamination, which was found to be associated with the long low voltage tail of the pulse, was efficiently suppressed by pulse shaping using a specially designed ferrite coil. Experiments to explore the sensitivity of γ-TiAl to various implantation temperatures (RT to 800°C) have been conducted using standard beam line implantation (F^+, 60 keV, $1\times10^{17}\,cm^{-2}$). Optimized F implants produce markedly improved oxidation resistance even under harsh conditions of thermocyclic oxidation in a wet ambient. For implantation temperatures in the range of RT to 600°C, the degree of protection is sufficiently high and practically independent of temperature, but decreases dramatically at 800°C.

Collaboration: Karl-Winnacker Institut der DECHEMA e.V.

I. Tsyganov[1]
I. Kovalenko[1]
M.T. Pham
E. Richter

Structure and properties of boron implanted Ti-4Al-1.5Mn

The influence of beam-line high dose boron implantation on the mechanical properties and corrosion behavior of near-alpha titanium alloy Ti-4Al-1.5Mn was investigated. Boron was implanted into Ti-alloy at 60 keV with fluences ranging from $1\times10^{17}cm^{-2}$ to $5\times10^{18}cm^{-2}$. The implantation results in the Gaussian boron distributions with maximum concentrations ranging from ~10 to ~85 at.%. XRD shows that for B fluences $<5x10^{17}cm^{-2}$ (maximal B concentration ~50 at.%) only the TiB phase is formed, while by increasing the B fluence above $5\times10^{17}cm^{-2}$ the formation of TiB_2 is observed. The hardness of the implanted layer increases with increasing fluence. For the highest fluence the hardness is ~4.5 times higher than that of unimplanted Ti-4Al-1.5Mn. Corrosion potential at room temperature of the implanted surfaces in aerated 1 % NaCl solution is closer to the noble values in comparison to the unimplanted Ti-4Al-1.5Mn. In the passive corrosion region the B implanted surfaces are also more corrosion resistant. The improvement of the corrosion behavior is attributed to the implantation-induced formation of titanium borides.

Supported by DAAD
Collaboration: [1]Lipetsk State Technical University, Lipetsk, Russia

R.M.S. Martins
F.M.Braz Fernandes[1]
R.J.C. Silva[1]
M. Beckers
N. Schell

Structural *in-situ* studies of Shape Memory Alloy (SMA) Ni-Ti thin films

In-situ XRD experiments allow to improve the knowledge of the structural development (time dependent crystal reorientation, metastable phase formation, strain evolution) during Ni-Ti SMA thin film growth by magnetron co-sputtering (Ni-Ti + Ti) and its correlation with the deposition parameters. Films were deposited on naturally oxidized Si(100) substrates at a temperature of approx. 470°C. During film growth the B2 phase started by stacking onto (200) planes. The (110) stacking started after a stress relaxation of the B2(200). There is a significant decrease of the peak intensity ratio of B2(110)/B2(200) when a substrate bias (-45 V) is applied. Depending on the desired properties for functional devices, either B2 phase or additional Ni rich or Ti rich phases (precipitates) could be fabricated by varying the power of co-sputtering (Ni-Ti + Ti) for otherwise fixed deposition parameters.

Collaboration: [1]CENIMAT, Campus da FCT/UNL, Monte de Caparica, Portugal

A.S. Paula[1]
J.P.H.G. Canejo[1]
N. Schell
F.M.Braz Fernandes[1]

Structural evolution on thermal cycling in Ti-rich NiTi shape memory alloys (SMA)

Annealing of a Ti-rich Ni-Ti SMA has been followed by *in-situ* high temperature XRD at ROBL in order to register the texture as well as the microstrain/ microstress evolution. The knowledge of the preferential orientation is an important information, as the anisotropic response of the material contributes to the success of the envisaged SMA application. Using high-temperature pole figures measurement, we obtain a relation between the change of preferential orientation and the structural evolution taking place during annealing The most significant change of the microstrain and the coherency domain length of the sample takes place above 350ºC where recrystallization occurs. Annealing at temperatures higher than 600ºC gives rise to a significant decrease of the FWHM of the B2(110) peak (at 700ºC its FWHM reaches a value smaller than 0.05º). This grain growth step of the structural evolution is accompanied by a significant increase of the Ti_2Ni(511) peak, showing that a precipitation phenomenon has been induced. Two main components of austenite texture, {110}<110> and {111}<110>, i.e. α fiber II texture, were found during annealing up to 400ºC. At 500ºC {111}<110> became the dominant texture component.

Collaboration: [1]CENIMAT, Campus da FCT/UNL, Monte de Caparica, Portugal

Magnetic Films

J. Fassbender
J. McCord[1]
R. Mattheis[2]
K. Potzger
A. Mücklich
J. von Borany

Doping magnetic materials - tunable properties due to ion implantation

Doping of magnetic materials opens a route to a new class of artificial magnetic materials with adjustable magnetic properties. Here we have investigated the tailoring of the magnetic properties of Permalloy (20 nm $Ni_{81}Fe_{19}$) by means of 30 keV Cr implantation. Due to the doping the Curie temperature of the Permalloy film decreases with the implantation fluence and drops below room temperature at an averaged Cr concentration of about 7 at.%. Also the saturation magnetization and the uniaxial anisotropy decrease. However, the magnetic damping behavior is strongly enhanced which is due to a combination of structural changes and alloying effects. In order to clarify the basic mechanism for the enhancement, the chemical and structural contributions to the magnetic damping parameter are separated by a comparison to results of 30 keV Ni implantation.

Collaboration: [1]Leibniz Institut für Festkörper- und Werkstoffforschung Dresden; [2]Institut für Physikalische Hochtechnologie Jena

K. Potzger
L. Bischoff
M.O. Liedke
B. Hillebrands[1]
M. Rickart[2]
P. Freitas[2]
J. McCord[3]
J. Fassbender

Magnetic domain structure of micro-patterned PtMn/NiFe exchange bias bilayers

A bottom pinned exchange bias bilayer system consisting of 20 nm PtMn and 6 nm NiFe (produced using ion beam deposition (IBD) and physical vapour deposition (PVD, magnetron sputtering)) was laterally magnetically patterned by means of focused ion beam irradiation (FIB) on a micrometer scale. 25 keV ion irradiation with a fluence of $2\times10^{14}Ga^{+}/cm^{2}$ leads to a disordering of the as prepared chemically ordered PtMn-phase with only minor changes in sample topography. Thus the exchange bias field as well as the coercive field is reduced to a large extent on a local scale. The magnetic properties of FIB written 1 μm wide stripes and their interaction with the non-irradiated spacing were analyzed by means of MOKE, MFM, and Kerr microscopy. The application of a magnetic field between - 12 Oe and - 80 Oe with respect to the exchange bias field direction leads to an antiparallel alignment of irradiated and non-irradiated stripes forming pronounced domain walls. A parallel alignment was found below - 100 Oe and in the positive field region.

Supported by EU

Collaboration: [1]Fachbereich Physik, TU Kaiserslautern; [2]INESC MN, Lisbon, Portugal; [3]Leibniz Institut für Festkörper- und Werkstoffforschung Dresden

K. Potzger
H. Reuther
S. Zhou
A. Mücklich
F. Eichhorn
R. Grötzschel
J. Fassbender

Ion beam synthesis of Fe nanoparticles in MgO

MgO(001) single crystals were irradiated with ^{57}Fe at an energy of 100 keV and an ion fluence of $6\times10^{16}cm^{-2}$ at implantation temperatures between 25°C (RT) and 1000°C. Analysis was carried out by means of CEMS, XRD, RBS and TEM. We found that the implantation temperature plays the important role for the formation of Fe nanoparticles. The fraction of metallic Fe (CEMS Fe^{0} signal) increases from 28% for RT implantation to 60% for 800°C implantation, while the Fe profile remains unchanged ($R_p \approx 50$ nm). The nanoparticles formed after 800°C implantation are about 5 nm in size and exhibit fcc-structure with an orientation relationship of Fe(111)/MgO(111) and Fe(220)/MgO(220). The nanoparticles exhibit paramagnetism at room temperature. At an implantation temperature of 1000°C the Fe implantation profile smears out completely and 92% of the Fe atoms are found in the Fe^{3+} oxidation state.

K. Potzger
H. Reuther
S. Zhou

Doping of ZnO with Fe using ion implantation

ZnO(0001) single crystals have been implanted with ^{57}Fe at an energy of 180 keV and an ion fluence of $4\times10^{16}cm^{-2}$. Analysis was carried out by means of

J. Fassbender

CEMS. We found Fe present in the Fe^0 charge state with an amount of 12% showing ferromagnetic behavior at room temperature (B_{hf} = 30.5 T). The remaining Fe atoms are in Fe^{2+} (54%) and Fe^{3+} (33%) oxidation states. In agreement with recent channeling investigations *(E. Rita et al.; Appl. Phys. Lett.* ***85*** *(2004) 4899)* we conclude that these states (partially) represent substitutional Zn-lattice sites occupied by the Fe atoms.

M.O. Liedke
K. Potzger
B. Hillebrands[1]
M. Rickart[2]
P. Freitas[2]
J. Fassbender

Magnetic domain structure of micro-patterned PtMn/CoFe exchange bias bilayers

Using magnetron sputter deposition a number of high exchange bias field samples, consisting of glass/Ta 7 nm/PtMn 20 nm/t_{CoFe} = 2 – 6 nm/Ta 4 nm, were prepared for magnetic patterning investigations using optical lithography. Several patterns have been etched physically ranging from 1 μm^2 to 2500 μm^2, separated by lines of 2 μm to 10 μm width. The samples have been characterized by VSM and MOKE. All samples exhibit a well defined exchange bias field. A series of MFM images were taken from the structures. All images show a monodomain magnetization state in zero magnetic field. The shape of the structure itself dose not influence the stray field direction. The shape anisotropy contribution is thus smaller than the unidirectional anisotropy given by the exchange bias.

Supported by EU

Collaboration: [1]Fachbereich Physik, TU Kaiserslautern; [2]INESC MN, Lisbon, Portugal

J. McCord[1]
J. Fassbender
M. Frommberger[2]
M.O. Liedke
E. Quandt[2]
L. Schultz[1]

Anisotropy patterning of amorphous CoFeSiB films by He ion irradiation

The local alteration of the magnetic anisotropy axis in amorphous soft magnetic FeCoBSi films by He-ion irradiation in an applied magnetic in-plane field has been investigated. Sputtered CoFeSiB (thickness 30 nm) were irradiated with 5 keV He-ions. A magnetic field of 600 Oe was applied during irradiation aligned orthogonal to the initial easy axis of anisotropy. Above a critical fluence an alignment of anisotropy in the applied field direction is observed by MOKE and complementary domain observation by Kerr microscopy. Using irradiation together with photolithography the films were irradiated locally, thus resulting in anisotropy-patterned structures. Domain patterns in different elements with varying angles of anisotropy and edge orientation, separating regions of different anisotropy alignment, are shown. The influence of the patterning on the (still) full film reversal is determined in detail.

Collaboration: [1]Leibniz Institut für Festkörper- und Werkstoffforschung Dresden; [2]Stiftung “Center of Advances European Studies and Research” (Caesar), Smart Materials Laboratory, Bonn, Germany

M.C. Weber[1]
H. Nembach[1]
B. Hillebrands[1]
J. Fassbender

Small and large angle precession in exchange biased bilayers

Small and large angle excitations in exchange bias systems have been investigated in real time by means of all-optical pump-probe experiments. Due to an increased spin temperature upon photoexcitation, an unpinning of the interfacial exchange coupling takes place resulting in a collapse of the unidirectional anisotropy. In terms of an internal pulse field the excess energy of the spin system leads to the excitation of a high frequency precessional response. The magnitude of the internal pulse field can be controlled by the absorbed photons. Hence, the precessional motion depending on the precession angle can be investigated. The extracted Gilbert parameter does not depend on the magnitude of the internal pulse field. Both small and large angle precession can be modeled within the Landau-Lifshitz-Gilbert framework. Employing the antiferromagnetic thickness dependence of the exchange bias field, the exchange bias field dependence of the Gilbert parameter was investigated. The dissipation rate increases linearly with the exchange bias field magnitude

which can be understood taking local fluctuations of the interfacial exchange coupling as an additional dissipation mechanism into account.

Supported by DFG
Collaboration: [1]Fachbereich Physik, TU Kaiserslautern, Germany

M.C. Weber[1]
H. Nembach[1]
H. Schultheiss[1]
C. Bayer[1]
S. Blomeier[1]
R. Kaltofen[2]
J. Schumann[2]
M.J. Carey[3]
B. Hillebrands[1]
J. Fassbender

All-optical probe of magnetization dynamics in exchange bias systems

The picosecond optical control of the exchange bias anisotropy was investigated in real time for different exchange bias bilayers (NiFe/FeMn, CoFe/NiMn, CoFe/IrMn) using time-resolved magneto-optics. Upon photoexcitation the spin temperature is increased leading to a collapse of the interfacial exchange coupling. Both the shift fields and the easy axis coercivities are reduced within the first 10 ps. The unpinning is followed by a slower spin-lattice relaxation process. The deduced relaxation times turn out to be quite comparable (< 205 ps) for all bilayers. The thermal decoupling of the bilayers can lead to a high frequency precession of the magnetization of the ferromagnetic layers. The precessional response of the CoFe/IrMn system reveals a Kittel type field dependence of the precession frequency. Brillouin light scattering measurements of the field dependence of the FMR frequency are in good agreement with the real time measurements, further supporting the homogeneous mode character of the optically excited precession.

Supported by DFG
Collaboration: [1]Fachbereich Physik, TU Kaiserslautern; [2]Leibniz Institut für Festkörper- und Werkstoffforschung Dresden; [3]Hitachi Global Storage Technologies, San Jose Research Center, USA

K.-H. Heinig
B. Schmidt
L. Röntzsch
F. Eichhorn
J. Schumann[1]

$L2_1$ ordering in Heusler alloys by He^+ irradiation

Layers of sputter-deposited $Co_2Cr_{0.6}Fe_{0.4}Al$ Heusler alloys (50 – 100 nm thick) were irradiated with 0.2 µA/cm^2 of 40 keV He^+ ions up to fluences between 10^{15} and 10^{16}cm^{-2}. The sample temperature during He^+ irradiation was fixed at 600, 700 or 800°C. Preliminary studies of 50 nm thick $Co_2Cr_{0.6}Fe_{0.4}Al$ layers irradiated at 600°C with 10^{15} He^+/cm^2 resulted in a coercivity of H_c = 182 Oe and a saturation magnetization of m_s = 216 µemu. Without ion irradiation, as-deposited layers and layers annealed at high temperatures lead to typically H_c = 0.5 Oe and m_s = 121 µemu. Thus, He^+ irradiation of this Heusler alloy improves its magnetic properties substantially. It has been proven by XRD studies that the improved magnetic properties are caused by ion-assisted B2 $\rightarrow$ $L2_1$ superstructure formation in the $Co_2Cr_{0.6}Fe_{0.4}Al$ Heusler alloy. The (200) superlattice peak of the Co sublattice has been found in XRD studies after irradiation at 600°C, whereas the (111) superlattice peak indicating Cr and Al ordering has been detected after irradiation at 800°C only. Obviously, although He^+ irradiation assists ordering substantially, a complete $L2_1$ phase formation has not been achieved yet.

Collaboration: [1] Leibniz Institut für Festkörper- und Werkstoffforschung Dresden

V. Cantelli
J. von Borany
J. Fassbender
R. Kaltofen[1]

$L1_0$ ordering in He-irradiated NiMn films

Magnetron sputtered film stacks of 5 nm Ta/20 nm $Fe_{20}Ni_{80}$/50(15) nm NiMn/ 5 nm Ta deposited at Si/SiO_2 substrates were subsequently irradiated with He ions (30 keV, $1\times10^{15} \div 3\times10^{16}$cm^{-2}, RT or 250°C). The transition from the chemically disordered, paramagnetic NiMn phase (fcc) to the ordered, antiferromagnetic $L1_0$ phase (fct) during annealing (100 – 500°C, Vac) was studied by *in-situ* XRD at ROBL. A small $L1_0$ fraction (< 10%) is already available after deposition. The transformation to a dominating $L1_0$ ordered NiMn film takes place at about 300°C for both, implanted and unimplanted samples. Implantation at 250°C lowers the transition temperature only at about 50°C. Thus, the transition temperature is much more influenced by the thermal budget than the ion irradiation. This is explained by the high mobility of Mn and Ni which probably leads to a fast recombination of irradiation induced point defects. Annealing at higher temperatures (T > 400°C) leads to a loss of

$L1_0$ ordering due to an intermixing of the NiMn and the Permalloy ($Fe_{20}Ni_{80}$) films, resulting in an FeNiMn-alloy with a lattice constant according to Vegard's rule. A benefit of ion irradiation is the improvement of the crystallinity and the degree of <111> texture in the NiMn films already after low fluence ($1\times10^{15}cm^{-2}$) implantation.

Collaboration: [1]Leibniz Institut für Festkörper- und Werkstoffforschung Dresden

Biotechnological Materials

I. Tsyganov[1]
M.F. Maitz
E. Wieser
E. Richter
H. Reuther

Correlation between blood compatibility and physical surface properties of titanium-based coatings

Layers of Ti nitride, Ti oxynitrides TiN_xO_y and Ti oxide were produced by means of metal plasma immersion ion implantation and deposition (MePIIID) from a plasma produced by cathodic arc evaporation of Ti under addition of nitrogen and/or oxygen to the ambient near the substrate. The phase composition and structure of the layers are strongly dependent on the relation of the gas partial pressure. To study the correlation between blood compatibility and physical properties of the coatings, the thrombocyte adhesion and fibrinogen adsorption on the surface as well as wettability and surface energy were investigated. The blood compatibility of Ti oxide in part of the thrombocyte adhesion and fibrinogen adsorption can be improved by the addition of N into the layer. Thrombocyte adhesion and fibrinogen adsorption are lower for TiN_xO_y than for TiO_2. This correlates with a lower hydrophobicity and higher polar component of the surface energy for TiN_xO_y.

Collaboration: [1]Lipetsk State Technical University, Lipetsk, Russia

S. Matys[1]
M.F. Maitz
W. Pompe[1]

Detection of copper(II) and nickel(II) uptake by Bacillus sphaericus and Pseudomonas stutzeri

Two membrane permeable fluorescence dyes, the calcium indicator Oregon Green (OG) and the nickel sensitive dye Newport Green (NG) were used in membrane permeable forms for detection of the uptake of copper and nickel ions in common soil bacteria. NG fluorescence directly and highly specific reflects the uptake of nickel into the cells by enhancement of the fluorescence. OG as marker for intracellular calcium forms a fluorescent complex inside the cells, which is subsequently quenched by the competing copper ions in dependence on their concentration. Flow cytometry revealed a higher Cu^{2+} uptake by the gram negative *P. stutzeri* DSMZ 5190 than by gram positive *B. sphaericus* JG-A12 and NCTC 9602. For *B. sphaericus* JG-A12 a more effective Ca^{2+} dependent defence mechanism against Ni^{2+} was found than in NCTC 9602. This shows that the combination of flow cytometry with appropriate metal specific fluorescence dyes generally enables a fast and efficient look into single vital bacterial cells in presence of heavy metals while simultaneous monitoring of their physiological state.

Collaboration: [1]Institut für Werkstoffwissenschaft, Technische Universität Dresden

S. Tunc[1]
M.F. Maitz
G. Steiner[2]
L. Vázquez[3]
M.T. Pham
R. Salzer[2]

***In-situ* conformational analysis of fibrinogen adsorbed on Si surfaces**

Structural changes of fibrinogen were characterized in its adsorbed state. Specific enzyme linked immunosorption experiments show that the amount of adsorbed fibrinogen increases as the surface becomes more hydrophobic. AFM investigations reveal the trinodular shape of fibrinogen molecules adsorbed on hydrophilic surfaces, whereas all of the molecules appear globular on hydrophobic surfaces. The distribution of secondary structures in adsorbed fibrinogen was quantified by *in-situ* FTIR analysis. Substrates of identical chemical bulk composition but different surface hydrophobicity permit direct comparison among them. Adsorption properties of fibrinogen are different for each degree of hydrophobicity. Although there is some increase of turn structure and decrease of β-sheet structure, the secondary structure of adsorbed fibrinogen on hydrophilic surface turns out to be rather similar to that of the protein in solution phase with a major α-helix content. Hydrophilic surfaces exhibit superior blood compatibility as required for medical applications.

Collaboration: [1]University Antalya, Turkey; [2]Institut für Analytische Chemie, TU Dresden; [3]Ciencia de Materiales de Madrid (CSIC), Cantoblanco, Madrid, Spain

A.V. Kondyurin
M.F. Maitz

Ion implantation of ePTFE for increased wettability and improved cell adherence

Mechanically stretched, expanded polytetrafluorethylene (ePTFE) is a microscopically porous version of PTFE, possessing excellent chemical- and biostability. The application of ePTFE as blood vessel prostheses in vascular surgery is nowadays common, however problems such as thrombosis still occur in small diameter vessels. Attachment of endothelial cells as a vessel lining has been proposed as a method to reduce the event of thrombosis. However, due to the highly hydrophobic nature of the material, sufficient cell attachment cannot currently be realised. PIII has been used to modify the surface of PTFE, ePTFE and LDPE by 0.5 – 20 kV implantation of nitrogen, argon and oxygen ions, with doses varying from 10^{13} to $10^{16}cm^{-2}$. Hydrophobicity, measured by water contact angle, was reduced for PTFE and LDPE for low to medium doses (10^{13} – $10^{15}cm^{-2}$) but increased again with high doses due to carbonisation and roughening of the surface. FTIR revealed the low to medium dose modifications as being due to increased oxygen containing chemical groups on the surface. Increase in the adhesion and survival of endothelial cells was observed on PIII treated ePTFE, with the high dose samples ($10^{16}cm^{-2}$) showing the most improvement. Chemical cross-linking of hydrophilic molecules like acrylamide to the newly formed reactive groups of the surface further improved the cell performance.

Collaboration: Boston Scientific SCIMED, USA

Nanostructures

B. Schmidt
K.-H. Heinig
L. Röntzsch
T. Müller
K.-H. Stegemann[1]
E. Votintseva[1]
T. Gemming[2]
J. Thomas[2]
M. Klimenkov[3]

Ion irradiation through SiO_2/Si-interfaces: Non-conventional fabrication of Si nanocrystals for memory applications

Si nanocrystals for multi-dot floating-gate memories have been produced by non-conventional ion beam synthesis. The stack (50 nm poly-Si)/(15 nm SiO_2) /(Si substrate) of MOSFETs has been exposed to 50 – 100 keV Si^+ irradiation, the Si^+ ions comes to rest below the gate oxide within the (001)Si substrate. Thus, Si excess in the gate oxide of the MOS structure is formed mainly by ion beam mixing of the upper poly-Si/SiO_2 interface and the lower SiO_2/(001)Si interface. Subsequently, the metastable SiO_x of the two ion beam mixed interfaces has been transformed into stable Si and SiO_2 by rapid thermal annealing (RTA). Adjacent to the recovering interface, narrow SiO_2 zones become denuded of excess Si, whereas the more distant tails of excess Si form nanocrystals in the gate oxide. Using energy filtered TEM (EFTEM) Si nanocrystals with diameter of ≤ 2 nm located in two NC-δ-layers near the poly-Si/SiO_2 and the SiO_2/Si-substrate interfaces have been observed. The EFTEM images of these two NC-δ-layers coincide very well with results of kinetic Monte Carlo simulations of phase separation in non-stoichiometric phases near ion beam mixed Si/SiO_2 interfaces.

Supported by EU GROWTH Program

Collaboration: [1]ZMD AG Dresden; [2]Leibniz Institut für Festkörper- und Werkstoff-forschung Dresden; [3]Forschungszentrum Karlsruhe

P. Dimitrakis[1]
P. Normand[1]
E. Vontitseva[2]
K.H. Stegemann[2]
K.-H. Heinig
B. Schmidt

Memory devices obtained by Si^+ irradiation through poly-Si/SiO_2 gate stack

Ion irradiation induced interface mixing was used to generate silicon nano-clusters at the SiO_2-Si interface of MOS structures aiming at electronic memory applications. No particular processing issues have been encountered during integration of this technique in standard submicron CMOS technology. The memory properties of the fabricated structures as a function of the Si^+-irradiation dose and post-irradiation temperature and time have been examined through electrical measurements of capacitors and transistors. Low-voltage operating devices that can endure more than 10^6 programming/erasing cycles have been successfully achieved. While excellent device uniformity and reproducibility have been observed over 6-inch wafers, more research is still required to improve charge retention and ensure the standard 10-year retention time needed for true non-volatile memory applications.

Supported by EU GROWTH Program

Collaboration: [1]National Center for Scientific Research “DEMOKRITOS” Athens, Greece; [2]ZMD AG Dresden

V. Cantelli
J. von Borany
R. Grötzschel
A. Mücklich
N. Schell

Comparison of ion beam synthesis of Ge and Co nanoparticles in a SiO_2 matrix

Ge or Co nanoclusters (NC) in 1 μm thermally grown SiO_2 films have been fabricated by ion beam synthesis. A four-fold sequence of $^{74}Ge^+$ or $^{59}Co^+$ (E = 45 – 350 keV, total fluence $7.8\times10^{16}cm^{-2}$) implantation was used to create box-like Ge or Co profiles ($C_{Max} = 3 \pm 1$ at.%) down to a depth of about 300 nm. Different annealing steps ($T_A = 600 \div 1100$°C) in dry Ar atmosphere or vacuum were carried out. The NC evolution was characterized by RBS, TEM and *in-situ* grazing incident XRD ($\alpha_I = 0{,}5°$; $\lambda = 1{,}54$ Å) at ROBL. Remarkable differences were found between the Ge and Co NC evolution. For Ge implanted SiO_2 films, a significant near-surface Ge oxidation and Ge nanocluster melting at temperatures above 850°C was established. The mean NC size continuously increases with T_A from approx. 2 nm (T_A = 800°C, 30 s) to ~ 5 nm (T_A = 1000°C, 30 min). On the contrary, for Co-implanted SiO_2 films, a jump-like transition in the nanocluster properties are observed at $T_A \approx 800$°C:

A homogenous distribution of small (diameter ~ 4 nm) amorphous clusters is transformed into a bimodal NC distribution consisting of large (diameter between 20 and 40 nm) nanocrystals near the surface (< 100 nm) and a deeper region of smaller NC (diameter ~ 7 nm). Moreover, the existence of a large number of tiny amorphous clusters surrounding the large ones was observed by HRTEM. In contrast to Ge, within the investigated temperatures range Co NC do not melt.

J. Meijer[1]
B. Burchard[1]
I. Rangelow[2]
L. Bischoff

Nano-aperture for single ion implantation with nm lateral resolution

The fabrication of nanoscale quantum devices for solid state information technology requires tools to manipulate or implant single atoms, clusters or molecules with nm resolution or below. The technical requirements to meet this challenge are enormous. We propose a new technology, which allows one to implant countable singly charged ions with very high recognition. The basic idea is to use an ion trap as ion source and a nano-machined AFM- tip combined with a micro lens as a focussing system. For the tip processing the IMSA-Orsay Physics FIB equipped with a Ga LMIS and a spot size of 30 nm was used. A special end-point detector was implemented to stop the sputtering process immediately after the penetration of the ions. Thus on top of an Au covered pyramidal cantilever tip a nano-hole with an inlet diameter of 140 nm and a diameter smaller than 50 nm on the back side, studied by high-resolution SEM, was fabricated. Ion optical calculations of the experimental setup consisting of a trap source combined with nanometric components were performed. Additionally adaptations and limits of this method to focus nanocluster beams, molecules and high energetic ions were investigated.

Collaboration: [1]Institut für Physik mit Ionenstrahlen, Ruhr-Universität Bochum; [2]Institut für Mikrostrukturtechnologie und Analytik, Universität Kassel

Ch. Akhmadaliev
L. Bischoff
B. Schmidt
L. Röntzsch

$CoSi_2$ – nanowires fabricated by FIB

Nanostructures, like wires or pearl chains play an increasing role in areas as plasmonics, nano-optics or nanoelectronics as well as in the implementation of optical components into microelectronic devices. $CoSi_2$ is a promising materials candidate due to its metallic behaviour with low resistivity and the compatibility with the microelectronics technology. Two methods to fabricate $CoSi_2$ nanowires using FIB technique in terms of ion beam synthesis (IBS) are investigated. In a first approach an oxide layer, structured by use of a fine focused Ga beam, acting as an implantation mask for a broad beam Co doping at elevated temperatures (420°C) and subsequent annealing (600°C, 60 min + 1000°C, 30 min in N_2) was investigated. Nanowires as narrow as 20 nm aligned to the <110> crystal orientation but not continuous over the whole mask structure could be obtained. Secondly, a mass separated FIB of cobalt ions is applied for a direct writing IBS process. To this end a $Co_{36}Nd_{64}$ alloy LMIS was introduced in the FIB column (Canion 31Mplus, Orsay Physics). The use of the doubly charged ions allows one to increase the energy up to 60 keV, important to obtain buried structures. The results were comparable to that of the broad-beam implantation. The extreme high dose rate in the FIB spot smaller than 50 nm needs a further investigation of the time scale of the process due to dynamic annealing and damage accumulation.

Supported by DFG

L. Bischoff
B. Schmidt
C. Akhmadaliev
J. Renger[1]
J. Seidel[1]
P. Olk[1]

Focussing of surface plasmon polaritons by triangle-shaped waveguides

Different approaches to concentrate the electromagnetic field at optical frequencies by means of surface-plasmon-polaritons (SPP) have been explored aiming at strong enhancement and localization of the field. Thin-film metallic waveguides of triangular shape were employed to concentrate the light into a sub-wavelength region at the apex of the triangle. The metallic Al and Ag thin

S. Grafström[1]
L. M. Eng[1]

films deposited onto a glass substrate were structured photolithographically at the micron scale. Later on the focussed ion beam was used to introduce the sub-micron features like sharp edges or grooves into the waveguide with a nanometer precision. The SPP is excited by focussing the light onto a small groove intersecting the metallic waveguide. The groove cancels the requirement of momentum conservation and makes the excitation of surface waves possible. The SPP propagates along the waveguide towards the very end. This metallic waveguide structures are advantageous because of the absence of cut-off frequency known from the dielectric (glass) waveguides opening the door to sub-wavelength resolution in microscopy.

Collaboration: [1]Institute for Applied Physics, University of Technology Dresden

L. Röntzsch
K.-H. Heinig

Atomistic computer simulations on ion beam synthesis and stability of nanowires

First results were obtained on the ion beam synthesis of single-crystalline nanowires embedded in a single-crystalline matrix, particularly of $CoSi_2$ nanowires in Si(100). The line implantation profile of a scanning focused Co ion beam of a few tens of nanometers in width was calculated on the basis of final ion range data taken from TRIDYN and TRIM simulations. The 3D implantation profile served as input for a kinetic lattice Monte-Carlo code by means of which nucleation and growth of $CoSi_2$ precipitates (A-type) and their coalescence into a $CoSi_2$ nanowire were described. After nanowire synthesis, the system has a further tendency towards a reduction of interfacial free energy (“Rayleigh instability”). It was demonstrated that the orientation of an embedded nanowire to the host matrix strongly influences its stability. Since the system energetically favors the $CoSi_2$(111)/Si(111) interface, stabilizing forces occur if the nanowire is aligned with the <011> directions of the matrix. On the contrary, misaligned nanowires were found to be subject to strong faceting forces which lead to their decay into a chain of rather monodisperse and equidistant nanoclusters, whose size and separation distance depend on the angle of misalignment.

Supported by DFG

K.-H. Heinig
A. Polman[1]
A.M. Vredenberg[2]
M. Toulemonde[3]
T. van Dillen[4]

Mechanism of ion beam shaping of nanometals

Extreme shaping of Au nanospheres in SiO_2 into Au nanorods and Au nanowires using swift heavy ion irradiation has been reported recently (IBMM 04). Aspect ratios exceeding 20 were achieved with 54 MeV Ag^+ ions at rather low fluences (several $10^{14}cm^{-2}$). The mechanism for this behavior is not clear yet, in particular this cannot be explained by the so-called “Trinkaus model”, which describes the ion-assisted anisotropic deformation of nanoparticles. A first consistent model which describes both, nanometal shaping and accumulation of several nanoparticles into one nanowire, has been developed. Kinetic Monte Carlo simulations using temperature-time-profiles of ion tracks suggest that ion beam shaping is driven by temperature-dependent surface tension of partially molten Au particles (Marangoni effect), and that diffusive Au mass transfer through SiO_2 from short to long wires occurs via a mechanism similar to Ostwald ripening.

Collaboration: [1]Center of Nanophotonics, FOM-Institute AMOLF, Amsterdam, Netherlands; [2]Utrecht University, Netherlands; [3]CIRIL, Caen, France; [4]Groningen University, Netherlands

A. Peeva[1]
M. Kalitzova[1]
G. Zollo[2]
G. Beshkov[1]
G.Vitali[2]
W. Skorupa

Ion beam assisted Ge nanocrystallization in Ta_2O_5 films

The influence of Ge^+ ion fluence and post-implantation thermal treatment on the Ge nanocrystallization in Ta_2O_5 films was investigated. RF sputtered amorphous Ta_2O_5 films on Si were implanted with Ge^+ ions at 40 keV to fluences of $5\times10^{15} - 5\times10^{16}cm^{-2}$ at room temperature. The nanocrystallization of the implanted Ge was initiated by rapid thermal annealing at temperatures

between 700 and 1000°C for 30 s. In order to compare the microstructure of the as-implanted and the annealed Ta_2O_5 films, TEM studies were carried out in diffraction contrast and phase contrast (high resolution) modes. The TEM observations show that Ge tends to agglomerate and form nanoclusters for the fluence $5\times10^{16}cm^{-2}$. Thermal treatment at 700°C is optimal for the purpose of the present study. At this temperature Ge forms nanoclusters while the Ta_2O_5 film remains amorphous. At higher annealing temperatures crystallization processes in the Ta_2O_5 layer take place.

Collaboration: [1]Institute of Solid State Physics, Sofia, Bulgaria; [2]University "La Sapienza", Rome, Italy

Doping and Defects in Semiconductors

F. Gao[1]
W.J. Weber[1]
M. Posselt
V. Belko[2]

Atomistic study of intrinsic defect migration in 3C-SiC

Atomic-scale computer simulations, both molecular dynamics (MD) and the nudged-elastic band methods, have been applied to investigate long-range migration of point defects in cubic SiC (3C-SiC) over the temperature range from $0.36T_m$ to $0.95T_m$ (melting temperature). The point defect diffusivities, activation energies, and defect correlation factors have been obtained. Stable C split interstitials can migrate via the first- or second-nearest-neighbor sites, but the relative probability for the latter mechanism is very low. Si interstitials migrate directly from one tetrahedral position to another neighboring equivalent position by a kick-in/kick-out process via a split-interstitial configuration. Both C and Si vacancies jump to one of their equivalent sites through a direct migration mechanism. The migration barriers obtained for C and Si interstitials are consistent with the activation energies observed experimentally for two distinct recovery stages in irradiated SiC. Also, energy barriers for C interstitial and vacancy diffusion are in reasonable agreement with ab initio data.

Collaboration: [1]Pacific Northwest National Laboratory, Richland, USA; [2]Belarus State University, Minsk, Belarus

Z. Zolnai[1]
A. Ster[1]
N. Q. Khánh[1]
E. Kótai[2]
M. Posselt
G. Battistig[1]
T. Lohner[1]
J. Gyulai[1]

Ion beam analysis and computer simulation of damage accumulation in nitrogen implanted 6H-SiC: effects of channeling

500 keV nitrogen implantations at different tilt angles (0°, 0.5°, 1.2°, 1.6°, 4°) with respect to the c-axis of 6H-SiC were carried out. Radiation damage distributions have been investigated by RBS/C using 3.55 MeV $^{4}He^{+}$ beam. A comparative simultaneous evaluation of the damage depth distributions in the Si and C sublattices of 6H-SiC led to a <0001>-channeling-to-random correct-ion factor of 0.8 in the electronic stopping power of the $^{4}He^{+}$ ions. Full-cascade Crystal-TRIM simulations could reconstruct the measured shapes and heights of damage distributions for all implantation tilt angles. Secondary defect generation effects in addition to the primary point defect accumulation were assumed in the analysis.

Collaboration: [1]Research Institute for Technical Physics and Materials Science, Budapest, Hungary; [2]Research Institute for Particle and Nuclear Physics, Budapest, Hungary

A. Lebedev

Development and maintenance of the Crystal-TRIM module of the process simulator FLOOPS-SYN

The state-of-the-art process simulator FLOOPS-SYN includes Crystal-TRIM as its primary Monte-Carlo implantation engine. Crystal-TRIM capabilities have been extended to simulate ion implantation into crystalline targets with variable material composition, such as Si_xGe_{1-x}. The lattice constant of the target material can be treated as a numerical field, which enables modeling of e.g. strained-silicon structures. Numerous enhancements have been made both to the core BCA code and to overlaying algorithms (lateral trajectories replication, treatment of extended target boundaries, etc.) to stabilize and significantly accelerate the simulation process for modern complex 2D and 3D device structures.

Supported by ISE

Collaboration: Integrated Systems Engineering (ISE) AG / Synopsys, Zürich, Switzerland

W. Skorupa
G. Ferro[1]
D. Panknin
W. Anwand

Improved FLASiC method for high-quality SiC-on-Si heteroepitaxy

Very thin 3C-SiC films epitaxially grown on Si-substrate are substantially improved after irradiation with flash lamp pulses of 20ms duration. In this so called FLASiC process, the irradiated energy is selectively absorbed at the

J. Stoemenos[2]
The FLASiC Consortium

SiC/Si interface where the most defective part of the 3C-SiC film exists. The Si at the interface melts up to a depth depending on the energy density of the flash pulse. Thus the lower part of the SiC film is dissolved into the melted Si substrate, then during the solidification phase separation occurs and the SiC is recrystallized forming high quality 3C-SiC trapezoidal pyramids (TPs) on the backside of the non-dissolved SiC film. However due to significant Si mass transport the Si-surface is seriously undulated. Also the SiC film is mainly improved from the backside leading to defective epitaxial growth. Therefore an improved method was developed aiming (i) to minimize the undulations of the Si substrate, and (ii) to improve the quality of the SiC film at the front interface. This patented method involves the deposition of a silicon overlayer (SOL) onto the SiC, followed by an additional SiC layer on the SOL. The new method is called i-FLASiC where the “i” stands for “inverse”.

Supported by EU
Collaboration: [1]University C. Bernard, Lyon, France; [2]Aristotele University, Thessaloniki, Greece

M. Voelskow
W. Skorupa
G. Ferro[1]
J. Stoemenos[2]

Homogenisation of the melting depth in FLASiC structures

FLASiC processing leads to the well known faceted melting of the monocrystalline bulk silicon surface due to the substantial overheating of the substrate. Therefore the recrystallization process starts from a non planar liquid-solid interface leading due to the different densities of liquid and solid silicon to a non-flat SiC-Si interface. During further epitaxial growth this results in a too defective epilayer quality. To overcome this problem, a carbon rich (~5 %) but crystalline region was positioned by high temperature ion implantation about 500 nm behind the SiC-Si interface into the silicon substrate. Regarding to the phase diagram, this carbon concentration leads to an increase of the melting temperature of silicon of more than hundred degrees. Hence, only a thin uniformly molten silicon layer, located between the top SiC layer and the carbon rich so called melt stop layer, is formed during the flash lamp irradiation. After the flash pulse the Si layer recrystallizes epitaxially on the implanted crystalline layer resulting in a well annealed planar SiC layer.

Supported by EU
Collaboration:[1]University C. Bernard, Lyon, France; [2]Aristotele University, Thessaloniki, Greece

D. Panknin
P. Godignon[1]
J. Stoemenos[2]
G. Ferro[3]
W. Skorupa

Formation of 3C-SiC films embedded in SiO_2 by sacrificial oxidation

The formation of high-quality thin 3C-SiC layers on SiO_2 is described using the sacrificial oxidation as a tool. The wet oxidation in 3C-SiC is very anisotropic and strongly dependent on the defect density. At first a 35 nm thick 3C-SiC film was deposited on the Si substrate, then the film was treated by flash lamp irradiation. After that two zones can be distinguished, the upper, which exhibits a high defect density, and the lower with a significantly reduced defect density. The upper zone was wet oxidized and an oxide layer was formed on top of the good-quality 3C-SiC film. In parallel, a buried oxide layer was formed by oxidation of the Si substrate through small channels, which were formed in the SiC during the wet oxidation. Through those channels the Si substrate is oxidized fast forming a continuous buried oxide layer and realizing in this manner a 3C-SiC-On-Insulator structure.

Supported by EU
Collaboration: [1]CNM Barcelona, Spain; [2]Aristotele University, Thessaloniki, Greece; [3]University C. Bernard, Lyon, France

M. Voelskow
D. Panknin
J. Stoemenos[1]
G. Ferro[2]
P. Godignion[3]
W. Skorupa

Epitaxial 3C-SiC formation at the SiO_2/Si interface by C^+ implantation into SiO_2 and annealing

The applicability of the formation of high quality 3C-SiC carbonized layers on Si substrates as seeds for further epitaxial deposition of thick 3C-SiC films was studied. Due to the 20% misfit between Si and 3C-SiC as well as the fast carbonization process the defect density of the carbonized layers is very high,

of the order of 5×10^{11} to $10^{12}cm^{-2}$. The purpose of this work was to replace the conventional carbonization process by a method working more slowly and closely to thermal equilibrium. In this case carbon is introduced by ion implantation into the thermally grown oxide on a Si substrate near to the SiO_2/Si interface, which is then transferred to the Si surface by annealing. This results in the formation of small SiC grains at the SiO_2/Si interface perfectly aligned with the Si matrix and absolutely flat at the SiO_2/Si interface. Another advantage of the new carbonization process is the elimination of the cavities due to the suppression of Si out-diffusion.

Supported by EU

Collaboration: [1]Aristotele University, Thessaloniki, Greece; [2]University C. Bernard, Lyon, France, [3]CNM Barcelona, Spain

R. Kögler
F. Eichhorn
A. Mücklich
T. Schumann
C. Serre[1]
A. Perez-Rodriguez[1]
W. Skorupa

Effect of in-situ point defect composition on ion beam synthesis of SiC

SiC nanoclusters (nc) were synthesized by C ion implantation in Si at a temperature of 480°C. The quantity and quality of SiC nc were compared for different implantation modes: simultaneous and sequential. The simultaneous implantation mode was performed by two ion beams, C^+ and Si^+ ions. The additional Si implant is associated with excess vacancy generation in the SiC formation zone. In this way the composition of point defects, vacancies versus interstitials, was varied. The effect of vacancies on the SiC synthesis was studied. The sequential pre-deposition of vacancy defects in the Si substrate before the C implantation was performed by an additional Si or He implantation. The simultaneous dual beam implantation was found to be the only method to improve SiC synthesis. The generation of vacancies, both excess vacancies and He induced vacancies, using a sequential implantation process is disadvantageous for SiC nc formation. The pre-deposition of vacancy defects is accompanied by a higher crystal damage and/or the defects are annealed out during the subsequent C implantation at temperatures above 400°C. Vacancies must be created "in-situ" during C implantation to achieve enhanced output of SiC.

Collaboration: [1]University of Barcelona, Spain

G. Brauer
W. Anwand
P.G. Coleman[1]
W. Skorupa

Vacancy-type damage in 6H-SiC after Al^+ and N^+ co-implantation and annealing

Vacancy-type damage formed in n-type 6H-SiC from CREE Inc. (USA) co-implanted by Al^+ and N^+ at 800°C, and subsequently annealed at 1200°C and 1650°C, was studied as a function of the sequence of implantations and annealing conditions. Parameters of the fourfold implantation were chosen to produce buried layers of $(SiC)_{1-x}(AlN)_x$ with x ~ 0.2. The basic defect formed is found to be the nearest-neighbor Si + C divacancy (V_2) and multiples of it. As a general feature, large-sized defects (25 – 30 V_2) are observed after the four implantation steps in a very narrow sub-surface layer only, whereas deep-reaching defects of three to four agglomerated V_2 are still found to exist far beyond the implanted layer in the material. It is certain now that the depth profile of vacancy-type damage strongly depends on the sequence of implantations and on annealing conditions. These studies show that annealing even at 1650°C for 10 min is not sufficient to remove the vacancy-type damage created by ion implantation.

Collaboration: [1]Department of Physics, University of Bath, UK

W. Skorupa
R.A. Yankov[1]
W. Anwand
M. Voelskow
T. Gebel[1]
D.F. Downey[2]

Ultra-shallow junctions produced by BF_3 plasma doping and flash lamp annealing

The capabilities of plasma doping (PLAD) and flash lamp annealing (FLA) for use in ultra-shallow junction fabrication were evaluated. Silicon wafers were doped in a BF_3 plasma using wafer biases ranging from 0.6 to 1 kV and a dose of $4\times10^{15}cm^{-2}$. The wafers so implanted were heat-treated by FLA using

E.A. Arevalo[2]

preheating temperatures in the range of 500 to 700°C, peak temperatures of 1100 to 1350°C, and effective anneal times of 20 and 3 ms. SIMS and sheet resistance measurements were undertaken to determine the junction depth and the sheet resistance, respectively. Optimum processing conditions have been identified under which both high electrical activation and insignificant dopant diffusion occur compared to the as-implanted state. In this way, one can obtain combinations of junction depth and sheet resistance that meet the 45 nm (!) technology node requirements according to the International Technology Roadmap for Semiconductors 2002.

Supported by EU and VSEA

Collaboration: [1]nanoparc GmbH, Dresden; [2]Varian Semiconductor Equipment Association, Gloucester, MA, USA

W. Skorupa
T. Gebel[1]
R.A. Yankov
S. Paul[2]
W. Lerch[2]
D.F. Downey[3]
E.A. Arevalo[3]
M. Smith[4]
R.A. McMahon[4]

Advanced thermal processing of B^+ and BF_2^+ implanted junctions using flash lamps

The effects of flash lamp annealing (FLA) on the formation of ultra-shallow implanted junctions (USJs) were studied. Critical parameters in the processing of USJs by FLA are the duration of the light pulse, the peak temperature, and the preheating temperature. An effective anneal time of 20 ms is much too long for fabricating USJ that meet the 90 nm technology node requirements while an effective time not exceeding 3 ms is advantageous and gives much better results. This is due to heating of the sample influencing primarily the front near-surface region while permitting rapid quenching through conductive heat loss to the substrate. Computer simulation of the flash-induced heat flow in the silicon wafer clearly confirmed this finding. The quality of the final USJ depends crucially on the use of an optimized thermal budget. The implant/anneal conditions producing the best combinations of R_s/X_j values to meet the 90 nm 70 nm technology node requirements were defined.

Supported by EU

Collaboration: [1]nanoparc GmbH, Dresden; [2]Mattson GmbH, Dornstadt; [3]Varian Semiconductor Equipment Ass., Gloucester, MA, USA; [4]Engineering Dept., Cambridge University, UK

D. Grambole
F. Herrmann
Ü. Dagkaldiran[1]
J. Meijer[1]

Micro RBS-channeling measurements to study damage accumulation in silicon by ion implantation

To extend the investigation of the damage accumulation during ion implantation in silicon to very high ion beam densities, Si samples were implanted with 600 keV Si^+ ions of a current density of 360 µA/cm² (2.2×10^{15} Si/s cm^2) at different substrate temperatures (T = 50 – 400°C) up to a fluence of $1\text{x}10^{18}$ Si/cm^2 using the Bochum ion projector. The damage of the Si crystal in the implanted circular areas of 185 µm diameter was investigated by micro RBS/C (3 MeV He ions) using the Rossendorf nuclear microprobe. A second chamber with a 4-axis goniometer (2 translations, 2 rotations) was installed behind the standard chamber to enable precise sample alignment. For suppression of crystal damage during the RBS/C measurements the beam spot was chosen $\geq 50 \times 50$ µm^2 at a beam current of about 0.6 nA ($< 1.5\times10^{14}$ He/s cm^2). For an implantation fluence of 1×10^{16} Si/cm^2 an amorphization temperature of about 150°C was obtained. This value deviates strongly from that value obtained by extrapolation of published values to the current density used here.

Collaboration: [1]Ruhr-Universität Bochum, Experimentalphysik III, Bochum

R. Kögler
A. Peeva
A. Kuznetsov[1]
J. Christensen[2]
B.G. Svensson[1]
W. Skorupa

Implantation induced excess vacancies in SiGe and related Cu gettering

Implantation-induced excess vacancies and the related Cu gettering was studied in a strained $Si_{0.93}Ge_{0.07}$ layer grown on (100) Si substrate. The excess defects were shown to control the Cu gettering observed by depth profiling with SIMS after rapid thermal annealing at a temperature of 900°C. The excess vacancy and interstitial generation during ion implantation can be simulated by a binary collision process using a computer code such as TRIM.

The simulation predicts a lower excess vacancy generation in SiGe in comparison to Si. However, the vacancy concentration in the SiGe layer was found to be higher than in Si. An additional vacancy concentration of about $3.15\times10^{18}cm^{-3}$ was determined in the SiGe layer besides the calculated implantation-generated excess vacancies. These vacancies were presumably incorporated during SiGe layer deposition on Si substrate. Vacancies may agglomerate in Si and form cavities during annealing. The cavities observed in SiGe by TEM were significantly larger than those in Si.

Supported by DAAD

Collaboration: [1]University of Oslo, Oslo, Norway; [2]Royal Institute of Technology, KTH, Sweden

S. Prucnal[1]
J.M. Sun
X.Q. Cheng
W. Skorupa
A.N. Nazarov[3]
J. Zuk[1]

Electron trapping of rare earth implanted MOS devices

Using ion implantation different luminescent centers (Gd^{3+}, Tb^{3+}, Eu^{3+}, Ce^{3+}, Tm^{3+}, Er^{3+}) were embedded into the SiO_2 layer of purpose-designed MOS capacitors. The electrical properties of these devices such as carrier injection, charge-to-breakdown, charge trapping characteristics, and operation lifetime for dedicated applications are under evaluation. The trapping of negative charges during high-field electron injection at low level ($10^{15} \div 10^{19} e^-/cm^2$) from the Si substrate of ITO-SiO_2-Si structures shows distinct differences for the different RE's in dependence on the annealing temperature and concentration. For Gd implanted devices the trapping rate for Gd concentrations of 0.25 – 9% is always lower than in unimplanted SiO_2 layers. The concentration dependence for the implanted devices shows no simple increase of the trapping rate with increasing concentration but a maximum for 3% where the electroluminescence (EL) shows an optimum. Further investigations regarding the correlation between EL carrier trapping are in progress to clarify the EL degradation mechanism.

Supported by EU (Marie-Curie program) and Humboldt-Stiftung

Collaboration: [1]M. Curie University Lublin, Poland; [2]Institute of Semiconductor Physics, Kyiv, Ukraine

A. Nazarov[1]
J.M. Sun
I.N. Osiyuk[1]
I. P. Tjagulskii[1]
V.S. Lysenko[1]
W. Skorupa
R.A. Yankov[2]
T. Gebel[2]

Correlation of charge trapping and light emission in Er-doped Si rich SiO_2 films

The processes of charge trapping and electro- (EL) and photoluminescence (PL) in erbium implanted silicon dioxide enriched with silicon nanocrystals have been studied. It is shown that for a concentration of the excess Si of 10 at.% there is more than a tenfold increase in the PL intensity at a wavelength of 1540 nm, whereas the EL at the same Si concentration is completely quenched. It is further established that implanting erbium leads to efficient positive charge trapping in the oxide occurring at traps with a giant cross section, and negative charge trapping at traps of a large cross section. In addition, both electron and hole traps of small cross sections ($\sim 10^{-18}$ cm^2) are found to form. Introducing subsequently Si nanocrystals in the oxide leads to the creation of electron traps with a giant cross section whereas increasing the excess Si concentration to 10 at.% suppresses appreciably the processes of charge trapping at electron traps of a large cross section, and at electron and hole traps of a small cross section.

Supported by nanoparc GmbH and DAAD

Collaboration: [1]Institute of Semiconductor Physics, Kyiv, Ukraine; [2]nanoparc GmbH, Dresden

Optoelectronic Materials

S. Sinning
T. Dekorsy
M. Helm
G. Mußler[1]

Reduced sub-picosecond electron relaxation in GaN_xAs_{1-x}

Nitrogen containing III-V-semiconductors have attracted considerable interest over the past few years due to their unique electronic properties and their potential for optoelectronic applications. We investigated time resolved femtosecond carrier dynamics in molecular beam epitaxy (MBE) grown GaN_xAs_{1-x} with a nitrogen fraction of 1.3%. Carrier dynamics are investigated by one-color pump-probe measurements in transmission geometry covering a wide excitation wavelength range from 720 nm to 870 nm (1.7 eV to 1.42 eV). The intraband carrier relaxation time in GaN_xAs_{1-x} was found to be significantly larger than in GaAs. We compared the experimental results with carrier – polar optical phonon scattering rates calculated within the band anticrossing model. From the results we conclude that the slowing down of the carrier relaxation is a result of the strongly modified band structure in GaN_xAs_{1-x}.

Collaboration: [1]Paul-Drude-Institut für Festkörperelektronik, Berlin

A. Dreyhaupt
S. Winnerl
T. Dekorsy
M. Helm

High-intensity THz radiation from a microstructured large-area photoconductor

We have developed a planar large-area photoconducting emitter based on GaAs for impulsive generation of THz radiation. The device consists of an interdigitated electrode metal-semiconductor-metal (MSM) structure which is masked by a second metallization layer isolated from the MSM electrodes. The second layer blocks optical excitation in every second period of the MSM finger structure. Hence charge carriers are excited only in those periods of the MSM structure which exhibit a unidirectional electric field. Constructive interference of the THz emission from accelerated carriers leads to THz electric field amplitudes up to 85 V/cm when excited with fs optical pulses from a Ti:sapphire oscillator with an average power of 100 mW at a bias voltage of 65 V applied to the MSM structure. The intense broad-band radiation characteristic (range 0.5 – 3.5 THz) of the planar large-area photoconducting emitter provides an excellent tool for spectroscopic applications.

A. Dreyhaupt
S. Winnerl
T. Dekorsy
M. Helm
T. Roch[1]
G. Strasser[1]

Transport study and infrared spectroscopy of semiconductor superlattices

Electric transport and interminiband transitions in doped GaAs/AlGaAs superlattices with miniband width of 5 meV has been investigated in the temperature range from 5 K to 300 K. The current-voltage characteristics of the superlattices showed regions of negative differential conductance. Analyzing the results with a model based on Bloch oscillations of miniband electrons, intraminiband relaxation times between 0.5 ps (low temperature) and 0.2 ps (room temperature) were obtained. Infrared Fourier transform spectra of the same superlattices showed clear features for the 1s-2p_z donor transition and the *interminiband* transitions in the center and on the edge of the minibrillouin zone, where the joint density of states is highest. The experiments gave evidence for coherent miniband transport in the superlattices. The sample design, namely the doping of the superlattices and the contact layers, was optimized for planned *intraminiband* spectroscopy experiments in the THz frequency range. Such experiments can indicate Bloch gain in superlattices.

Collaboration: [1]Technische Universität Wien, Institut für Festkörperelektronik, Wien, Österreich

S. Winnerl
S. Sinning
T. Dekorsy

Increased terahertz emission from thermally treated GaSb

We investigated the emission of THz radiation from GaSb excited with femtosecond laser pulses. Annealing the samples in the temperature range

M. Helm

from 300 – 700°C allowed to modify the surface stoichiometry. While almost no radiation was emitted by the virgin samples, a maximum of THz emission was found for samples annealed at 500°C. The emitted radiation was in the frequency range from 0.5 – 3.5 THz. The efficiency of the annealed GaSb emitter was comparable to the efficiency of a GaAs surface field emitter. The emission was associated with the build-up of an electric surface field, which is responsible for the acceleration of photoexcited carriers. Using Raman spectroscopy a thermal decomposition of the GaSb surface was observed. This was confirmed by the observation of Sb coherent phonons in pump-probe spectroscopy experiments. The analysis of the Raman spectra furthermore indicated the presence of a surface electric field, which is consistent with the THz emission. The small-gap material GaSb (E_g = 0.726 eV) has the potential to be used as a surface-field THz emitter in a compact THz source, which is optically excited with an Er^{3+}-doped femtosecond fiber laser.

S. Menzel
C.V.-B. Tribuzy
N. Georgiev
T. Dekorsy
M. Helm
K. Biermann[1]
H. Künzel[1]

Intersubband transitions in InGaAs/AlAsSb quantum well structures for application in short-wavelength quantum cascade lasers and modulators

Intersubband transitions (ISBT) in semiconductor quantum wells have been attracting much attention in various infrared optoelectronic device applications. For realizing devices that can be employed at wavelengths < 2 µm, large conduction band offsets (> 1 eV) are required, which are e.g. offered by the InGaAs/AlAsSb heterosystem, lattice matched to InP substrates. The relaxation dynamics in multi-quantum wells based on this material system was investigated with a newly built pump-probe setup employing an optical parametric oscillator (OPO) as a radiation source for the desired wavelength range. Preliminary results show an intersubband relaxation times of 0.5 ps. Furthermore mesa processing of InGaAs/AlAsSb quantum cascade emitter structures was developed in order to measure electric transport, photocurrent and electroluminescence. These experiments are of great interest for applications in future high-rate optical communication networks.

Supported by DFG

Collaboration: [1]Fraunhofer Institut für Nachrichtentechnik, Heinrich-Hertz-Institut, Berlin

D. Stehr
M. Krenz
T. Dekorsy
M. Helm
F. Schrey[1]
K. Unterrainer[1]

Degenerate pump-probe measurements on III-V semiconductor heterostructures

The relaxation properties of n-doped GaAs/AlGaAs superlattices and InAs/GaAs self-assembled quantum dots were investigated in a degenerate pump-probe experiment using the free-electron laser (FEL). First the absorption behavior was characterized over the relevant spectral region by FTIR in order to identify the resonant transitions. The pump-probe measurements with the FEL were performed both in macrobunch-mode and in cw-mode at 13 MHz repetition rate. Due to the very fast relaxation of excited carriers by LO-phonon scattering (< 1 ps) and the very broad absorption spectra (9 – 22 µm) in the case of the superlattice, we were able to measure an autocorrelation signal for the complete wavelength regime of the FEL to determine the pulse length (2 – 4 ps). By switching from macropulse- into cw-mode we were also able to measure carrier-relaxation at longer timescales due to the increase of the S/N-ratio. In this mode we also could detect a pump-probe-signal from the quantum dot sample, where the relaxation is slowed down by polaron formation. Measuring this relaxation time is of great interest for future applications of fast optoelectronic devices featuring quantum dots.

Collaboration: [1]Technische Universität Wien, Institut für Photonik, Wien, Österreich

U. Helbig[1]
M. Krenz
T. Dekorsy

Set up of an autocorrelator and characterization of a laser based plasma switch

The free electron laser (FEL) operated with the ELBE accelerator, at which

first lasing was demonstrated on May 07, 2004, is designed for pulsed operation with a repetition rate of 13 MHz. Since the average power of the order of >10 W is too high for many experiments, a pulse picking system is needed for experiments with high peak power but low average power. The pulse picking system is based on a semiconductor slab illuminated by a laser pulse with high fluence (10 mJ/cm²) which modifies the reflectivity and transmission of a Ge wafer by high-density excitation of carriers. In a first experiment autocorrelators based on second harmonic generation and on two-photon absorption in the photodiodes were built up. The autocorrelator based on second harmonic generation yielded the correct pulse duration of the order of 10 ps, while the autocorrelator based on two photon absorption yielded somewhat longer times, depending on the pulse intensity. A diode laser operating at the wavelength of 7.7 µm was used to measure the change of reflectivity and transmission of the Ge wafer when illuminated with the switch laser. The results are important for the final design of the pulse picking system for the FEL.

Collaboration: [1]Hochschule Mittweida (FH), Mittweida

J.M. Sun
W. Skorupa
T. Dekorsy
M. Helm
L. Rebohle[1]
T. Gebel[1]

Efficient electroluminescence from Tb-implanted MOS light emitting devices

Strong green electroluminescence (EL) with brightness up to 2800 cd/m^2 was realized with indium-tin-oxide/SiO_2:Tb/Si MOS light emitting devices. The SiO_2:Tb^{3+} gate oxide was prepared by thermal oxidation followed by Tb^+ implantation. EL and PL properties were studied, varying the Tb^{3+} ion concentration and the annealing temperature. The EL efficiency increased linearly with increasing the implantation doses for a Tb concentration below 2%. The optimized device shows a high external quantum efficiency of 16 % and a luminous efficiency of 2.1 lm/W. The excitation processes of the strong green EL is attributed to the impact excitation of the Tb^{3+} luminescent centers by hot electrons The cross-relaxation from the higher excited levels to the lowest excited levels of Tb^{3+} restricts the concentration quenching of the green luminescence peaks enabling the fabrication of efficient green EL devices at a high Tb concentration. Light emitting devices with micrometer size were demonstrated.

Collaboration: [1]nanoparc GmbH, Dresden

H.-J. Fitting[1]
T. Ziems[1]
A. von Czarnowski[1]
B. Schmidt

Luminescence center transformation in wet and dry SiO_2

The main luminescent centers in SiO_2 films are the red luminescence R (1.85 eV) of the nonbridging oxygen hole center (NBOHC) and the oxygen deficient center (ODC) with a blue B (2.7 eV) and an UV (4.4 eV) luminescence. By means of a new "track-stop" technique we have investigated especially the initial luminescence behavior at the beginning of ion irradiation. Thus the blue-emitting center is produced under irradiation, but from existing precursors. Contrary to that, the dose behavior of the red (R) luminescence in wet and dry oxide is quite different, decreasing in wet oxide from a high initial level and increasing in dry oxide from almost zero. We propose a model of luminescence center transformation based on radiolytic dissociation and the reactions of mobile oxygen and hydrogen.

Collaboration:[1]Institut für Physik, Universität Rostock, Rostock

Others

R.I. Grynszpan[1,2]
S. Saude[1,2,3]
W. Anwand
G. Brauer

Positron annihilation investigation and nuclear reaction analysis of helium and oxygen-implanted zirconia

Since irradiation affects the in-service properties of zirconia, we investigated the fluence dependence on production and thermal stability of defects induced by helium and oxygen-ion implantation in single crystals of yttria-fully-stabilized zirconia. In either case, depth profiling by Slow Positron Implantation Spectroscopy (SPIS) detects a distribution of vacancy-type defects peaking at 60% of the projected ion range Rp. Owing to the saturation of positron-trapping occurring for low fluences, which depends on the ion mass, we could estimate a critical size of clusters ranging from 0.4 to 1.6 nm. The lack of SPIS-evidence of an open-volume excess at Rp is explained by the presence of over-pressurized gas bubbles. This assumption is confirmed by NRA of ^3He concentration profiles, which shows that helium remains partly trapped at Rp, even after annealing above 400°C.

Collaboration: [1]Lasers, Optics and Thermo-optics Department, DGA/DCE/CTA, Ministere de la Defense, Arcueil, France; [2]LCMTR, UPR-209, ISCSA, IFR-CNRS-1780, Thiais, France; [3]SINUMEF, Ecole Nationale Superieure d'Arts et Metiers, Paris, France

A. Macková[1]
R. Grötzschel
F. Eichhorn
P. Nekvindová[2]
J. Špirková[2]

Characterisation of Er:$LiNbO_3$ and APE:Er:$LiNbO_3$ by RBS/channeling and XRD analysis

Erbium doped lithium niobate (Er:$LiNbO_3$) as a non-linear optical material was prepared by standard Czochralski growth and treated by an annealed proton exchange (APE) procedure to achieve locally a change of the refractive index for use as planar waveguides. Samples with X-, Y- and Z-cut, respectively were studied. It was shown by detailed RBS/C lattice site location measurements of Er atoms that in the pristine crystal Er occupies a site about 0.03 nm shifted in z-direction from the Li site. This shift can be explained by the different atomic sizes. After the APE treatment at 213°C for 3 hours in adipic acid, in course of which the Li is partly replaced by H, the z-shift of Er atoms amounts to nearly 0.1 nm. This corresponds to the XRD results showing an increase of the net plane distances both for the X- and the Y-cut samples leading to an enlarged average volume of the elementary cell after APE. During this treatment a remarkable lattice damage occurs which is seen both by XRD and by RBS/C. The dependence of this damage on the APE parameters is not yet understood and further studies are necessary.

Supported by Grant Agency of the Czech Republic

Collaboration: [1]Nuclear Physics Institute, Academy of Sciences of the Czech Republic, Řež near Prague, Czech Republic; [2]Department of Inorganic Chemistry, Institute of Chemical Technology, Prague, Czech Republic

A.A. Shiryaev[1]
D. Grambole
F. Herrmann

Hydrogen diffusion in diamonds

A representative set of natural and synthetic diamonds with variable concentrations ($0 \div 0.3$ at.%) of different types of nitrogen point defects were annealed in an Ar/H_2 atmosphere at 900°C for 2 – 72 h. The basic hydrogen level for all samples is between $10^{-2} \div 0.7$ at.%. IR spectroscopy was applied to determine the concentration of N- and H-related defects, whereas µERDA (Si^+ beam, spot size 250×300 μm^2) was used to determine both the depth and spatial distribution of hydrogen. Surprisingly, at depth above 30 - 50 nm only very weak signal from in-diffused hydrogen is observed after annealing which indicates low hydrogen diffusivity. It appears that the hydrogen concentration in cubic growth sectors is higher than in octahedral ones. The hydrogen concentration from ERDA does not correspond neither with the optically-active nitrogen defect density nor the H-related optical features.

This indicates that a significant fraction of hydrogen is present in an optically-inactive state.

Supported by the AvH-Stiftung

Collaboration: [1]Bayerisches Forschungsinstitut für Experimentelle Geochemie und Geophysik, Bayreuth

Equipment

M. Friedrich
W. Bürger
S. Turuc

Operation and development of the electrostatic accelerators

The ***2 MV VdG accelerator*** has been used exclusively for RBS analysis.
The ***5 MV Tandem*** has been applied for ion beam analysis, high-energy implantation and detector development. After the rupture of the charging belt (HVEE, operation time 15800 h) a new belt (CIGO/Italy) and a modified charging system with tungsten foils as chargers has been installed. Stability problems due to self-charging of the inner belt surface were encountered and solved by the installation of a needle array to discharge the inner belt surface. The vacuum control system of the injector and of the accelerator has been modernized using the actor/sensor interface communication technology according to standard EN 50295. The original operation system of the beam diagnostic elements was replaced by a flexible modular control system.
The ***3 MV Tandetron*** has been applied mainly for high-energy implantation and ion beam analysis. By using Rb instead of Li in the charge exchange canal of the injector for negative He ions, the He beam current could be increased by about 30%.
In 2004 the total operating hours of the high-energy accelerators were 1696 h (VdG), 2110 h (5 MV Tandem) and 2524 h (Tandetron).

W. Pilz
Ch. Akhmadaliev
L. Bischoff

Optimized the emitter geometry for a high-performance alloy liquid metal ion source

For the Canion 31Mplus focused ion beam column purchased in 2003, different emitter geometries in a modified source cartridge were tested to extract ion beams from high melting alloys like CoNd and AuGeSi. From highly pure wires from W, Ta and Ni with diameters between 100 and 200 µm, the emitter was constructed as a 0.5 mm long tip spot-welded onto a coil-like filament which takes up the source material. The tip was mechanically shaped to an angle of about 98° corresponding to the Taylor cone. A second design consists of a needle mounted directly on the ceramic socket independent from the surrounding filament coil to prevent a movement of the needle tip during heating. A CoNd alloy LMIS prepared in this way has been successfully operated in the Orsay Physics FIB system for about 6 months.

W. Anwand
Th. Schumann
W. Skorupa
S. Tamme[1]
Th. Graß[1]
L. Rebohle[2]
Th. Trautmann[2]

A commercial prototype of a new flash lamp annealing apparatus

The apparatus was developed in the framework of the European GROWTH project FLASiC devoted to improved SiC/Si heteroepitaxy. During the thermal treatment the wafer is arranged in a sample chamber under vacuum conditions or in Ar atmosphere. The wafer can be heated from the back side by halogen lamps in the range of 700 to 1100°C. Xe flash lamps above the wafer produce a light flash of 20 ms or shorter with an energy up to 300 kJ and an electrical power up to 15 MW. The pulses are formed by an arrangement of capacitors and induction coils. Mirrors focus the light of the lamps onto the sample, the surface of which can be transiently heated to temperatures above the melting temperature. Sample handling and thermal treatment are remotely controlled. Extensive safety features and equipment were installed to provide high-level work safety.

Supported by EU

Collaboration: [1]FHR Anlagenbau GmbH, Ottendorf-Okrilla; [2]nanoparc GmbH, Dresden

Glossary

AES	Auger Electron Spectroscopy
AFM	Atomic Force Microscopy
AMS	Atomic Mass Spectrometry
CEMS	Conversion Electron Mössbauer Spectroscopy
CVD	Chemical Vapour Deposition
EEPROM	Electrically Erasable Programmable Read-Only Memory
EFTEM	Energy Filtered Transmission Electron Microscopy
EL	Electroluminescence
ERDA	Elastic Recoil Detection Analysis
ESRF	European Synchrotron Radiation Facility, Grenoble
FEL	Free Electron laser
FIB	Focused Ion Beam
FLA / P	Flash Lamp Annealing / Processing
FTIR	Fourier Transform Infrared Spectroscopy
GDOS	Glow Discharge Optical Spectroscopy
GIXRD	Gracing Incidence X-ray Diffraction
HRTEM	High-resolution Transmission Electron Microscopy
IBAD	Ion Beam Assisted Deposition
ITO	Indium-Tin Oxide
LED	Light Emitting Diode
LMIS	Liquid Metal Ion Source
MBE	Molecular Beam Epitaxy
MFM	Magnetic Force Microscopy
MOKE	Magneto-Optic Kerr Microscopy
MOS	Metal-Oxide-Semiconductor
MOSFET	Metal-Oxide-Semiconductor Field Effect Transistor
NRA	Nuclear Reaction Analysis
OES	Optical Emission Spectroscopy
PAS	Positron Annihilation Spectroscopy
PECVD	Plasma Enhanced Chemical Vapour Deposition
PIGE	Proton-Induced Gamma-Ray Emission
PIII	Plasma Immersion Ion Implantation
PIXE	Proton-Induces X-ray Emission
PLAD	Pulsed Laser Assisted Deposition
PVD	Physical Vapour Deposition

RHEED	Reflection-high Energy Electron Diffraction
ROBL	**RO**ssendorf **B**eam**L**ine (at the ESRF)
RBS	Rutherford Backscattering Spectroscopy
RBS/C	Rutherford Backscattering Spectroscopy under Channelling Conditions
RT	Room Temperature
RTA	Rapid Thermal Annealing
SAD	Selected Area Diffraction
SEM	Scanning Electron Microscopy
SIMS	Secondary Ion Mass Spectrometry
SPIS	Slow Positron Implantation Spectroscopy
STM	Scanning Tunnel Microscope
TEM	Transmission Electron Microscopy
TRIDYN	Ion Implantation Simulation Program (incl. dynamic target modifications)
TRIM	Trajectories of Ions in Matter (Computer-Program)
USJ	Ultra-Shallow Junction
VSM	Vibrating Sample Magnetometry
XANES	X-ray Absorption Near Edge Structure
XPS	X-ray Photoelectron Spectroscopy
XRD	X-ray Diffraction
XTEM	Cross-section Transmission Electron Microscopy

Supporting Institutions

AiF	Arbeitsgemeinschaft Industrieller Forschungsvereinigungen e.V.
AvH	Alexander-von-Humboldt Stiftung
BMBF	Bundesministerium für Bildung und Forschung
BMWA	Bundesministerium für Wirtschaft und Arbeit
DAAD	Deutscher Akademischer Austauschdienst
DFG	Deutsche Forschungsgemeinschaft
EU	European Union
MPG	Max-Planck-Gesellschaft
SMWK	Sächsisches Staatsministerium für Wissenschaft und Kunst
SMWA	Sächsisches Staatsministerium für Wirtschaft und Arbeit
WTZ	BMBF-Programm der „Wissenschaftlich-Technischen Zusammenarbeit“

Statistics

Publications

Abd El-Rahman, A.M., El-Hossary, F.M., Negm, N.Z., Prokert, F., Richter, E., Möller, W.
Influence of gas pressure and substrate temperature on PIII nitrocarburizing process of AISI 304 stainless steel
Nucl. Instr. and Meth. B **226** (2004) 499

Abd El-Rahman, A.M., El-Hossary, F.M., Fitz, T., Negm, N.Z., Prokert, F., Richter, E., Möller, W.
Effect of N_2 *to* C_2H_2 *ratio on rf plasma surface treatment of austenitic stainless steel*
Surf. Coat. Technol. **183** (2004) 286

Abd El-Rahman, A.M., Negm, N.Z., Prokert, F., El-Hossary, F.M., Richter, E., Möller, W.
Depth-related microstructure of rf plasma nitrocarburized austenitic stainlees steel
Surf. Coat. Technol. **191** (2004) 140

Abendroth, B., Gago, R., Eichhorn, F., Möller, W.
X-ray diffraction study of stress relaxation in cubic boron nitride films grown with simultaneous medium-energy ion bombardment
Appl. Phys. Lett. **85** (2004) 5905

Abendroth, B., Gago, R., Kolitsch, A., Möller, W.
Stress measurement and stress relaxation during magnetron sputter deposition of cubic boron nitride thin films
Thin Solid Films **447-448** (2004) 131

Aidinis, C.J., Bischoff, L., Mair, G.L.R., Londos, C.A., Ganetsos, Th., Akhmadaliev, C.
Study of a liquid metal field ion emitter for the production of Si ions
Microel. Eng. **73-74** (2004) 116

Aidinis, C.J., Mair, G.L. R., Bischoff, L., Londos, C.A., Akhmadaliev, C., Ganetsos, Th.
The temperature dependence of the energy distribution of the beam emitted by a $Au_{82}Si_{18}$ *liquid metal field-ion emitter*
Nucl. Instr. and Meth. B **222** (2004) 627

Akhmadaliev, C., Bischoff, L., Mair, G.L.R., Aidinis, C.J., Ganetsos, Th.
Investigation of emission instabilities of liquid metal alloy ion sources
Microel. Eng. **73-74** (2004) 120

Alves, E., Ramos, A.R., Barradas, N.P., Vaz, F., Cerqueira, P., Rebouta, L., Kreißig, U.
Ion beam studies of TiN_xO_y *thin films deposited by reactive magnetron sputtering*
Surf. Coat. Technol. **180-181** (2004) 372

Andreasen, K.P., Jensen, T., Petersen, J.H., Chevallier, J., Bøttiger, J., Schell, N.
The structure and the corresponding mechanical properties of magnetron sputtered TiN–Cu nanocomposites
Surf. Coat. Technol. **182** (2004) 268

Andreasen, K.P., Schell, N., Jensen, T., Petersen, J.H., Jensen, M.S., Chevallier, J., Bøttiger, J.
On the development of the <111> fiber texture in nanocrystalline gold during growth and annealing
Mat. Res. Soc. Symp. Proc. **788** (2004) 49

Anwand, W., Brauer, G., Kuriplach, J., Skorupa, W.
Slow positron beam investigations of defects caused by B implantation into epitaxial 6H-SiC
Mat. Sci. Forum **445-446** (2004) 60

Arazi, A., Faestermann, T., Fernandez Niello, J.O., Frischke, D., Knie, K., Korschinek, G., Maier, H.J., Richter, E., Rugel, G., Wallner, A.
Magnesium suppression for ^{26}Al measurements using AlO-ions
Nucl. Instr. and Meth. B **223-224** (2004) 259

Ayache, R., Richter, E., Bouabellou, A.
Microstructure of β-$FeSi_2$ buried layers synthesis by ion implantation
Nucl. Instr. and Meth. B **216** (2004) 137

Ayache, R., Bouabellou, A., Richter, E.
Optical characterization of β-$FeSi_2$ layers formed by ion beam synthesis
Mat. Sci. Semicond. **7** (2004) 464

Azzaroni, O., Fonticelli, M.H., Benítez, G., Schilardi, P.L., Gago, R., Caretti, I., Vázquez, L., Salvarezza, R.C.
Direct nanopatterning of metal surfaces using self-assembled molecular films
Adv. Mat. **16** (2004) 405

Azzaroni, O., Fonticelli, M., Schilardi, P.L., Benítez, G., Caretti, I., Albella, J.M., Gago, R., Vázquez, L., Salvarezza, R.C.
Surface nanopatterning of metal thin films by physical vapour deposition onto surface-modified silicon nanodots
Nanotechnology **15** (2004) 197

Barradas, N.P., Matias, V., Sequelra, A.D., Soares, J.A., Kreißig, U., Wang, J.U., Freitas, P.
He-RBS, He-ERDA and heavy ion-ERDA analysis of Si/Ta 70 Å/CoFe 35 Å/$HfAlO_x$/CoFe 35 Å/Ta 30 Å systems
Nucl. Instr. and Meth. B **219-220** (2004) 742

Beyer, R., Beyreuther, E., Borany, J. von, Weber, J.
Scanning capacitance microscopy and spectroscopy on SiO_2 films with embedded Ge and Si nanoclusters
Microel. Eng. **72** (2004) 207

Bilek, M.M.M., McKenzie, D.R., Möller, W.
Use of low energy and high frequency PBII during thin film diposition to achieve relief of intrinsic stress and microstructural changes
Surf. Coat. Technol. **186** (2004) 21

Bischoff, L., Akhmadaliev, C., Mair, A.W.R., Mair, G.L.R., Ganetsos, Th., Aidinis, C.J.
Investigation of a tin liquid metal ion source
Appl. Phys. A **79** (2004) 89

Bischoff, L., Mair, G.L.R., Mair, A.W.R.
The mass spectrum of a tin liquid metal ion source
Nucl. Instr. and Meth. B **222** (2004) 622

Bischoff, L., Mair, G.L.R., Aidinis, C.J., Londos, C.A., Akhmadaliev, C., Ganetsos, T.
A $Au_{82}Si_{18}$ liquid metal field-ion emitter for the production of Si ions: fundamental properties and mechanisms
Ultramicroscopy **100** (2004) 1

Bohne, Y., Shevchenko, N., Prokert, F., Borany, J. von, Rauschenbach, B., Möller, W.
In situ X-ray diffraction investigations during high-energy oxygen ion implantation in transition metals

Vacuum **76** (2004) 281

Bonafos, C., Carrada, M., Cherkashin, N., Coffin, H., Chassaing, D., Ben Assayag, G., Claverie, A., Müller, T., Heinig, K.-H., Perego, M., Fanciulli, M., Dimitrakis, P., Normand, P.
Manipulation of 2D arrays of Si nanocrystals embedded in thin SiO_2 layers by low energy ion implantation
J. Appl. Phys. **95** (2004) 5696

Boudreault, G., Elliman, R., Grötzschel, R., Gujrathi, S.C., Jeynes, C., Lennard, W.N., Rauhala, E., Sajavaara, T., Timmers, H., Wang, Y.Q., Weijers, T.D.M.
Round Robin: measurement of H implantation distributions in Si by elastic recoil detection
Nucl. Instr. and Meth. B **222** (2004) 547

Bugoi, R., Constantinescu, B., Neelmeijer, C., Constantin, F.
The potential of external IBA and LA-ICP-MS for obsidian elemental characterization
Nucl. Instr. and Meth. B **226** (2004) 136

Cabral, A.R., Lehmann, B., Grambole, D., Herrmann, F.
Hydrogen in a natural Pd-O compound from Gongo Soco, Minas Gerais, Brazil
Canadian Mineralogist **42** (2004) 689

Camero, M., Gago, R., Gomez-Aleixandre, C., Albella, J.M.
Effect of argon on the deposition of ECR-CVD hydrogeneated carbon nidtride films
Boletin de la sociedad espanola de ceramica y vidrio **43** (2004) 491

Caretti, I., Jiménez, I., Gago, R., Abendroth, B., Albella, J.M.
Tribological properties of ternary BCN films with controlled composition and bonding structure
Diam. Rel. Mat. **13** (2004) 1532

Cardoso, S., Ferreira, R., Freitas, P., Mc Kenzie, M., Chapman, J., Ventura, J., Sousa, J., Kreißig, U.
Ferromagnetic coupling field reduction in CoFeB tunnel juctions deposited by ion beam
IEEE Transact. on Magn. **40** (2004) 2272

Cavalleri, A., Dekorsy, T., Chon, H.H.W., Kiefer, J.C., Schoenlein, R.W.
Evidence for a structurally-driven insulator-to-metal transition in VO_2: A view from the ultrafast timescale
Phys. Rev. B **70** (2004) 161102

Chen, X.D., Ling, C.C., Fung, S., Beling, C.D., Wu, H.S., Brauer, G., Anwand, W., Skorupa, W.
Deep level defects in He-implanted n-6H-SiC studied by deep level transient spectroscopy
Mat. Res. Soc. Proc. **815** (2004) J5.5.1

Chun, S.Y., Chayahara, A., Posselt, M.
Limitations on ultra-thin multilayers: pulsed cathodic arc and computer simulation
Surf. Coat. Technol. **182** (2004) 171

Cizek, J., Prochazka, I., Brauer, G., Anwand, W., Kuzel, R., Cieslar, M., Islamgaliev, R.K.
Ultra-fine grained copper prepared by high pressure torsion: spatial distribution of defects
in: Proc. Second Int. Conf. on Nanomaterials by Severe Plastic Deformation: Fundamentals - Processing - Applications, Vienna 2002, eds. M.J. Zehetbauer, R.Z. Valiev (Wiley, Weinheim, 2004)

Cizek, J., Prochazka, I., Becvar, F., Kuzel, R., Cieslar, R., Brauer, G., Anwand, W., Kirchheim, R., Pundt, A.
Hydrogen-induced defects in bulk niobium
Phys. Rev. B **69** (2004) 4106

Cizek, J., Prochazka, I., Kuzel, R., Becvar, F., Cieslar, M., Brauer, G., Anwand, W., Kirchheim, R., Pundt, A.
Hydrogen-induced defects in niobium studied by positron annihilation
Mat. Sci. Forum **445-446** (2004) 60

Danesh, P., Pantchev, B., Antonova, K., Liarokapis, E., Schmidt, B., Grambole, D., Baran, J.
Hydrogen bonding and structural order in hydrogenated amorphous silicon prepared with hydrogen-diluted silane
J. Phys. D: Appl. Phys. **37** (2004) 249

Danesh, P., Pantchev, B., Schmidt, B., Grambole, D.
Hydrogen solubility limit in hydrogenated amorphous silicon
Semicond. Sci. Technol. **19** (2004) 1422

Dekorsy, T.
Free electron lasers in physics
Encyclopedia of Modern Optics, Eds. B.D. Günther and D.G. Steel, Elsevier (2004) 164

Dekorsy, T., Sun, J., Skorupa, W., Schmidt, B., Helm, M.
Light-emitting silicon pn diodes
Appl. Phys. A **78** (2004) 471

Dieter, S., Pyzalla, A., Bauer, A., Schell, N., McCord, J., Seemann, K., Wanderka, N., Reimers, W.
Correlation between magnetic properties of CoFe single and CoFe/SiO_2 multi-layer thin films and their microstructure, texture and internal stress state
Zeitschrift für Metallkunde **95** (2004) 164

Dreyhaupt, A., Winnerl, S., Dekorsy, T., Helm, M.
Large-area high-power THz emitter based on interdigitated electrodes
IEEE Conference digest IRMMW2004/THz2004 (2004) 83

Facsko, S., Bobek, T., Stahl, A., Kurz, H., Dekorsy, T.
Dissipative continuum model for self-organized pattern formation during ion-beam erosion
Phys. Rev. B **69** (2004) 3412

Fassbender, J., Ravelosona, D., Samson, Y.
Tailoring magnetism by light-ion irradiation
J. Phys. D: Appl. Phys. **37** (2004) R179

Fernandez-Hidalgo, P., Martin-Palma, R.J., Conde, A., Gago, R., Simancas, J., Garcia-Diego, I., Egio, A., Martinez-Duart, J.M.
Structural and chemical characterization of functional SiO_xCy: H coatings for polymeric lenses
J. Vac. Sci. Technol. B **22** (2004) 2402

Ferro, G., Panknin, D., Polychroniadis, E., Stoemenos, J., Camassel, J., Skorupa, W., Monteil, Y.
Flash Lamp Supported Deposition of 3C-SiC (FLASiC) - thick 3C-SiC films grown on 35 nm FLASiC layer
Mat. Sci. Forum **457-460** (2004) 313

Fitting, H.-J., Ziems, T., Czarnowski, A. von, Schmidt, B.
Luminescence center transformation in wet and dry SiO_2
Radiation Measurements **38** (2004) 649

Förster, M., Kurz, H., Dekorsy, T., Leavitt, R.
Well-width dependence of coupled Bloch-phonon oscillations in biased InGaAs/InAlAs superlattices

Phys. Stat. Sol. **1** (2004) 2702

Friedrich, M., Pilz, W., Glugla, M., Bekris, N., Kiisk, M., Liechtenstein, V.
A *small and compact AMS facility for depth profiling of tritium and other light elements*
Nucl. Instr. and Meth. B **223-224** (2004) 21

Gao, F., Posselt, M., Belko, V., Zhang, Y., Weber, W.J.
Structures and energetics of defects: a comparative study of 3C- and 4H-SiC
Nucl. Instr. and Meth. B **218** (2004) 74

Gao, F., Weber, W.J., Posselt, M., Belko, V.
Atomic computer simulations of defect migration in 3C and 4H-SiC
Mat. Sci. Forum **457-460** (2004) 457

Gao, F., Weber, W.J., Posselt, M., Belko, V.
Atomistic study of intrinsic defect migration in 3C-SiC
Phys. Rev. B **69** (2004) 245205

Gebel, T., Rebohle, L., Yankov, R.A., Nazarov, A.N., Skorupa, W.
Nanocluster-rich silicon dioxide layers: electroluminescence and charge trapping
Proc. SPIE Int. Soc. Opt. Eng. **5445** (2004) 284

Gomes, G.F., Ueda, M., Reuther, H., Richter, E., Beloto, A.
Chromium recoil implantation into SAE 1020 steel by nitrogen ion bombardment
Braz. J. of Physics **34** (2004) 1629

Grosse, M., Kalkhof, D., Keller, L., Schell, N.
Influence parameters of martensitic transformation during low cycle fatigue for steel AISI 321
Physica B **350** (2004) 102

Grötzschel, R., Klein, C., Mäder, M.
RBS with high depth resolution using small magnetic spectrometers
Nucl. Instr. and Meth. B **219-220** (2004) 344

Güttler, D., Abendroth, B., Grötzschel, R., Depla, D., Möller, W.
Mechanisms of target poisoning during magnetron sputtering as investigated by real-time in situ analysis and collisional computer simulation
Appl. Phys. Lett. **85** (2004) 6134

Heera, V., Mücklich, A., Dubois, C., Voelskow, M., Skorupa, W.
Layer morphology and Al implant profiles after annealing of supersaturated, single crystalline, amorphous and nanocrystalline SiC
J. Appl. Phys. **96** (2004)2841

Heitmann, J., Müller, F., Yi, L., Zacharias, M., Kovalev, D., Eichhorn, F.
Excitons in Si nanocrystals: confinement and migration effects
Phys. Rev. B **69** (2004) 5309

Helm, M.
Intersubband semiconductor light sources: history, status, and future
IEEE Conference digest IRMMW2004/THz2004 (2004) 57

Hennig, C., Reich, T., Kraus, W., Reck, G., Prokert, F., Schell, N.
Combining EXAFS and X-ray powder diffraction to solve structures containing heavy atoms
Physica Scripta **12** (2004) 1

Ignatova, V. A., Conard, T., Möller, W., Vandervorst, W., Gijbels, R.
Depth profiling of $ZrO_2/SiO_2/Si$ stacks - a TOF-SIMS and computer simulation study
Appl. Surf. Sci. **231-2** (2004) 603

Jembrih-Simbürger, D., Neelmeijer, C., Mäder, M., Schreiner, M.
X-ray fluorescence and ion beam analysis of iridescent Art Nouveau glass - authenticity and technology
Nucl. Instr. and Meth. B **226** (2004) 119

Kagadei, V., Nefyodtsev, E., Proskurovsky, D., Romanenko, S., Shevchenko, V., Grambole, D., Grötzschel, R., Herrmann, F., Ivanov, Y.
The effect of atomic hydrogen flow on electrical resistance of the transition metal films
Sensors and Actuators A **113** (2004) 293

Kaschieva, S., Dmitriev, S. N., Skorupa, W.
Reduction of the annealing temperature of radiation-induced defects in ion-implanted MOS structures
Appl. Phys. A **78** (2004) 607

Kentsch, U., Landgraf, S., Schmidt, M.
Slow highly charged ions for nanoscale surface modifications
Nucl. Instr. and Meth. B **216** (2004) 196

Kögler, R., Peeva, A., Kuznetsov, A., Christensen, J., Svensson, B.G., Skorupa, W.,
Ion beam induced excess vacancies in Si and SiGe and related gettering
Sol. State Phenom. **95-96** (2004) 587

Kokkoris, M., Perdikakis, G., Kossionides, S., Petrovic, S., Vlastou, R., Grötzschel, R.
A study of the dechanneling of protons in SiC polytype crystals in the energy range E_p=400 - 650 keV
Nucl. Instr. and Meth. B **219-220** (2004) 226

Kondyurin, A.V., Lauke, B., Richter, E.
Polymerization processes of epoxy matric composites under simulated free space conditions
High Performance Polymers **16** (2004) 163

Kondyurin, A.V., Maitz, M.F., Romanova, V.A., Begishev, V.P., Kondyurina, I.V., Günzel, R.
Drug release from polyureaurethane coating modified by plasma immersion ion implantation
J. Biomat. Sci., Polymer Edition **15** (2004) 145

Kostov, K.G., Ueda, M., Lepiensky, A., Soares, P.C., Gomes, G.F., Silva, M.M., Reuther, H.
Surface modification of metal alloys by plasma immersion ion implantation and subsequent plasma nitriding
Surf. Coat. Technol. **186** (2004) 204

Krause-Rehberg, R., Brauer, G., Leipner, H.S.
EPOS - intensive Positronenquelle für die Materialforschung
Scientia Halensis **2** (2004) 13

Krawczyk-Bärsch, E., Arnold, T., Reuther, H., Brandt, F., Bosbach, D., Bernhard, G.
Formation of secondary Fe-oxyhydroxide phases during the dissolution of chlorite effect on uranium sorption
Applied Geochemistry **19** (2004) 1403

Kreißig, U., Gago, R., Vinnichenko, M., Fernández-Hidalgo, P., Martín-Palma, R.J., Martínez-Duart, J.M.

Heavy-ion ERDA and spectroscopic ellipsometry characterization of a SiOC: H layered structure as functional coating on polymeric lenses
Nucl. Instr. and Meth. B **219-220** (2004) 908

Leitenberger, W., Wendrock, H., Bischoff, L., Weitkamp, T.
Pinhole interferometry with coherent hard X-rays
J. Synchr. Radiat. **11** (2004) 190

Liechtenstein, V.K., Ivkova, T.M., Olshanski, E.D., Golser, R., Kutschera, W., Steier, P., Vockenhuber, C., Repnow, R., Hahn, R. von, Friedrich, M., Kreißig, U.
Recent investigations and applications of thin diamond-like carbon (DLC) foils
Nucl. Instr. and Meth. A **521** (2004) 197

Linss, V., Rodil, S.E., Reinke, P., Garnier, M.G., Oelhafen, P., Kreißig, U., Richter, F.
Bonding characteristics of DC magnetron sputtered B-C-N thin films investigated by Fourier-transformed infrared spectroscopy and X-ray photoelectron spectroscopy
Thin Solid Films **467** (2004) 76

Lopes, J.M.J., Zawislak, F.C., Fichtner, P.F.P., Behar, M., Rebohle, L., Skorupa, W.
Pre-irradiation memory effect on the photoluminexcence intensity of Ge-implanted SiO_2 layers
Nucl. Instr. and Meth. B **218** (2004) 438

Mackova, A., Grötzschel, R., Eichhorn, F., Nekvindova, P., Spirkova, J.
Characterization of Er: $LiNbO_3$ and APE: Er: $LiNbO_3$ by RBS-channeling and XRD techniques
Surf. Interf. Analysis **36** (2004) 949

Mair, G.L.R., Akhmadaliev, C., Bischoff, L., Ganetsos, Th., Aidinis, C.J., Anagnostakis, E.A.
The effect of electrode geometry on the stability of a liquid metal ion emitter
Nucl. Instr. and Meth. B **217** (2004) 347

Markwitz, A., Kennedy, V.J., Durbin, S.M., Johnson, P.B., Mücklich, A., Dytlewski, N.
Depth profiling of light elements in PAMBE-grown GaN and helium-implanted titanium with heavy ion time-of-flight elastic recoil detection
Surf. Inter. Anal. **36** (2004) 317

Martín-Palma, R.J., Gago, R., Vinnichenko, M., Martínez-Duart, J.M.
In-depth optical and structural study of silver-based low-emissivity multilayer coatings for energy-saving applications
J. Phys. D: Appl. Phys. **37** (2004) 1554

Martins, R.M.S., Silva, R.J.C., Braz Fernandes, F.M., Pereira, L., Gordo Paulo, R., Maneira Manuel, J. P., Schell, N.
In-situ GIXRD characterization of the crystallization of Ni-Ti sputtered thin films
Mat. Sci. Forum **455-456** (2004) 342

May-Tal Beck, S., Brauer, G., Anwand, W., Berant, Z., Shahal, O., Ganor, M., Israelashwily, I.
Reliability test of a PAL spectrometer - selected results on Fe
Mat. Sci. Forum **445-446** (2004) 495

Misochko, O.V., Lebedev, M., Georgiev, N., Dekorsy, T.
Coherent phonons in $NdBa_2Cu_3O_{7-x}$ single crystals: Optical-response anisotropy and hysteretic behavior
J. Exp. Theor. Phys. **98** (2004) 341

Mizoguchi, K., Hino, T., Nakayama, M., Dekorsy, T., Bartels, A., Kurz, H., Nakashima, S.

Umklapp process in observation of coherent folded longitudinal acoustic phonons in a GaAs/AlAs long-period superlattice
Physica E **21** (2004) 646

Mukherjee, S., Prokert, F., Richter, E., Möller, W.
Compressive stress, preferred orientation and film composition in Ti-based coatings developed by plasma immersion ion implantation-assisted deposition
Surf. Coat. Technol. **186** (2004) 99

Müller, T., Bonafos, C., Heinig, K.-H., Tencé, C., Coffin, H., Cherkashin, N., Ben Assayag, G., Schamm, S., Zanchi, G., Colliex, C., Möller, W., Claverie, A.
Multi-dot floating-gates in MOSFETs for nonvolatile memories - their ion beam synthesis and morphology
Appl. Phys. Lett. **85** (2004) 2373

Music, D., Kreißig, U., Mertens, R., Schneider, J.M.
Electronic structure and mechanical properties of Cr_7C_3
Phys. Lett. A **326** (2004) 473

Neelmeijer, C., Mäder, M.
Reverse painting on glass as seen by the proton beam
Nucl. Instr. and Meth. B **226** (2004) 126

Panknin, D., Godignon, P., Mestres, N., Polychroniadis, E., Stoemenos, J., Ferro, G., Pezoldt, J., Skorupa, W.
Formation of 3C-SiC films embedded in SiO_2 *by sacrificial oxidation*
Mat. Sci. Forum **445-446** (2004) 1515

Pantchev, B., Danesh, P., Liarokapis, E., Schmidt, B., Schmidt, J., Grambole, D.
Effect of post-hydrogenation on the structural properties of amorphous silicon network
Jap. J. Appl. Phys. **43** (2004) 454

Pecheva, E.L., Pramatarova, L., Maitz, M.F., Pham, M.T., Kondyurin, A.
Extreacellular matrix used in an in-vitro model system for hydroxyapatite formation
Ann. Transplant. **9** (2004) 58

Pecheva, E.L., Pramatarova, L., Maitz, M.F., Pham, M.T., Kondyurin, A.
Kinetics of hydroxyapatite deposition on solid substrates by sequential implantation of Ca and P ions, Part I: FTIR and Raman spectroscopy study
Appl. Surf. Sci. **235** (2004) 176

Pecheva, E.L., Pramatarova, L., Maitz, M.F., Pham, M.T., Kondyurin, A.
Kinetics of hydroxyapatite deposition on solid substrates by sequential implantation of Ca and P ions, Part II: Morphological, composition and structure study
Appl. Surf. Sci. **235** (2004) 170

Pecz, B., Toth, L., Dobos, L., Szuts, T., Heera, V., Skorupa, W., Dekorsy, T.
TEM sudy of GaAs implanted by high dose nitrogen ions
13th Int. Conf. on Microscopy of Semiconducting Materials Churchill College, University of Cambridge, 31 March – April 3, 2003
Inst. Phys. Conf. Ser. No. **180** (2004) 441

Peeva, A., Kögler, R., Skorupa, W., Kuznetsov, A., Christensen, J.
Spatial distribution of cavities in silicon formed by ion implantation generated excess vacancies
J. Appl. Phys. **95** (2004) 4738

Peikert, M., Bhandari, R., Wieser, E., Wenzel, C., Mücklich, A.
The effect of silicon ion implantation on the structure of tantalum-silicon contacts
Thin Solid Films **449** (2004) 187

Pełka, J. B., Andrejczuk, A., Reniewicz, H., Schell, N., Krzywinski, J., Sobierajski, R., Wawroa, A., Zytkiewicz, Z. R., Klinger, D., Juha, L.
Structure modifications in silicon irradiated by ultra-short pulses of XUV free electron laser
J. Alloys and Compounds **382** (2004) 264

Pham, M.T., Maitz, M.F., Reuther, H., Richter, E., Matz, W., Mücklich, A., Shevchenko, N., Prokert, F.
Redox and electrocatalytic activity of Ni ion-implanted Ti
J. Mat. Res. **19** (2004) 1249

Pham, M.T., Maitz, M.F., Reuther, H., Mücklich, A., Prokert, F., Steiner, G.
Nucleation of calcium phosphate by surface-bound extracellular matrix
J. Biomed. Mat. Res. A **71** (2004) 16

Pham, M.T., Maitz, M.F., Reuther, H., Richter, E., Matz, W., Mücklich, A., Prokert, F.
Electrochemical behaviour of bimetallic Ni-Ti surface generated by ion implantation
J. Mat. Res. **19** (2004) 439

Pham, M.T., Maitz, M.F., Richter, E., Reuther, H., Mücklich, A., Prokert, F.
Enhancement in redox and electrocatalytic activity observed on Si ion-implanted Ni
J. Mat. Res. **19** (2004) 616

Pham, M.T., Maitz, M.F., Richter, E., Reuther, H., Prokert, F., Mücklich, A.
Electrochemical behaviour of nickel surface-alloyed with copper and titanium
J. Electroanal. Chemistry **572** (2004) 185

Piazza, F., Grambole, D., Zhou, L., Talke, F., Casiraghi, C., Ferrari, A.C., Robertson, J.
Large area deposition of hydrogenated amorphous carbon films for optical storage disks
Diam. Rel. Mat. **13** (2004) 1505

Piekoszewski, J., Sartowska, B., Walis, L., Werner, Z., Kopcewicz, M., Prokert, F., Stanislawski, J., Kalinowska, J., Szymczyk, W.
Interaction of nitrogen atoms in expanded austenite formed in pure iron by intense nitrogen plasma pulses
Nukleonika **49** (2004) 57

Pilz, W., Friedrich, M., Heinig, K.-H., Schmidt, B., Borany, J. von
AMS depth profiling of humidity in silica
Nucl. Instr. and Meth. B **219-220** (2004) 459

Polychroniadis, E., Stoemenos, J., Ferro, G., Monteil, Y., Panknin, D., Skorupa, W.
Structural characterization of thin 3C-SiC films annealed by the flash lamp process
Mat. Sci. Forum **457-460** (2004) 351

Posselt, M., Gao, F., Weber, W. J., Belko, V.
A comparative study of structure and energetics of elementary defects in 3C- and 4H-SiC
J. Phys. Cond. Matter **16** (2004) 1307

Potfajova, J., Sun, J.M., Winnerl, S., Dekorsy, T., Skorupa, W., Schmidt, B., Helm, M., Mantl, S., Breuer, U.
Silicon-based electrically driven microcavity LED

Electronics Letters **40** (2004) 904

Pramatarova, L., Pecheva, E.L., Maitz, M.F., Pham, M.T., Kondyurin, A.
Growth of hydroxyapatite layers on solid surfaces patterned by ion implantation
Ann. Transplant. **9** (2004) 40

Prokert, F., Kravtsov, E., Milyaev, M., Romashev, L., Ustinov, V.
X-ray study of in-plane layer stress and orientation degree in Fe/Cr multilayers grown by MBE on R-plane sapphire
Zeitschrift für Kristallographie **21** (2004) 142

Reuther, H., Arnold, T., Krawczyk-Bärsch, E.
Quantification of secondary Fe-phases formed during sorption experiments on chlorites
Hyperfine Interactions **156-157** (2004) 439

Reuther, H., Richter, E., Prokert, F., Ueda, M., Beloto, A.F., Gomes, G.F.
Investigation of steel surfaces treated by a hybrid ion implantation technique
Hyperfine Interactions **156** (2004) 575

Rogozin, A.I., Vinnichenko, M.V., Kolitsch, A., Möller, W.
Effect of deposition parameters on properties of ITO films prepared by reactive MF pulsed dual magnetron sputtering
J. Vac. Sci. Technol. A **22** (2004) 349

Rogozin, A., Shevchenko, N., Vinnichenko, M., Prokert, F., Cantelli, V., Kolitsch, A., Möller, W.
Real-time evolution of the ITO film properties and structure during annealing in vacuum
Appl. Phys. Lett. **85** (2004) 212

Röntzsch, L., Heinig, K.-H., Schmidt, B.
Experimental evidence of Si nanocluster delta-layer formation in buried and thin SiO_2 films induced by ion irradiation
Mat. Sci. in Semicond. Proc. **7** (2004) 357

Saude, S., Grynszpan, R.I., Anwand, W., Brauer, G., Grob, J.J., Le Gall, Y.
Fluence dependence and thermal stability of defects in helium-implanted cubic zirconia
Nucl. Instr. and Meth. B **216** (2004) 156

Saude, S., Grynszpan, R.I., Anwand, W., Brauer, G.,
Defect production in ion-implanted yttria-stabilized zirconia investigated by positron depth profiling
J. Alloys and Compounds **382** (2004) 252

Schell, N., Jensen, T., Petersen, J.H., Andreasen, K.P., Bøttiger, J., Chevallier, J.
The nanostructure evolution during and after magnetron deposition of Au films
ESRF Highlights **2003** (2004) 39

Schneeweiss, O., Pizurova, N., Jiraskova, Y., Zak, T., Bezdicka, P., Reuther, H.
Phase composition and properties of iron nanocrystals and clusters embedded in MgO matrix
Hyperfine Interactions **156** (2004) 81

Seidel, J., Baida, F.I., Bischoff, L., Guizal, B., Grafström, S., Labeke, D. van, Eng, L.M.
Coupling between surface plasmon modes on metal films
Phys. Rev. B **69** (2004) 121405

Semtsiv, M.P., Ziegler, M., Dressler, S., Masselink, W.T., Georgiev, N., Dekorsy, T., Helm, M.

Above room temperature operation of short wavelength (λ = 3.8 μm) strain-compensated $In_{0.73}Ga_{0.27}As$–AlAs quantum-cascade lasers
Appl. Phys. Lett. **85** (2004) 1478

Shevchenko, N., Pham, M. T., Maitz, M. F.
Studies of surface modified NiTi alloy
Appl. Surf. Sci. **235** (2004) 126

Sinning, S., Dekorsy, T., Helm, M.
Ultrafast carrier dynamics in nitrogen implanted GaAs
IEE Proc. Optoelectronics **151** (2004) 361

Skorupa, W., Anwand, W., Panknin, D., Voelskow, M., Ferro, G., Monteil, Y., Leycuras, A., Pezoldt, J., McMahon, R., Smith, M., Camassel, J., Stoemenos, J., Polychroniadis, E., Godignon, P., Mestres, N., Turover, D., Rushworth, S. Friedberger, A.
Flash Lamp Supported Deposition of 3C-SiC (FLASiC) – a promising technique to produce high quality cubic SiC layers
Mat. Sci. Forum **457-460** (2004) 175

Skorupa, W., Dekorsy, T., Gebel, T., Helm, M., Lysenko, V.S., Nazarov, A.N., Osiyuk, I.N., Rebohle, L., Schmidt, B., Sun, J.M.
Ion beam processing for silicon - based light emission
Mat. Res. Soc. Symp. Proc. **792** (2004) R11.1.1

Skorupa, W., Panknin, D., Voelskow, M., Anwand, W., The European FLASiC Consortium, Gebel, T., Yankov, R.A., Paul, S., Lerch, W.
Advanced thermal processing of semiconductor materials by flash lamp annealing
Mat. Res. Soc. Symp. Proc. **810** (2004) C4.16

Skorupa, W., Yankov, R.A., Anwand, W., Voelskow, M., Gebel, T., Downey, D.F., Arevalo, E.A.
Ultra-shallow junctions produced by plasma doping and flash lamp annealing
Mat. Sci. Eng. B **114-115** (2004) 358

Smith, M., McMahon, R., Voelskow, M., Skorupa, W.
Modeling and regrowth mechanisms of flash lamp processing of SiC-on-silicon heterostructures
J. Appl. Phys. **96** (2004) 4843

Smith, M., McMahon, R., Voelskow, M., Stoemenos, J., Skorupa, W.
Flash lamp supported deposition of 3C-SiC (FLASiC) - Modelling and regrowth mechanism
Mat. Sci. Forum **457-460** (2004) 333

Stoemenos, J., Panknin, D., Eickhoff, M., Heera, V., Skorupa, W.
Improved 3C-SiC films epitaxially grown on Si by flash lamp processing
J. Electrochem. Soc. **151** (2004) G136

Sun, J.M., Dekorsy, T., Skorupa, W., Schmidt, B., Mücklich, A., Helm, M.
Below-band gap electroluminescence related to doping spikes in boron-implanted silicon pn diodes
Phys. Rev. B **70** (2004) 155316

Sun, J.M., Skorupa, W., Dekorsy, T., Helm, M., Rebohle, L., Gebel, T.
Efficient ultraviolet electroluminescence from a Gd-implanted silicon metal-oxide-semiconductor device
Appl. Phys. Lett. **85** (2004) 3387

Tsyganov, I., Maitz, M.F., Wieser, E.

Blood compatibility of titanium-based coatings prepared by metal plasma immersion ion implantation and deposition
Appl. Surf. Sci. **235** (2004) 156

Turos, A., Gaca, J., Wojcik, M., Nowicki, L., Ratajczak, R., Grötzschel, R., Eichhorn, F., Schell, N.
Virtues and pitfalls in structural analysis of compound semiconductors by the complementary use of RBS/channeling and high resolution X-ray diffraction
Nucl. Instr. and Meth. B **219-220** (2004) 618

Ueda, M., Gomes, G., Abramof, E., Reuther, H.
Grazing incidence X-ray diffraction of SS304 steel surfaces modified by high- and low- pressure ion nitriding processes
Surf. Coat. Technol. **186** (2004) 291

Ueda, M., Gomes, G., Kostov, K., Reuther, H., Lepienski, C., Soares, P., Takai, O., Silva, M.
Results from experiments on hybrid plasma immersion ion implantation/nitriding processing of materials
Braz. J. Phys. **34** (2004) 1632

Uglov, V.V., Anishchik, V., Vetushka, A.M., Rumyanceva, I.N., Richter, E.
Structure and phase transformations of AISI M2 high-speed tool steel treated by PIII and subsequent compression plasma flows of nitrogen
Surf. Coat. Technol. **183** (2004) 35

Vandyshev, E.N., Zhuravlev, K.S., Gilinsky, A.M., Skorupa, W.
Enhancement of the photoluminescence of silicon nanocrystals under the influence of electric field
Physica E **21** (2004) 304

Vinnichenko, M., Gago, R., Huang, N., Leng, Y.X., Sun, H., Kreißig, U., Kulish, M.P., Maitz, M.F.
Spectroscopic ellipsometry investigation of amorphous carbon films with different sp3 content: relation with protein adsorption
Thin Solid Films **455-456** (2004) 530

Wang, X., Prokert, F., Reuther, H., Maitz, M.F., Zhang, F.
Chemical Composition and Biocompatibility of Ti-Ag-O films prepared by ion beam assisted deposition
Surf. Coat. Technol. **185** (2004) 12

Weishart, H., Heera, V., Eichhorn, F., Pécz, B., Toth, L., Skorupa, W.
Diamond formation by carbon implantation into cubic silicon carbide
Diam. Rel. Mat. **13** (2004) 627

Winnerl, S., Sinning, S., Dekorsy, T., Helm, M.
Increased terahertz emission from thermally treated GaSb
Appl. Phys. Lett. **85** (2004) 3092

Winnerl, S., Sinning, S., Dekorsy, T., Helm, M.
THz emission from GaSb samples with modified surface stoichiometry
IEEE Conference digest IRMMW2004/THz2004 (2004) 499

Yankov, R.A., Gebel, T., Rebohle, L., Trautmann, T., Skorupa, W., Gauglitz, G., Frank, R.
Fabrication and evaluation of efficient light emitters comprising nanocluster-rich SiO_2 layers
"Photonic Crystal Materials and Nanostructures", R.M. De La Rue, P. Viktorovitch, C.M. Sotomayor Torres, M. Midrio (Eds), Proc. of SPIE **5450** (2004) 578

Zuk, J., Krzyzanowska, H., Clouter, M.J., Bromberek, M., Bubert, H., Rebohle, L., Skorupa, W.
Brillouin scattering and x-ray photoelectron studies of germanium nanoclusters synthesized in SiO_2 by ion implantation
J. Appl. Phys. **96** (2004) 4952

Invited Talks

Brauer, G., Anwand, W., Coleman, P.G., Skorupa, W.
Slow positron annihilation spectroscopy – a tool to characterize vacancy-type damage in ion-implanted 6H-SiC
5th Int. Conf. on Ion Implantation and Other Applications of Ions and Electrons, Kazimierz Dolny, Poland, June 14–17, 2004

Eichhorn, F., Gaca, J., Heera, V., Schell, N., Turos, A., Weishart, H., Wojcik, M.
Structural studies on ion implanted semiconductors using x-ray synchrotron radiation: strain evolution and growthof nanocrystals,
5th Int. Conf. on Ion Implantation and Other Applications of Ions and Electrons, Kazimierz Dolny, Poland, June 14–17, 2004

Fassbender, J.
Application of light ion irradiation on the magnetic properties of exchange bias layers
Sommerschule der EU-RTN Netzwerke "Nexbias" und "Ultraswitch", Biarritz, Frankreich, Sept 13–17, 2004

Fassbender, J.
Ion beams for magnetic thin film applications
14th Int. Conf. on Ion Beam Modification of Materials, Monterey, USA, Sept 5–10, 2004

Fassbender, J.
Optical control of the magnetization on the picosecond timescale
Int. Workshop on "Magneto-optics of magnetic thin films and multilayers", Duisburg, Germany, April 29–30, 2004

Fassbender, J.
Optical control of the magnetization on the picosecond timescale
Academy Colloquium "Ultrafast spin and magnetization dynamics in magnetic nanostructures", Amsterdam, Niederlande, June 15–17, 2004

Gago, R., Jiménez, I., Vinnichenko, M., Neidhardt, J., Hultman, L., Möller, W.
Bonding structure of fullerene-like carbon nitride thin films
9th Int. Conf. on Plasma Surface Engineering, Garmisch-Partenkirchen, Germany, Sept 13–17, 2004

Grenzer, J., Hazra, S., Chini, T.K., Bischoff, L., Sanyal, M.K., Pietsch, U.
X-ray investigation of low-energy ion-beam induced lateral surface nanostructures on semiconductor surfaces
IUMRS Int. Conf. in Asia (IUMRS-ICA-2004), Hsinchu, Taiwan, Nov 16–18, 2004

Heinig, K.-H., Müller, T., Röntzsch, L.
Atomistic simulations of nanofabrication with ion beams
7th Int. Conf. on Computer Simulation of Radiation Effects in Solids, Helsinki, Finland, June 28–July 2, 2004

Heinig, K.-H., Röntzsch, L., Bernas, H.

Ion-irradiation-induced chemical ordering of intermetallic alloys – predictions based on atomistic simulations
14th Int. Conf. on Ion Beam Modification of Materials, Monterey, USA, Sept 5–10, 2004

Heinig, K.-H.
Computer experiments of nanoshaping
Int. Workshop on Ion Beam Shaping of Nanometals, Amsterdam, Netherlands, Dec 17, 2004

Helm, M.
Efficient light emitting devices based on nanoscale silicon
Int. Conf. on Superlattices, Nanostructures, and Nanodevices (ICSNN'04), Cancun, Mexico, July 19–23, 2004

Helm, M.
Intersubband semiconductor light sources: history, status, and future
The Joint 29th Int. Conf. on Infrared and Millimeter Waves/12th Int. Conf. on Terahertz Electronics (IRMMW 2004/THz 2004), Karlsruhe, Germany, Sept 27–Oct 1, 2004

Jäger, H.-U., Belov, A.Y.
Basic processes in deposition and annealing of ta-C films as predicted by molecular-dynamics simulations
5th Specialist Meeting on Amorphous Carbon, ITC-irst Povo-Trento, Italy, Sept 9–10, 2004

Kolitsch, A., Abendroth, B., Gago, R., Fitz, R., Möller, W.
Application of combined low and high energy ion assistance for film formation and stress relaxation of cBN thin films
5th Int. Conf. on Ion Implantation and Other Applications of Ions and Electrons, Kazimierz Dolny, Poland, June 14–17, 2004

Kolitsch, A., Abendroth, B., Gago, R., Fitz, R., Möller, W.
Combined application of multiple ion energies for simultaneous growth and stress relaxation at thin film deposition
8th Europ. Conf. on Accelerators in Applied Research and Technology, Paris, France, Sept 20–24, 2004

Möller, W., Heinig, K.-H., Müller, T., Röntzsch, L., Schmidt, B.
Self-organisation of nanostructures driven by ion irradiation
IWINP, Shanghai, China, March 11–13, 2004

Möller, W.
Fundamentals of ion beam analysis,
Tutorial "Thin Film Diagnostics", EU-RTN "New Fullerene Like Materials", Dresden, Germany, June 3–5, 2004

Möller, W.
Plasma surface interaction and ion bombardment
Tutorial "Fundamentals and Trends in Plasma Processing"
9th Int. Conf.on Plasma Surface Engineering, Garmisch-Partenkirchen, Germany, Sept 11, 2004

Skorupa, W., Sun, J.M., Nazarov, A.N., Osiyuk, I.N., Tjagulskii, I.P., Lysenko, V.S., Rebohle, L., Yankov, R.A., Gebel, T.,
Silicon-based Light Emission: An inverse approach based on a harsh SIMOX problem
NATO Advanced Research Workshop "Science and Technology of Semiconductor-On-Insulator structures and devices operating in a harsh environment", Kyiv, Ukraine, April 25–29, 2004

Skorupa, W., Panknin, D., Voelskow, M., Anwand, W., Gebel, T., Yankov, R.A.
Advanced thermal processing of materials in the msec range
5th Int. Conf. on Ion Implantation and Other Applications of Ions and Electrons, Kazimierz Dolny, Poland, June 14–17, 2004

Skorupa, W. and the European FLASiC consortium
Flash lamp processing for SiC-Si Heteroepitaxy
Deutsches SiC-Treffen, Kloster Banz, Germany, July 12–13, 2004

Conference Contributions

Abdul-Kader, A. M., Turos, A., Grambole, D., Jagielski, J., Piatkowska, A., Madi, N. K., Al-Maadeed, M.
Compositional transformations in ion implanted polymers
8th Europ. Conf. on Accelerators in Applied Research and Technology, Paris, France, Sept 20–24, 2004

Abendroth, B., Gago, R., Eichhorn, F., Kolitsch, A., Möller, W.
Ion-induced stress relaxation during magnetron sputtering deposition of cubic boron nitride thin films
9th Int. Conf. on Plasma Surface Engineering, Garmisch-Partenkirchen, Germany, Sept 13–17, 2004

Abrasonis, G., Gago, R., Vinnichenko, M., Mücklich, A., Kreißig, U., Kolitsch, A., Möller, W.
On the synthesis of fullerene-like CN_x by IBAD: role of film-forming species, ion bombardment and film growth rate
9th Int. Conf. on Plasma Surface Engineering, Garmisch-Partenkirchen, Germany, Sept 13–17, 2004

Anwand, W., Brauer, G., Skorupa, W.
Defect profiling with positrons – recent results on ion implanted 6H-SiC
Frühjahrstagung des Arbeitskreises "Herstellung und Charakterisierung von massiven GaAs-, InP- und SiC-Kristallen" der Deutschen Gesellschaft für Kristallwachstum und Kristallzüchtung (DGKK), Halle (Saale), Germany, March 31–April 1, 2004

Anwand, W.
The prototype of the new flash lamp apparatus: experiences, results, comparison old and new equipment
EU-Projekttreffen FLASiC, Ilmenau, Germany, Oct 15, 2004

Ayache, R., Bouabellou, A., Richter, E.
Optical characterization of β-$FeSi_2$ layers formed by ion beam synthesis
E-MRS Spring Meeting, Strasbourg, France, May 24–28, 2004

Ayache, R., Bouabellou, A., Richter, E.
Structural and optical properties of ß-$FeSi_2$ phases prepared by ion beam synthesis
E-MRS Fall Meeting, Warsaw, Poland, Sept 6–10, 2004

Beckers, M., Schell, N., Martins, R.M.S., Möller, W.
In-situ x-ray diffraction during sputter deposition of $Ti_{1-x}Al_xN$ thin films
9th Int. Conf. on Plasma Surface Engineering, Garmisch-Partenkirchen, Germany, Sept 13–17, 2004

Beckers, M., Schell, N., Martins, R.M.S., Möller, W.
Growth of sputter-deposited $Ti_{1-x}Al_xN$ investigated by in-situ x-ray diffraction
Rective sputter processes and related phenomena III,
Symp. of the Belgium and Dutch Vacuum Society, Gent, Belgium, Dec 9–10, 2004

Belov, A.Y., Jäger, H.-U.
Formation and evolution of sp^2 clusters in amorphous carbon networks as predicted by molecular dynamics annealing simulations
15th Europ. Conf. on Diamond, Diamond-Like Materials, Carbon Nanotubes, Nitrides & Silicon Carbide, Riva Del Garda, Trentino, Italy, Sept 12–17, 2004

Belov, A.Y., Jäger, H.-U.
Relaxation kinetics in amorphous carbon films: an insight from atomic scale simulation
E-MRS Spring Meeting, Strasbourg, France, May 24–28, 2004

Bernas, H., Chappert, C., Devolder, T., Ravelosona, D., Ferre, J., Jamet, J.P., Chen, Y., Samson, Y., Marty, A., Halley, D., Attane, J., Heinig, K.-H., Strobel, M., Kaitasov, O., Gautrot, S.
Manipulating magnetic nanostructures by ion irradiation: patterning and ordering,
IWINP, Shanghai, China, March 11–13, 2004

Bernas, H., Chappert, C., Devolder, T., Ravelosona, D., Mathet, V., Ferre, J., Jamet, J.P., Mougin, A., Bauer, M., Repain, V., Samson, Y., Marty, A., Halley, D., Attane, J., Heinig, K.-H., Stamps, R., Chen, Y., Suzuki, Y., Kaitasov, O., Ruault, M.-O., Gautrot, S.
Tailoring magnetic nanostructures by ion irradiation,
14th Int. Conf. on Ion Beam Modification of Materials, Monterey, USA, Sept 5–10, 2004

Bilyalov, R., Ulyashin, A., Scherff, M., Grambole, D., Nieuwenhuysen, K. van, Beaucarne, G., Poortmans, J.
Porous Silicon as an intermediate layer for heterojunction solar cells on p-type crystalline substrates
19th Europ. Photovoltaic Solar Energy Conference, Paris, France, June 7–11, 2004

Bischoff, L., Seidel, J., Grafström, S., Eng, L.M.
Surface plasmon interaction with single grooves in thin silver films
E-MRS Spring Meeting, Strasbourg, France, May 24–28, 2004

Bischoff, L., Schmidt, B., Akhmadaliev, C., Röntzsch, L.
$CoSi_2$ nano wires synthesized by FIB processing
Europ. Focused Ion Beam Users Group Annual Meeting, Zürich, Swizerland, Oct 4, 2004

Bischoff, L., Pilz, W., Ganetsos, Th., Akhmadaliev, C., Aidinis, C.J., Londos, C.A.
On the temperature dependence of the mass spectra of AuGe and AuGeSi liquid metal alloy ion sources
2nd Conf. on Microelectronics Microsystems and Nanotechnology, Athens, Greece, Nov 14–17, 2004

Blomeier, S., Fassbender, J., Hillebrands, B., McGrouther, D., McVitie, S., Chapman, J.N.
Strukturelle Untersuchung ionenbestrahlter Austausch-Verschiebungsschichtsysteme
DPG Frühjahrstagung, Regensburg, Germany, March 8–12, 2004

Blomeier, S., Fassbender, J., Hillebrands, B., McGrouther, D., Neill, R.O., McVitie, S., Chapman, J.N.
Modifikation der magnetischen Eigenschaften Austausch-Gekoppelter NiFe/FeMn Filme durch Beschuss mit Ga^+-Ionen
DPG Frühjahrstagung, Regensburg, Germany, March 8–12, 2004

Blomeier, S., McGrouther, D., Neill, R.O., McVitie, S., Chapman, J.N., Weber, M.C., Hillebrands, B., Fassbender, J.
Modification of the magnetic properties of exchange coupled NiFe/FeMn films by Ga^+ ion irradiation
JEMS'04, Dresden, Germany, Sept 6–10, 2004

Bohne, Y., Shevchenko, N., Prokert, F., Borany, J. von, Rauschenbach, B., Möller, W.

In-situ Charakterisierung während der Hochenergie - Sauerstoffionen - Implantation in Übergangsmetalle
DPG Frühjahrstagung, Regensburg, Germany, March 8–12, 2004

Bohne, Y., Shevchenko, N., Prokert, F., Borany, J. von, Rauschenbach, B., Möller, W.
In situ characterization of phase formation during high-energy oxygen ion implantation in molybdenum
8th Europ. Conf. on Accelerators in Applied Research and Technology, Paris, France, Sept 20–24, 2004

Bonafos, C., Cherkashin, N., Carrada, M., Coffin, H., Ben Assayag, G., Schamm, S., Dimitrakis, P., Normand, P., Perego, M., Fanciulli, M., Müller, T., Heinig, K.-H., Argawal, A, Claverie, A.
Manipulation of 2D arrays of Si nanocrystals by ultra-low-energy ion beam-synthesis for nonvolatile memories applications
MRS Fall Meeting, Boston, USA, Nov 29–Dec 3, 2004

Borany, J. von, Friedrich, M., Rüb, M., Deboy, G., Butschke, J., Letzkus, F.
Application of ultra-high energy boron implantation for superjunction power (CoolMOS) devices
15th Int. Conf. on Ion Implantation Technology, Taipeh, China, Oct 24–29, 2004

Brauer, G., Brandstetter, S., Teichert, C., Anwand, W., Skorupa, W.
AFM characterization of 6H-SiC surfaces after ion implantation and annealing
18th Int. Conf. on the Application of Accelerators in Research and Industry, Ft. Worth/TX, USA, Oct 10–15, 2004

Brauer, G.
Depth profiling of defects using a slow positron beam
35th Polish Seminar on Positron Annihilation, Turawa, Poland, Sept 20–24, 2004

Braz Fernandes, F.M., Paula, A.S., Canejo, J., Mahesh, K.K., Silva, R.J.C., Martins, R.M.S., Cardoso, A.M.A., Schell,N.
Texture evolution during annealing of Ni-Ti shape memory alloy
Shape Memory and Superelastic Technology SMST-Europe, Baden-Baden, Germany, Oct 3–7, 2004

Burchard, B., Meijer, J., Rangelow, I.W., Bischoff, L.
Nm scale resolution single ion implantation into diamond for quantum dot production
15th Europ. Conf. on Diamond, Diamond-Like Materials, Carbon Nanotubes, Nitrides & Silicon Carbide, Riva Del Garda, Trentino, Italy, Sept 12–17, 2004

Camero, M., Gago, R., Gómez-Aleixandre, C., Albella, J.M.
Bonding environment in films deposited from Ar/CH_4 and Ar/CH_4/N_2 ECR discharge: effect of voltage *polarization on the growth process*
9th Int. Conf. on Plasma Surface Engineering, Garmisch-Partenkirchen, Germany, Sept 13–17, 2004

Cantelli, V., Borany, J. von, Mücklich, A., Schell, N.
Investigation of the formation and phase transition of small Ge and Co nanoparticles embedded in a dielectric matrix
4th Int. Conf. on Synchrotron Radiation in Materials Science, Grenoble, France, Aug 23–25, 2004

Cantelli, V., Rogozin, A., Shevchenko, N., Vinnichenko, M., Prokert, F., Kolitsch, A., Möller, W.
Annealing of ITO films: in situ studies of structure and resistance
ESRF Science Days, Aussois, France, May 26–28, 2004

Casiraghi, C., Piazza, F., Ferrari, A.C., Grambole, D., Robertson, J.
Deriving properties of hydrogenated amorphous carbon by raman alone

15th Europ. Conf. on Diamond, Diamond-Like Materials, Carbon Nanotubes, Nitrides & Silicon Carbide, Riva Del Garda, Trentino, Italy, Sept 12–17, 2004

Chen, X.D., Ling, C.C., Fung, S., Beling, C.D., Wu, H.S., Brauer, G., Anwand, W., Skorupa, W.
Deep level defects in He-implanted n-6H-SiC studied by deep level transient spectroscopy
MRS Spring Meeting, San Francisco/CA, USA, April 12–16, 2004

Cheng, X.Q., Sun, J.M., Kögler, R., Skorupa, W., Möller, W., Prucnal, S., Zuk, J.
Photoluminescence of Er doped SiO_2 films embedded Si nanoclusters using dual implantation chamber and annealing
5th Int. Conf. on Ion Implantation and Other Applications of Ions and Electrons, Kazimierz Dolny, Poland, June 14–17, 2004

Cizek, J., Prochazka, I., Smola, B., Stulikova, I., Kuzel, R., Cieslar, M., Matej, Z., Cherkaska, V., Brauer, G., Anwand, W., Islamgaliev, R.K., Kulyasova, O.
Positron annihilation studies of microstructure of ultra fine grained metals prepared by severe plastic deformation
4th Int. Conf. on Materials Structure and Micromechanics of Fracture, Brno, Czech Republic, June 23–25, 2004

Cizek, J., Prochazka, I., Kuzel, R., Becvar, F., Cieslar, M., Brauer, G., Anwand, W., Kirchheim, R., Pundt, A.
Hydrogen-induced defects in niobium studied by positron annihilation spectroscopy
Int. Symp.on Metal-Hydrogen Systems, Fundamentals and Applications, Cracow, Poland, Sept 5 – 10, 2004

Cizek, J., Prochazka, I., Kuzel, R., Matej, Z., Cherkaska, V., Cieslar, M., Smola, B., Stulikova, I., Brauer, G., Anwand, W., Islamgaliev, R.K., Kulyasova, O.
Positron annihilation spectroscopy of ultra fine-grained metals prepared by severe plastic deformation
35th Polish Seminar on Positron Annihilation, Turawa, Poland, Sept 20–24, 2004

Constantinescu, B., Bugoi, R., Cojocaru, V., Voiculescu, D., Grambole, D., Herrmann, F., Ceccato, D.
Romanian ancient gold objects provenance studies using micro-beam methods: the case of Pietroasa hoard
9th Int. Conf. on Nuclear Microprobe Technology and Applications, Cavtat, Dubrovnik, Croatia Sept 13–17, 2004

Dagkaldiran, Ü., Grambole, D., Herrmann, F., Schreiber, H.-U., Meijer, J.
Microchanneling investigation of ß-$FeSi_2$-structures
9th Int. Conf. on Nuclear Microprobe Technology and Applications, Cavtat, Dubrovnik, Croatia Sept 13–17, 2004

Dimitrakis, P., Normand, P., Vontintseva, E., Stegemann, K.-H., Heinig, K.-H., Schmidt, B.
Memory devices obtained by Si^+ irradiation through poly-Si/SiO_2 gate stack
2nd Conf. on Microsystems, Microelectronics and Nanotechnology, Athene, Greece, Nov 11–17, 2004

Dmitrieva, O., Acet, M., Liedke, M.O., Rellinghaus, B., Fassbender, J.
He ion irradiation induced phase transformation of icosahedral FePt nanoparticles
Conf. on Magnetism and Magnetic Materials, Jacksonville, USA, Nov 7–11, 2004

Dollinger, G., Neumaier, P., Bergmaier, A., Eckstein, W., Fischer, R., Hofsaess, H., Kroeger, H., Ronning, C., Jäger, H.-U.
Range and mixing distributions of low-energy carbon ions as a base for subplantation growth models
EMRS Spring Meeting, Strasbourg, France, May 24–28, 2004

Dekorsy, T., Helm, M., Yakovlev, V., Seidel, W., Keilmann, F.
Far-IR spectroscopy of the nonlinear susceptibility of GaAs with an FEL
Int. Conf. on Low Energy Electrodynamics in Solids, Kloster Banz, Germany, July 19–23, 2004

Dekorsy T., Sun, J.M., Skorupa, W., Mücklich, A., Schmidt, B., Helm, M.
Origin of efficient light emission from Si pn diodes prepared by ion implantation
27th Int. Conf. on the Physics of Semiconductors, Flagstaff, AZ, USA, July 25–30, 2004

Dreyhaupt, A., Winnerl, S., Dekorsy, T., Helm, M.
Time-domain THz spectroscopy of electronic excitations in GaAs/AlGaAs superlattices
DPG Frühjahrstagung, Regensburg, Germany, March 8–12, 2004

Eichhorn, F., Fromknecht, R.
Structural studies of epitaxial Au nanocrystals in rutile
7th Biennial Conf. on High Resolution X-Ray Diffraction and Imaging, Prague, Czech Republic, Sept 7–10, 2004

Facsko, S., Pesic, Z., Hellhammer, R., Stolterfoht, N., Kost, D., Möller, W.
Electron emission from Ne^{9+} *interacting with thin* SiO_2 *films*
24th Werner-Brandt Workshop, Berlin, Germany, July 12–14, 2004

Facsko, S., Kost, D., Möller, W., Zschornack, G., Hellhammer, R., Stolterfoht, R.
Potential energy retention of highly charged ions in solid surfaces
12th Int. Conf. on the Physics of Highly Charged Ions, Vilnius, Lithuania, Sept 6–11, 2004

Ferrari, A.C., Reich, S., Casiraghi, C., Arenal de la Concha, R., Loiseau, A., Gago, R., Abendroth, B., Bello, I., Robertson, J.
UV raman spectroscopy of boron nitrides
15th Europ. Conf. on Diamond, Diamond-Like Materials, Carbon Nanotubes, Nitrides & Silicon Carbide, Riva Del Garda, Trentino, Italy, Sept 12–17, 2004

Ferro, G., Panknin, P., Polychroniadis, E.K., Monteil, Y., Skorupa, W., Stoemenos, J.
Microstructural characterization of 3C-SiC thin films epitaxially formed by the flash lamp process (FLASIC)
5th Europ. Conf. Silicon Carbide and Related Materials, Bologna, Italy, Aug 31–Sept 4, 2004

Friedrich, M., Tyrroff, H.
Long-time operation of a modified Cs sputter ion source 860-C
38th Symp. of Northeastern Accelerator Personnel, Hamilton/Ontario, Canada, Oct 17–21,2004

Gago, R., Vinnichenko, M., Kreißig, U., Czigany, Z., Kolitsch, A., Möller, W.
Growth of carbon nitride thin films by low-energy ion beam assisted evaporation: on the production of fullerene-like microstructure
Int. Conf. on Metallurgical Thin Films and Coatings, San Diego, CA, USA April 9–23, 2004

Ganetsos, T., Mair, A.W.R., Mair, G.L.R., Bischoff, L., Akhmadaliev, C., Aidinis, C.J.,
Can direct field-evaporation of doubly-charged ions and post-ionisation from singly-charged state coexist?
49th Int. Field Emission Symposium, Seggau Castle, Graz, Austria, July 12–15, 2004

Gebel, T., Rebohle, L., Yankov, R.A., Skorupa, W., Gauglitz, G., Frank, R.
Microarrays of miniaturized silicon-based light sources: fabrication and use
Statusseminar "Chiptechnologien, Mikroarrays, Hygiene und Gesundheit", DECHEMA, Frankfurt/M., Germany, Jan 26–27, 2004

Gomes, G.F., Ueda, M., Beloto, A.F., Reuther, H., Richter, E.
Chromium enrichment of AISI 304 stainless steel surface after nitrogen ion recoil bombardment of chromium film
8th Europ. Conf. on Accelerators in Applied Research and Technology, Paris, France,
Sept 20–24, 2004

Grambole, D., Herrmann, F., Dagkaldiran, Ü., Meijer, J.
Micro RBS-channeling measurements to study damage accumulation in silicon by ion implantation
9th Int. Conf. on Nuclear Microprobe Technology and Applications, Cavtat, Dubrovnik, Croatia,
Sept 13–17, 2004

Grenzer, J., Bischoff, L., Pietsch, U.
X-ray grazing incidence diffraction: A tool to optimize focused ion beam implantation
7th Biennial Conf. on High Resolution X–Ray Diffraction and Imaging, Prague, Czech Republic,
Sept 7–10, 2004

Grynszpan, R.I., Fradin, J., Saude, S., Thome, L., Anwand, W., Brauer, G.
Investigation of defects induced by ion implantation of noble gases in yttria-stabilized zirconia
18th Int. Conf. on the application of accelerators in research and industry, Ft. Worth/TX, USA,
Oct 10–15, 2004

Hoffmann, V., Huebner, R., Hecker, M., Baunack, S., Mattern, K., Wetzig, K., Grötzschel, R.
Investigation of ultra-thin layers by RF-GD-OES
2004 Winter Conference on Plasma Spectrochemistry, Fort Lauderdale, USA, Jan 5–10, 2004

Jäger, H.-U., Belov, A.Y., Gago, R., Vinnichenko, M., Jiménez, I., Huang, N., Leng, Y.X., Sun, H., Maitz, M.F.
Evolution of sp^2 networks with substrate temperate in amorphous carbon films: theory and experiment
15th Europ. Conf. on Diamond, Diamond-Like Materials, Carbon Nanotubes, Nitrides & Silicon Carbide, Riva Del Garda, Trentino, Italy, Sept 12–17, 2004

Kögler, R., Eichhorn, F., Peeva, A., Voelskow, M., Mücklich, A., Serre, C., Skorupa, W.
Effects of ion beam induced excess vacancies in silicon: analysis, modelling, application,
5th Int. Conf. on Ion Implantation and Other Applications of Ions and Electrons, Kazimierz Dolny, Poland, June 14–17, 2004

Kost, D., Facsko, S., Möller, W.
Potential energy retention of slow highly charged Ar-ions in chemical clean silicon surfaces
DPG-Frühjahrstagung, Regensburg, Germany, March 8–12, 2004

Krause-Rehberg, R., Sachert, S., Brauer, G., Rogov, A., Noack, K., Michel, P.
Design of a mono-energetic positron source for positron lifetime measurements at the radiation source ELBE
18th Int. Conf. on the Application of Accelerators in Research and Industry, Ft. Worth/TX, USA,
Oct 10–15, 2004

Krause-Rehberg, R., Brauer, G., Sachert, S., Bondarenko, V., Rogov, A, Noack, K.
EPOS – an intense positron beam project at the Research Center Rossendorf
Int. Symp. on Positron Beam and its Application, Wuhan, China, Oct 29–30, 2004

Krecar, D., Fuchs, M., Kögler, R., Hutter, H.
Investigation of gettering effects in CZ-type Silicon with SIMS
13. Arbeitstagung Angewandte Oberflächenanalytik, Dresden, Germany, Sept 14–17, 2004

Liedke, M.O., Nembach, H., Fassbender, J., Hillebrands, B.

Investigation of the Fe19Ni81/Fe50Mn50 exchange bias system with varying Cu spacer layer for partial decoupling
DPG Frühjahrstagung, Regensburg, Germany, March 8–12, 2004

Liedke, M.O., Nembach, H., Hillebrands, B., Fassbender, J.
Analysis of the NiFe/FeMn exchange bias system with a varying Cu spacer thickness and position for partial decoupling
JEMS'04, Dresden, Germany, Sept 6–10, 2004

Liedke, M.O., Nembach, H., Hillebrands, B., Fassbender, J.
Investigation of the $Fe_{19}Ni_{81}/Fe_{50}Mn_{50}$ exchange bias system with varying Cu spacer layer for partial decoupling
Int. Workshop on Exchange Bias in Magnetic Nanostructures, Biarritz, France, Sept 16–18, 2004

Ling, C.C., Cheng, X.D., Fung, S., Beling, C.D., Brauer, G., Anwand, W., Skorupa, W.
E_1/E_2 an Z_1/Z_2 deep level defects in n-type 6H silicon carbide induced by electron irradiation and He implantation
27th Int. Conf. on the Physics of Semiconductors, Flagstaff/AZ, USA, July 26–30, 2004

Maitz, M.F., Pham, M.T, Shevchenko, N.
Modified NiTi for improved biocompatibility
6th Asian Symp. on Biomedical Materials, Emei City, Chengdu, China, 2004

Maitz, M.F., Fitz, T., Pham, M.T., Richter, E.
Blood compatibility of metal oxide surfaces prepared by metal plasma immersion ion implantation and deposition
7th World Biomaterials Congress, Sydney, Australia, 2004

Martins, R.M.S., Braz Fernandez, F.M., Silva, R.J.C., Beckers, M., Schell, N.
In-situ XRD during sputtering of Shape Memory Alloy (SMA) Ni-Ti thin films
14th ESRF User Meeting, Grenoble France, Feb 10–11, 2004

Martins, R.M.S., Braz Fernandez, F.M., Silva, R.J.C., Schell, N.
In-situ X-ray diffraction during sputtering of Shape Memory Alloy (SMA) Ni-Ti thin films
DPG-Frühjahrstagung, Regensburg, Germany, March 8–12, 2004

Martins, R.M.S., Braz Fernandez, F.M., Silva, R.J.C., Schell, N.
Structural in-situ studies of Shape Memory Alloy (SMA) Ni-Ti thin films
4th Int. Conf. on Synchrotron Radiation in Materials Science, Grenoble, France, Aug 23–25, 2004

Martins, R.M.S., Braz Fernandez, F.M., Silva, R.J.C., Beckers, M., Schell, N.
In-situ studies of Shape Memory Alloy (SMA) Ni-Ti thin films
ESRF Science Days, Aussois, France, May 26–28, 2004

Martins, R.M.S., Braz Fernandez, F.M., Silva, R.J.C., Beckers, M., Schell, N.
In-situ studies of Ni-Ti thin films
Shape Memory and Superelastic Technology SMST-Europe, Baden-Baden, Germany, Oct 3–7, 2004

Mazur, K., Sass, J., Eichhorn, F., Strupinski, W., Turos, A., Kowalik, A.
The (224) asymmetrical reflection from laterally patterned heteroepitaxial InGaAs/GaAs layers
Int. Conf. on Experimental and Computing Methods in High Resolution Diffraction Applied for Structure Characterization of Modern Materials, Zakopane, Poland, June 13–17, 2004

McCord, J., Fassbender, J., Liedke, M.O., Fromberger, M., Quandt, E., Schulz, L.
Anisotropy patterning of amorphous CoFeSiB films by He -ion radiation

Conf. on Magnetism and Magnetic Materials, Jacksonville, USA, Nov 7-11, 2004

Meduňa, M., Novák, J., Falub, C.V., Chen, G., Bauer, G., Tsujino, S., Grützmacher, D., Müller, E., Campidelli, Y., Kermarrec, O., Bensahel, D., Schell, N.
High temperature investigations of Si/Ge based cascade structures using X-ray scattering methods
7th Biennial Conf. on High Resolution X-Ray Diffraction and Imaging, Prague, Czech Republic, Sept 7–10, 2004

Müller, T., Heinig, K.-H., Bonafos, C., Coffin, H., Ben Assayag, G., Schamm, S., Zanchi, G., Claverie, A., Tencé, M., Colliex, C.
Multi-dot floating-gates in MOSFETS for nonvolatile memories – their ion beam synthesis and morphology
DPG Frühjahrstagung, Regensburg, Germany, March 8–12, 2004

Neelmeijer, C., Mäder, M.
Proton beam examination of glass – an analytical contribution for preventive conservation
Benefits of non-destructive analytical techniques for conservation
Int. Workshop COST-G8, Bighi/Kalkara, Malta, Jan 8, 2004

Nembach, H., Weber, M., Fassbender, J., Hillebrands, B.
Damping in thin NiFe films
DPG Frühjahrstagung, Regensburg, Germany, March 8–12, 2004

Oates, T.W.H, Ryves, L. Bilek, M.M.M., McKenzie, D.R.
Optical and electronic properties of ultrathin silver films for biosensor applications
EMRS Fall Meeting, Warsaw, Poland, Sept 6–10, 2004

Oates, T.W.H.
Electrical resistance of ultrathin films determined by in situ spectroscopic ellipsometry
5th Int. Young Scientists Conference, Kyiv, Ukraine, Oct 28–31, 2004

Olk, P., Seidel, J., Grafström, S., Eng L.M., Baida, F., Van Labeke, D., Ott, M., Bischoff, L.
Surface plasmon propagation in metallic nanostructures
DPG Frühjahrstagung, Regensburg, Germany, March 8–12, 2004

Paula, A.S., Canejo, J.P.H.G., Schell, N., Braz Fernandes, F.M.
Structural evolution on thermal cycling in Ti-rich NiTi SMA
4th Int. Conf. on Synchrotron Radiation in Materials Science (SRMS-4), Grenoble, France, Aug 23–25, 2004

Peeva, A.
Detailed profiling of ion implantation induced excess vacancies in silicon
Arbeitstreffen "Punktdefekte" TU Dresden, Germany, April 1–2, 2004

Peeva, A., Kalitzova, M., Zollo, G., Beshkov, G., Vitali, G., Skorupa, W.
Ion beam assisted Ge nanocrystallization in Ta_2O_5 films
13th Int. School on Condensed Matter Physics, Varna, Bulgaria, Aug 30–Sep 3, 2004

Perego, M., Ferrari, S., Fanciulli, M., Soncini, V., Mathiot, D., Heinig, K.-H., Müller, T., Schmidt, B., Normand, P., Dimitrakis, P., Kapetanakis, E., Ben Assayag, G., Bonafos, C., Carrada, M., Claverie, A.
2D-arrays of Si nanocrystals embedded in thin SiO_2 layers for new memory devices
Silicon Workshop, Genova, Italy, Feb 11, 2004
INFM Workshop, Genova, Italy, June, 2004

Pezoldt, J., Polychroniadis, E.K., Stauden, Th., Ecke, G., Chassagne, T., Vennegues, P., Leycuras, A., Panknin, D., Stoemenos, J., Skorupa, W.
Nucleation control in FLASiC assisted short time liquid phase epitaxy by melt modification
5th Europ. Conf. Silicon Carbide and Related Materials, Bologna, Italy, Aug.31-Sept.4, 2004

Piazza, F., Grambole, D., Schneider, D., Casiraghi, C., Ferrari, A.C., Robertson, J.
Protective diamond-like carbon coatings for future optical storage disks
15th Europ. Conf. on Diamond, Diamond-Like Materials, Carbon Nanotubes, Nitrides & Silicon Carbide, Riva Del Garda, Trentino, Italy, Sept 12–17, 2004

Pilz, W., Bischoff, L., Mair, G.L.R., Akhmadaliev, C., Aidinis, C.J., Ganetsos, Th.
The temperature dependence of energy spread and mass spectra of an $Au_{73}Ge_{27}$ alloy liquid metal ion source
49th Int. Field Emission Symposium, Seggau Castle, Graz, Austria, July 12–15, 2004

Podsiado, S., Strojek, B., Strzakowski, I., Turos, A., Abdul-Kader, A.M., Grambole, D.
Hydrogen behaviour in novel materials for spintronic: GaFeN codoped with Mg, Si and Al
5th Int. Conf. on Ion Implantation and Other Applications of Ions and Electrons, Kazimierz Dolny, Poland, June 14–17, 2004

Posselt, M.
Classical MD study on the the mobility of di- and tri-interstitials
MRS 2004 Spring Meeting, San Francisco, USA, April 12–16, 2004

Posselt, M., Gao, F., Weber, W.J.
Antisite pair recombination in cubic SiC by a concerted exchange mechanism
14th Int. Conf. on Ion Beam Modification of Materials, Monterey, USA, Sept 5-10, 2004

Posselt, M., Gao, F., Zwicker, D.
Migration of di- and tri-interstitials in silicon
7th Int. Conf. on Computer Simulation of Radiation Effects in Solids, Helsinki, Finland, June 28–July 2, 2004

Posselt, M., Mäder, M., Lebedev, A., Grötzschel, R.
Multiple implantations - experiments and computer simulations
MRS 2004 Spring Meeting, San Francisco, USA, April 12–16, 2004

Prucnal, S., Cheng, X.Q., Sun, J.M., Kögler, R., Zuk, J., Skorupa, W.
Optical and microstructural properties of doubly implanted SiO_2 layers using combined Ge-Si implantation
5th Int. Conf. on Ion Implantation and Other Applications of Ions and Electrons, Kazimierz Dolny, Poland, June 14–17, 2004

Rangelow, I.W., Ivanova, K., Ivanov, T., Meijer, J., Burchard, B., Park, S.J., Persaud, A., Schenkel, T., Bischoff; L.
Concept of an ion implantation stage with atomic resolution
9th Int. Conf. on Nuclear Microprobe Technology and Applications, Cavtat, Dubrovnik, Croatia, Sept 13–17, 2004

Reuther, H.
Chrombeschichtung von Baustahl mittels Ionenstrahlbehandlung
Mößbauerkolloquium Dresden 2004, FZ Rossendorf, Dresden, Germany, Sept 30–Oct 1, 2004

Reuther, H., Menzel, M., Vinnichenko, M., Kolitsch, A.

Sn^{4+} charge density variation in In_2O_3
Int. Symp. on the Industrial Applications of the Mössbauer Effect, Madrid, Spain, Oct 4–9, 2004

Reuther, H., Richter, E., Prokert, F., Ueda, M., Beloto, A.F., Gomes, G.F.
Chrombeschichtung von Baustahl mittels Ionenstrahlbehandlung
13. Arbeitstagung Angewandte Oberflächenanalytik, Dresden, Germany, Sept 14–17, 2004

Röntzsch, L., Heinig, K.-H., Schmidt, B.
Experimental evidence of Si nanocluster delta-layer formation in buried and thin SiO_2 films induced by ion irradiation
E-MRS Spring Meeting, Strasbourg, France, May 26, 2004

Röntzsch, L., Heinig, K.-H., Schmidt, B., Mücklich, A.
Experimental evidence of Si nanocluster delta-layer formation in the vicinity of ion-irradiated SiO_2-Si interfaces
14th Int. Conf. on Beam Modification of Materials, Monterey, USA, Sept 5–10, 2004

Röntzsch, L., Heinig, K.-H., Schmidt, B.
Evidence of self-aligned Si nanocluster delta-layers in buried SiO_2 films induced by ion irradiation
EURESCO Conf. on Cluster Systems and Nanotubes, Giens, France, May 8–12, 2004

Röntzsch, L., Heinig, K.-H., Schmidt, B.
Evidence of self-aligned Si nanocluster delta-layers in buried SiO_2 films induced by ion irradiation
Int. School on Radiation Effects in Solids, NATO and the Ettore Majorana Centre, Erice, Italy, July 17–29, 2004

Röntzsch, L., Heinig, K.-H., Schmidt, B.
Self-organization of nanocluster delta-layers at ion-beam mixed Si-SiO_2 interfaces
DPG Frühjahrstagung, Regensburg, Germany, March 8–12, 2004

Sass, J., Mazur, K., Eichhorn, F., Strupinski, W., Turos, A.
Determination of In concentration in InGaAs/ GaAs epilayers in the early stage of anisotropic stress relaxatio
Int. Conf. on Experimental and Computing Methods in High Resolution Diffraction Applied for Structure Characterization of Modern Materials, Zakopane, Poland, June 13–17, 2004

Schmidt, B., Heinig, K.-H., Röntzsch, L., Müller, T., Stegemann, K.-H., Votintseva, E.
Ion irradiation through SiO_2/Si-interfaces: non-conventional fabrication of Si nanocrystals for memory applications
14th Int. Conf. on Beam Modification of Materials, Monterey, USA, Sept 5–10, 2004

Seidel, J., Grafström, S., Bischoff, L., Eng, L.W.
Surface plasmon propagation in structured metal films
Int. Workshop and Seminar on Cooperative Phenomena in Optics and Transport in Nanostructures, Dresden, Germany, June 10–20, 2004

Semtsiv, M.P., Ziegler, M., Dressler, S., Masselink, W.T., Georgiev, N., Dekorsy, T., Helm, M.
Design and operation of strain-compensated InGaAs/AlAs/InP quantum cascade lasers emitting at 3.7-4.2 micrometer
6th Int. Conf. on Mid-Infrared Optoelectronics Materials and Devices, St. Petersburg, Russia, June 27–July 2, 2004

Semtsiv, M.P., Ziegler, M., Dressler, S., Masselink, W.T., Georgiev, N., Dekorsy, T., Helm, M.
Strain-compensated AlAs/(In,Ga)As heterostructures for short wavelength intersubband absorption and laser emission

Int. Conf. on Molecular Beam Epitaxy, Edinburgh, UK, Aug 22–27, 2004

Shevchenko, N., Maitz, M.F.
Ni depletion of a NiTi surface by ion implantation for biomedical applications
DPG Frühjahrstagung, Regensburg, Germany, March 8–12, 2004

Shevchenko, N., Pham, M.T., Richter, E., Maitz, M.F.
Ion implantation of NiTi alloy: surface processes and properties
7t[h] Int. Conf. on Modification of Materials with Particle Beams and Plasma Flows, Tomsk, Russia, July 25–30, 2004

Shevchenko, N., Pham, M.T., Richter, E., Maitz, M.F.
Ion implanted NiTi surfaces for biomedical applications
16th Int. Vacuum Congress IVC-16/ ICSS-12/ NANO-8, Venice, Italy, June 28–July 2, 2004

Shevchenko, N., Pham, M.T., Richter, E., Maitz, M.F.
Surface processes and properties of ion implanted NiTi alloy
9th Int. Conf. on Plasma Surface Engineering, Garmisch-Partenkirchen, Germany, Sept 13–17, 2004

Shevchenko, N., Rogozin, A., Schell, N., Cantelli, V., Vinnichenko, M., Prokert, F., Kolitsch, A.
In-situ investigations of the amorphous-to-crystalline transformation of ITO films by synchrotron X-ray scattering
Conf. on Synchrotron Radiation in Materials Science, France, Aug 23–25, 2004

Shevchenko, N., Rogozin, A., Vinnichenko, M., Prokert, F., Cantelli, V., Kolitsch, A., Möller, W.
In situ monitoring of the ITO film structure and properties during annealing
16th Int. Vacuum Congress IVC-16/ ICSS-12/ NANO-8, Venice, Italy, June 28–July 2, 2004

Sinning, S., Dekorsy, T., Helm, M.
Ladungsträger-Dynamik in Stickstoff-implantiertem GaAs
DPG Frühjahrstagung, Regensburg, Germany, March 8–12, 2004

Sinning, S., Dekorsy, T., Helm, M., Mussler, G., Daweritz, L., Ploog, K.H.
Ultrafast carrier dynamics in nitrogen containing GaAs
EMRS 2004 Spring Meeting, Strasbourg, France, May 24–28, 2004
27th Int. Conf. on the Physics of Semiconductors, Flagstaff, Arizona, USA, July 25–30, 2004

Skorupa, W., Panknin, D., Voelskow, M., Anwand, W., Gebel, T., Yankov, R.A.
Advanced Thermal Processing of Semiconducting Materials Using Flash Lamp Annealing
MRS Spring Meeting, San Francisco, USA, April 13–16, 2004

Skorupa, W., Yankov, R.A., Anwand, W., Voelskow, M., Gebel, T., Downey, D.F., Arevalo, E.A.
Ultra-shallow junctions produced by plasma doping and flash lamp annealing
EMRS Spring Meeting, Strasbourg, France, May 24–28, 2004

Smith, M., McMahon, R.A., Voelskow, M., Skorupa, W., Stoemenos, J.
Thermal model for flashlamp annealing of 3C-SiC/Si multilayer systems (i-FLASiC)
5th Europ. Conf. Silicon Carbide and Related Materials, Bologna, Italy, Aug 31–Sept 4, 2004

Solina, D., Liedke, M.O., Tietze, U., Fassbender, J., Schreyer, A.
Reflectivity characterization of ion irradiated exchange bias FeMn-FeNi films
MML'04, Boulder, USA, June 7–11, 2004

Solina, D., Liedke, M.O., Tietze, U., Fassbender, J., Schreyer, A.
Structure and interface characterisation of Exchange Bias FeMn-FeNi films

DPG Frühjahrstagung, Regensburg, Germany, March 8–12, 2004

Strivay, D., Ramboz, C., Sauvage, T., Gallien, J.-P., Grambole, D.
Estimating the depth of the roof and floor of intra-crystalline inclusions in a light-mineral matrix: application of RBS spectrometry
9th Int. Conf. on Nuclear Microprobe Technology and Applications, Cavtat, Dubrovnik, Croatia Sept 13–17, 2004

Sun, J.M., Dekorsy, T., Skorupa, W., Schmidt, B., Helm, M.
Temperature dependence of efficient silicon light-emitting diodes prepared by ion implantation
DPG Frühjahrstagung, Regensburg, Germany, March 8–12, 2004

Sun, J.M., Dekorsy, T., Skorupa, W., Schmidt, B., Mücklich, A., Helm, M.
Efficient silicon light emitting diodes by boron implantation: the mechanism
EMRS Spring Meeting, Strasbourg, France, May 24–28, 2004

Sun, J. M., Dekorsy, T., Skorupa, W., Schmidt, B., Mücklich, A., Helm, M.
The mechanism in efficient silicon light-emitting diodes
5th Int. Conf. on Ion Implantation and Other Applications of Ions and Electrons, Kazimierz Dolny, Poland, June 14–17, 2004

Tsvetkova, T., Takahashi, S., Zayats, A., Dawson, P., Turner, R., Bischoff, L., Angelov, O., Dimora-Malinovska, D.
Focused ion beam writing of optical pattern
5th Int. Conf. on Ion Implantation and Other Applications of Ions and Electrons, Kazimierz Dolny, Poland, June 14–17, 2004

Tsyganov, I., Maitz, M.F., Wieser, E., Richter, E., Reuther, H.
Structure and properties of titanium based coatings prepared by metal plasma immersion ion implantation and deposition
9th Int. Conf. on Plasma Surface Engineering, Garmisch-Partenkirchen, Germany, Sept 13–17, 2004

Tsyganov, I., Maitz, M.F., Richter, E.
Titanium-based layers prepared by metal plasma immersion ion implantation and deposition as hemocompatible surfaces
5th Int. Young Scientists Conf. on Problems of Optics and High Technology Material Science, Kyiv, Ukraine, Oct 28–31, 2004

Ueda, M., Berni, L.A., Castro, R.M., Reuther, H., Lepienski, C.M., Soares Jr., P.C.
Improvements of tribological properties of CrNiMo and CrCoMo alloys by nitrogen plasma immersion ion implantation
9th Int. Conf. on Plasma Surface Engineering, Garmisch-Partenkirchen, Germany, Sept 13–17, 2004

Ueda, M., Leandro, C., Reuther, H., Lepienski, C.M.
Plasma immersion ion implantation of nitrogen into H_{13} steel under moderate temperatures
8th Europ. Conf. on Accelerators in Applied Research and Technology, Paris, France, Sept 20–24, 2004

Ueda, M., Reuther, H., Lepienski, C.M.
Comparison of nitrogen ion beam and plasma immersion implantation in $Al_5 0_{52}$ alloy
8th Europ. Conf. on Accelerators in Applied Research and Technology, Paris, France, Sept 20–24, 2004

Ueda, M., Wei, R., Reuther, H.
Plasma immersion ion implantation under industrially relevant conditions

2nd Int. Workshop on Particle Beams & Plasma Interaction on Material/2nd Asia Symp. on Ion & Plasma Surface Finishing, Nov 25, 2004

Vinnichenko, M., Rogozin, A., Shevchenko, N., Kreißig, U., Kolitsch, A., Möller, W.
Spectroscopic ellipsometry characterization of ITO films prepared by reactive mf dual magnetron sputtering: effect of substrate temperature
Int. Conf. on Metallurgical Coatings and Thin Films, San Diego, CA, USA, April 19–24, 2004

Vinnichenko, M., Rogozin, A., Shevchenko, N., Kolitsch, A., Möller, W.
Real-time evolution of indium tin oxide properties during annealing in vacuum studied by in situ spectroscopic ellipsometry
5th Int. Young Scientists Conference, Problems of Optics and High Technology Material Science, Kyiv, Ukraine, Oct 27–31, 2004

Voelskow, M., Panknin, D., Polychroniadis, E.K., Ferro, G., Monteil, Y., Godignion, P., Mestres, N., Skorupa, W., Stoemenos, J.
Epitaxial 3C-SiC formation at the SiO_2/Si interface by C^+ Implantation into SiO_2 and subsequent annealing
5th Europ. Conf. Silicon Carbide and Related Materials, Bologna, Italy, Aug 31–Sept 4, 2004

Weber, M., Nembach, H., Fassbender, J.
Optische Kontrolle der Magnetisierung in austauschgekoppelten NiFe/FeMn Filmen auf der Pikosekundenzeitskala
DPG Frühjahrstagung, Regensburg, Germany, March 8–12, 2004

Weber, M., Nembach, H., Hillebrands, B., Fassbender, J.
All-optical probe of magnetization dynamics in exchange coupled NiFe/FeMn bilayers on the picosecond timescale
Int. Workshop on Exchange Bias in Magnetic Nanostructures, Biarritz, France, Sept 16–18, 2004

Weber, M., Nembach, H., Hillebrands, B., Fassbender, J.
Modified gilbert damping due to exchange bias in NiFe/FeMn bilayers
Conf. on Magnetism and Magnetic Materials, Jacksonville, USA, Nov 7–11, 2004

Weishart, H., Heera, V., Pécz, B., Tóth, L., Skorupa, W.
High-fluence C-implantation into 3C-SiC: synthesis of buried diamond-nanocrystals
DPG Frühjahrstagung, Regensburg, Germany, March 8–12, 2004

Winnerl, S., Dekorsy, T., Helm, M.
THz emission from GaSb samples with modified surface stoichiometry
DPG Frühjahrstagung, Regensburg, Germany, March 8–12, 2004

Winnerl, S., Dreyhaupt, A., Dekorsy, T., Helm, M.
THz-time-domain spectroscopy of doped semiconductor superlattices
Workshop on Quantum Heterostructures and THz Electronics, Regensburg, Germany, 2004

Zolnai, Z., Ster, A., Khanh, N.Q., Kotai, E., Posselt, M., Battistig, G., Lohner, T., Gyulai, J.
Ion beam analysis and computer simulation of damage accumulation in nitrogen implanted 6H-SiC: effects of channeling
5th Europ. Conf. on Silicon Carbide and Related Materials, Bologna, Italy, Aug 31–Sept 4, 2004

Zschornack, G., Landgraf, S., Facsko, S., Kost, D., Möller, W., Tyrroff, H., Großmann, F., Kentsch, U., Ovsyannikov, V.P., Schmidt, M., Ullmann, F.
A new ion beam facility for slow highly charged ions
9th Europ. Particle Accelerator Conference, Lucerne, Switzerland, July 5–9, 2004

Lectures

Bischoff, L.
Alloy liquid metal ion sources and their application in mass separated focused ion beams
Ruhr-Universität Bochum, Graduiertenkolleg, Germany, April 22, 2004

Bischoff, L.
Alloy liquid metal ion sources and their application in mass separated focused ion beams
Universität Tübingen, Institut für Angewandte Physik, Germany, Dec 1, 2004

Brauer, G., Anwand, W., Coleman, P.G., Skorupa, W.
Slow positron implantation spectroscopy – a tool to characterize vacancy-type damage in ion-implanted 6H-SiC
Dept. of Physics, University of Texas at Austin, Austin/TX, USA, Oct 19, 2004

Brauer, G., Anwand, W., Coleman, P.G., Skorupa, W.
Slow positron implantation spectroscopy – a tool to characterize vacancy-type damage in ion-implanted 6H-SiC
Physics Dept., University of Texas at Arlington, Arlington/TX, USA, Oct 21, 2004

Brauer, G., Anwand, W., Coleman, P.G., Skorupa, W.
Slow positron implantation spectroscopy – a tool to characterize vacancy-type damage in ion-implanted 6H-SiC
Dept. of Physics, Texas Christian University, Ft. Worth/TX, USA, Oct 22, 2004

Dekorsy, T.
Femtosekunden Spektroskopie an Quantenstrukturen
Universität Konstanz, Physikalisches Kolloquium, Germany, Jan 8, 2004

Dekorsy, T.
Silicon based photonics
AMOLF Amsterdam, Netherlands, March 29, 2004

Dekorsy, T.
Coherent phonons in condensed matter
Kolloquium of SFB 450, Berlin, Germany, May 18, 2004

Dekorsy, T.
Silicon based photonics
Philips Research, Eindhoven, Netherlands, June 4, 2004

Dekorsy, T.
Coherent phonons in condensed matter
Kolloquium Optik und Kondensierte Materie, University Bonn, Germany, Nov 9, 2004

Fassbender, J.
Maßgeschneiderte magnetische Materialien – neue Wege durch Ionenbestrahlung
TU Dresden, Physikalisches Kolloquium, Germany, 2004

Fassbender, J.
Modification of magnetic thin films and nanostructures by ion irradiation and implantation
Hitachi Almaden, San Jose, USA, Oct 8, 2004

Heinig, K.-H.

Nanostructure formation with ion beams
University Aarhus, Denmark, Oct 7, 2004

Heinig, K.-H.
Physik fernab vom Gleichgewicht: Nanostrukturierung mit Ionenstrahlen
Universität Jena, Physikalisches Kolloquium, Germany, Nov 1, 2004

Helm, M.
Silicon light-emitting pn diodes
Dept. of Electrical Engineering, Princeton University, USA, Feb 11, 2004

Helm, M.
Short-wavelength ($\lambda < 4$ µm) intersubband transitions and quantum cascade lasers in InP-based material systems
Dept. of Electrical Engineering, Princeton University, USA, Feb 26, 2004

Krause-Rehberg, R., Bondarenko, V., Brauer, G.
EPOS – ELBE positron source: positron annihilation multifacility project in Dresden
MATERIALICA, Neue Messe München, Germany, Sept 21–23, 2004

Möller, W.
Ionenstrahltechnologien
Weiterbildungskurs "Surface Engineering und Nanotechnologie (SENT), Herstellung und Anwendung dünner Schutzschichten", Dresden, Germany, Oct 27, 2004

Möller, W.
Beschichtungsplasmen
Weiterbildungskurs "Surface Engineering und Nanotechnologie (SENT), Herstellung und Anwendung dünner Schutzschichten", Dresden, Germany, Oct 27, 2004

Möller, W.
Oberflächen- und Schichtanalyse mit Hochenergie-Ionen
Weiterbildungskurs "Surface Engineering und Nanotechnologie (SENT), Charakterisierung dünner Schichten", Dresden, Germany, Dec 8, 2004

Neelmeijer, C.
Ionenstrahlen im Dienste der Kunst
Lange Nacht der Wissenschaften, Dresden, Germany, June 25, 2004

Neelmeijer, C.
Ionenstrahlen im Dienste der Kunst
Physikalisches Seminar, Hochschule für Technik und Wirtschaft Dresden, Germany, Dec 7, 2004

Oates, T.W.H.
Metal island/polymer composite films: novel properties and applications
Group of Macromolecular Physics, Charles University, Prague, Czech Republic, Dec 10, 2004

Skorupa, W.
Silicon-based light emission from ion-implanted materials
Dept. of Physics, Oslo University, Oslo, Norway, Aug 12, 2004

Skorupa, W.
Silizium-basierte Lichtemission und Blitzlampen-Temperung: Innovationen bei FWI
Senioren-Club des FZR, Dresden, Germany, Nov 4, 2004

Skorupa, W.
Blitzlampen-Temperung im msec-Bereich für die SiC-Si-Heteroepitaxie
Institut für Angewandte Physik, Universität Erlangen-Nürnberg, Germany, Nov 11, 2004

Skorupa, W.
Flash lamp processing for Group IV semiconductors
Dept of Engineering, University of Cambridge, UK, Dec 2, 2004

Winnerl, S.
LEDs und Laserdioden: Die Lichtrevolution
Lange Nacht der Wissenschaften, Dresden, Germany, June 25, 2004

Winnerl, S.
THz radiation and Bloch oscillations - old visions and new approaches
Dept. of Theoretical Physics, University of Oulu, Finland, Dec 15, 2004

Reports

Heer, R., Wagener, M., Winnerl, S.
MoBeE, Prozesssteuerung an der Molekularstrahl-Epitaxie-Anlage
FZ Jülich: Interner Bericht FZJ-ZEL-IB-500104, 2004

Heinig, K.-H., Schmidt, B., Müller, T.
Abschlußbericht EU-GROWTH-Project NEON

Panknin, D., Skorupa, W.
Flash Lamp Supported Deposition of 3C-SiC(FLASiC)
EU-GROWTH-Project (V. Framework), Two-Year-Report, March 2004

Skorupa, W.
Luminescence and memory effects in SiO_2 layers containing Si/Ge nanoclusters
WTZ Ukraine, Abschlussbericht, Dec 2004

Patents

Dekorsy, T., Dreyhaupt, A., Winnerl, S., Helm, M.
Kohärente Terahertz-Strahlungsquelle
Patentanmeldung beim Deutschen Patentamt DE 10 2004 046 123.6 (2004)

Friedrich, M., Tyrroff, H.
Sputterionenquelle
Patentanmeldung 102 41 252.9 ; DE 102 41 252 B4 ; EP 1 396 870 A3

Georgiev, N., Dekorsy, T., Helm, M., Semtsiv, M., Dreßler, S., Ziegler, M., Masselink, W.
Quanten-Kaskaden-Laser-Struktur
Patentanmeldung beim Deutschen Patentamt DE 10 2004 009 531.0 (2004)

Niemann, E., Panknin, D., Skorupa, W., Wirth, H.
Verfahren zur Herstellung eines mikroelektronischen Halbleiterbauelementes mittels Ionenimplantation
Deutsches Patent DE 198 08 246 B4 (erteilt 13.5.2004)

Pilz, W., Bischoff, L.
Emitter for an ion source and method of producing same
European patent application 04017894.9
Applicant: ICT GmbH 28.07.2004

Rogozin, A., Vinnichenko, M., Kolitsch, A.
In situ Verfahren zur Filmoptimierung bei der ITO-Abscheidung
Patentanmeldung 103 12 593.0; DE 103 12 593 A1

Shevchenko, N., Maitz, M.F., Pham, M.T.
Verfahren zur Herstellung nickelarmer Oberflächen auf Nitinol
DE 103 23 410 A1

Skorupa, W., Nazarov, A., Yankov, R., Gebel, T., Rebohle, L.
Verfahren zur Behandlung Silizium-basierter Lichtemitter
Patentanmeldung 103 13 727.0; DE 103 13 727 A1

Voelskow, M., Anwand, W., Skorupa, W.
Verfahren zur Behandlung von Halbleitersubstraten, die mittels intensiven Lichtimpulsen ausgeheilt werden
Deutsche Patentanmeldung DE 10 2004 047 594.6 (30.09.2004)

Voelskow, M., Anwand, W., Skorupa, W.
Blitzlampenspiegelanordnung
Deutsche Patentanmeldung DE 10 2004 060 557.2 (16.12.2004)

Master Thesis

Lange, H.
Online-Bestimmung von Betriebsparametern an Van-de-Graaff-Ionenbeschleunigern
HTW Dresden, Dec 2004

Diploma Theses

Gumprich, A.
Archäometrische Untersuchungen an den Goldteilen aus dem Hortfund von Nebra
TU Bergakademie Freiberg, April 2004

Güttler, D.
Echtzeit-in-situ-Messung der Oberflächenbelegung einer Magnetron-Kathode bei der reaktiven Sputter-Abscheidung
TU Dresden, July 2004

Henry, R.
Characterization and Optimization of an electron cyclotron resonance ion source
TU Dresden, Dec 2004

Menzel, S.
Intersubbandspektroskopie an Antimonid-basierten Halbleiter Quantenstrukturen
TU Dresden, Nov 2004

Mucke, S.

Herstellung von Nanometer-Strukturen mittels feinfokussiertem Ionenstrahl (FIB)
Hochschule Mittweida (FH), Feb 2004
Wissenschaftlich-Technische Berichte, FZR-402, April 2004

PhD Theses

Abendroth, B.
Ion-induced stress relaxation during the growth of cubic boron nitride thin films
TU Dresden, July 2004
Wissenschaftlich-Technische Berichte, FZR-406 , 2004

Akhmadaliev, C.
Investigation of acoustic waves generated in an elastic solid by a pulsed ion beam and their application in a FIB based scanning ion acoustic microscope
TU Dresden, Oct 2004
Wissenschaftlich-Technische Berichte, FZR-416, 2004

Schmidt, J.
Synthesis of silicon nanocrystal memories by sputter deposition
TU Dresden, Nov 15, 2004

Awards

Röntzsch, L.
EMRS – Young Scientist Award, Strasbourg, France, May 2004

Röntzsch, L.
IBMM 2004 Poster Award, Monterey, USA, Sept 2004

Organization of Meetings

Tutorial "Thin Film Diagnostics"
EU-RTN "New Fullerene Like Materials", FZ Rossendorf, Dresden, Germany, June 3–5, 2004
Möller, W., Kolitsch, A.

Mößbauerkolloquium Dresden 2004
FZ Rossendorf, Dresden, Germany, Sept 30–Oct 1, 2004
Reuther, H.

Flash lamp processing at FZR
Workshop: RTP & Blitzlampen-Temperverfahren, FZ Rossendorf, Dresden, Germany, Oct 21, 2004
Skorupa, W.

Laboratory Visits

Beckers, M.
ESRF Grenoble, ROBL-Beamline, France, June 15–21, Oct 28–Nov 2, 2004

Beckers, M.

Thin Film Physics Group, Linköping University, Sweden, Nov 25–Dec 2, 2004

Beckers, M.
Department of Solid State Sciences, University Gent, Belgium, Dec 7–8, 2004

Bischoff, L.
Ruhr-Universität Bochum, Lehrstuhl für Angewandte Festkörperphysik, Germany, April 21–23, 2004

Borany, J. von
ESRF Grenoble, ROBL-Beamline, France, April 6–13, Dec 15–18, 2004

Eichhorn, F.
ESRF Grenoble, ROBL-Beamline, France, April 12–17, July 19–27, Dec 16–20, 2004

Eichhorn, F.
Institute of Electronic Materials Technology, Warsaw, Poland, June 13–19, Nov 22–27, 2004

Gago, R.
Instituto de Ciencia de Materiales de Madrid, CSIC, Madrid, Spain, Feb 13–22, May 8–16, 2004

Gago, R.
Berliner Elektronenspeicherringgesellschaft für Synchrotronstrahlung m.b.H. (BESSY), Berlin, Germany, June 14–25, 2004

Grenzer, J.
Institute of Electronic Materials Technology, Warsaw, Poland, Nov 23–26, 2004

Heinig, K.-H.
CNRS/CEMES, Toulouse, France, Jan 27–29, 2004

Heinig, K.-H.
CSNSM Orsay, Paris, France, Feb 4–11, 2004

Heinig, K.-H.
CSNSM Orsay, Paris, France, Oct 25–29, 2004

Helm, M.
Princeton University, Dept. of Electrical Engineering, Princeton, NJ, USA, Feb 4–March 2, 2004

Kögler, R.
University of Oslo, Oslo, Norway, August 9–13, 2004

Neelmeijer, C.
Rutherford Appleton Laboratory, Chilton, UK, March 20–26, 2004

Rogozin A.
ESRF Grenoble, ROBL-Beamline, France, Feb 12–17, Sept 5–12, 2004

Schell, N.
CENIMAT F.C.T., Universidade Nova de Lisboa, Portugal, April 23–26, 2004

Schell, N.
University of Aarhus, Aarhus, Denmark, Dez 5–8, 2004

Schumann, T.

University of Oslo, Oslo, Norway, Aug 9–13, Nov 6–20, 2004

Shevchenko, N.
ESRF Grenoble, ROBL-Beamline, France, Feb 12–17, Sep 5–12, 2004

Skorupa, W.,
University of Oslo, Oslo, Norway, Aug 9–13, 2004

Skorupa, W.
University of Cambridge, and Heraeus Noblelight, Cambridge, UK, Dec 1–4, 2004

Voelskow, M.
University of Cambridge, and Heraeus Noblelight, Cambridge, UK, Dec 1–4, 2004

Weishart, H.
University of Cambridge, and Heraeus Noblelight, Cambridge, UK, Dec 1–4, 2004

Winnerl, S.
University of Oulu, Department of Theoretical Physics, Oulu, Finland, Dec 13–18, 2004

Guests

Alonso, E.
Institut für Integrierte Systeme der ETH Zürich, Zürich, Switzerland, March 8–13, 2004

Ayache, R.
University of Batna, Algeria, May 3–June 9, 2004

Balaszi, C.
KFKI Budapest, Hungary, April 4–9, 2004

Barinov, S.
Institute for Physical Chemistry of Ceramics, Moscow, Russia, Aug 15–Sept 5, 2004

Becker, H.-W.
Universität Bochum, Germany, Jan 13–15, 2004

Bernas, H.
CSNSM Orsay, Paris, France, Dec 12–16, 2003

Bilek, M.M.
University of Sydney, Australia, June 1–11, 2004

Braz Fernandes, F.M.
CENIMAT F.C.T., Universidade Nova de Lisboa, Lisbon, Portugal, Sept 26–Oct 3, 2004

Chumlyakov, Y.
Tomsk State University, Russia, July 7–9, 2004

Cizek, J.
Charles University, Prague, Czech Republic, Jun 2–4, Dec 3–13, 2004

Dagkaldiran, Ü.
Universität Bochum, Germany, Jan 13–5, March 9–12, May 26–28, 2004

Dvurechenskii, A.V.
Institut of Semiconductor Physics, Novosibirsk, Russia, Nov 1–13, 2004

El-Hossary, F.M.
South Valley University, Sohag, Egypt, Jan 12–16, 2004

Fritz, E.
Universität Bochum, Germany, Jan 13–15, 2004

Gorshin, A.
University of Lipetsk, Russia, Jan 12–Feb 8, 2004

Gracia, F.
University of Sevilla, Spain, Aug 2–Sept 18, 2004

Guschtschina, N.
Institute for Electrophysics, Jekaterinburg, Russia, Dec 1–21, 2004

Jagielski, J.
ITME Warsaw, Poland, March 3–5, 2004

Jembrih-Simbürger, D.
Academy of Fine Arts Vienna, Austria, April 25–May 1, 2004

Karpour, A.
University of Sydney, Australia, Oct 1–Dec 15, 2004

Komlev, V.
Institute for Physical Chemistry of Ceramics, Moscow, Russia, Aug 15–Sept 5, 2004

Kondyurin, A.
University of Perm, Russia, Jan 1–Sept 30, 2004

Kubarev, O.
Institute for Physical Chemistry of Ceramics, Moscow, Russia, Aug 15–Sept 5, 2004

Kuriplach, J.
Charles University, Prague, Czech Republic, March 24–April 7, Aug 11–13, Nov 18–Dec 2, 2004

Ma, X.
Institute of Technology, Harbin, China, June 8–Sept 8, 2004

Mackova, A.
Institute of Nuclear Physics, Řež, Czech Republic, May 24–June 8, June 14–19, Dec 8–10, 2004

Mäder, M.
Akademie der Bildenden Künste Wien, Austria, July 5–9, 2004

Markov, A.
Institute for High Current Elektronics, Tomsk, Russia, Sept 1–Oct 31, 2004

Mair, A.W.R.
University of Manchester, U.K., Aug 15–Sept 15, 2004

McMahon, R.

Univ. of Cambridge, Engineering Department, U.K., March 5–7, 2004

Meijer, J.
Universität Bochum, Germany, Jan 13–15, March 9–12, 2004

Misochko, O.
Institut für Festkörperphysik, Chernogolovka, Russia, May 10–28, 2004

Music, D.
RWTH Aachen, Germany, Feb 10–12, Aug 25–28, 2004

Nazarov, A.N.
Ukrain. Academy of Sciences, Kyiv, Ukraine, July 19–Aug 17, 2004

Osiyuk, I.N.
Ukrain. Academy of Sciences, Kyiv, Ukraine, June 17–Aug 17, 2004

Ovchinnikov, V.
Institute for Electrophysics, Jekaterinburg, Russia, Nov 1–30, 2004

Owusu, H.
University Cape Cost, Ghana, July 7–Sept 30, 2004

Peeva, A.
Academy of Sciences of Bulgaria, Sofia, March 1–April 30, June 20–Aug 20, 2004

Piekoszewski, J.
Soltan Institute, Otwock-Swierk, Poland, June 1–6, Aug 12–15, 2004

Preoteasa, E.
Horia Hulubei National Institute, Bucharest, Romania, June 29–July 9, 2004

Razek, N.
Institut für Oberflächenmodifizierung, Leipzig, Germany, Nov 29–Dec 7, 2004

Ryves, L.J.S.
University of Sydney, Australia, June 1–11, 2004

Salavcová, L.
Institute of Chemical Technology, Prague, Czech Republic, May 24–28, 2004

Saude, S.
DGA-CTA-LOT Arcueil, France, Jan 29–Feb 15, 2004

Shkatov, V.
University of Lipetsk, Russia, Jan 12–Feb 8, 2004

Smith, M.
Univ. of Cambridge, Engineering Department, U.K., March 5–7, 2004

Svensson, B.G.
University of Oslo, Oslo, Norway, July 7–9, 2004

Tschernychev, V.
Universität Bochum, Germany, March 9–12, May 26–28, 2004

Tsvetkova, T.
Institute of Solid State Physics, Bulgarian Academy of Sciences, Bulgaria, Oct 9–30, 2004

Tsyganov, I.
University of Lipetsk, Russia, Jan 12–Feb 8, Aug 9–Dec 31, 2004

Turos, A.
ITME Warsaw, Poland, Feb 15–19, March 1–4, Aug 24–28, Oct 25–29, Dec 15–18, 2004

Tyagulskii, I.P.
Ukrain. Academy of Sciences, Kyiv, Ukraine, June 17–Aug 17, 2004

Ueda, M.
INPE San Jose dos Campos, Brasil, Sept 27–29, 2004

Villas-Boas Tribuzy, C.
CNPQ, Brasilien, Sept 13–Dec 31, 2004

Vinnichenko, M.
University Kiev, Ukraine, Jan 1–Feb 29, 2004

Vogel, T.
Universität Bochum, Germany, March 9–12, 2004

Werner, Z.
Soltan Institute, Otwock-Swierk, Poland, June 1–6, Aug 12–15, 2004

ROBL-MRH Visitors

Andreasen, K.P.
Dept. of Physics and Astronomy, University of Aarhus, Denmark, Feb 17–24, 2004

Baranowska, J.
TU Szczecin, Poland, April 16–20, 2004

Bøttiger, J.
Dept. of Physics and Astronomy, University of Aarhus, Aarhus, Denmark, Feb 17–24, 2004

Braz Fernandes, F.M.
CENIMAT F.C.T., Universidade Nova de Lisboa, Lisbon, Portugal, March 2–9, 2004

Busquets, D.
University Politécnica de Valencia, Spain, April 16–20, 2004

Cordeiro Silva, R.J.
CENIMAT F.C.T., Universidade Nova de Lisboa, Lisbon, Portugal, March 2–9, 2004

Falub, C.
Institute for Semiconductor Physics, Johannes Kepler Universität, Linz, Austria, Dec 8–13, 2004

Gaca, J.
ITME Warsaw, Poland, July 22–27, Oct 26–31, 2004

Kräußlich, J.

Institute for Optics and Quantumelectronics, FSU Jena, Jena, Germany, May 7–11, 2004

Mahesh, K.
CENIMAT F.C.T., Universidade Nova de Lisboa, Lisbon, Portugal, Sept 17–21, 2004

Mazur, K.
ITME Warsaw, Poland, July 19–24, Dec 16–20, 2004

Meduňa, M.
Institute of Condensed Matter Physics, Masaryk University, Brno, Czech. Republic, Dec 7–13, 2004

Mikula, P.
Nuclear Physics Institute, Řež, Czech. Republic, Feb 12–14, 2004

Novák, J.
Institute for Semiconductor Physics, Johannes Kepler Universität, Linz, Austria, Dec 8–13, 2004

Paula, A.
CENIMAT F.C.T., Universidade Nova de Lisboa, Lisbon, Portugal, Sept 17–21, 2004

Prinz, H.
AMD Saxony, Dresden, Germany, June 22–29, Nov 16–23, 2004

Pyzalla, A.
Institut für Werkstoffkunde, TU Wien, Vienna, Austria, July 12–19, 2004

Rinderknecht, J.
AMD Saxony, Dresden, Germany, June 22–29, Nov 16–23, 2004

Sass, J.
ITME Warsaw, Poland, July 19–24, Dec 16–20, 2004

Scheffzük, C.
GeoForschungszentrum Potsdam, Germany, Feb 9–15, 2004

Silva da, P.
Institut für Werkstoffkunde, TU Wien, Vienna, Austria, July 12–19, 2004

Silva, M.
CENIMAT F.C.T., Universidade Nova de Lisboa, Lisbon, Portugal, March 2–9, 2004

Skorina, M.
Institut für Materialwissenschaft und Technologie, TU Berlin, Berlin, Germany, July 1–19, 2004

Som, T.
Institute of Physics, Bhubaneswar, India, May 3–7, 2004

Walther, K.
GeoForschungszentrum Potsdam, Germany, Feb 9–15, 2004

Wojcik, M.
ITME Warsaw, Poland, July 22–27, Oct 26–31, 2004

Wunderlich, F.
Institute for Optics and Quantumelectronics, FSU Jena, Jena, Germany, May 7–11, 2004

Zienert, I.
AMD Saxony, Dresden, Germany, June 23–26, Nov 16–23, 2004

Marie Curie Fellows

Gushterova, P.
Central Laboratory for Optical Storage and Processing of Information, Bulgarian Academy of Sciences, Bulgaria, Sept 2003–June 2004, Sept–Nov, 2004

Harangus, L.
Horia Hulubei National Institute, Bucharest, Romania, Jan 2–Dec 28, 2004

Iordan, A.
Horia Hulubei National Institute, Bucharest, Romania, Jan 2–Dec 28, 2004

Prucnal, S.
Marie Curie-Sklodowska University Lublin, Poland, Jan 1–Nov 30, 2004

Colloquium of the Institute

H. Bracht – Universität Münster, Institut für Materialphysik/Germany
Advanced diffusion studies with isotopically controlled semiconductors
June 10, 2004

G. Bräuer – FhI für Schicht- und Oberflächentechnik Braunschweig/Germany
Dünne Schichten mit großer Wirkung – alltägliche und nicht alltägliche Beispiele
Jan 8, 2004

B. Büchner – IFW Dresden, Institut für Festkörperforschung/Germany
Ladungsordnungsphänomene in Übergangsmetalloxiden
May 6, 2004

J. Cizek – Dept. of Low Temperatur Physics, Charles University Prague/CZ
H-induced defects in Nb
June 3, 2004

R. Fromknecht – FZ Karlsruhe/Germany
Entwicklung von Nanosystemen in keramischen Oxyden durch Ionenimplantation
Jan 15, 2004

H. Haberland – Universität Freiburg, Fakultät für Physik/Germany
Dünne Schichten aus schnellen Clustern
Jan 22, 2004

N. Kaiser – FhI für Angewandte Optik und Feinmechanik, Jena/Germany
Optische Schichten – Trends
Oct 21, 2004

H. von Löhneysen – Physikalisches Institut, Universität Karlsruhe/Germany
Metalle an einer magnetischen Instabilität
Sept 2, 2004

R. Sauerbrey – Institut für Optik und Quantenelektronik, FSU Jena/Germany
Teilchenbeschleunigung und Kernreaktionen mit hochintensiven Lasern
Dec 2, 2004

M. Stamm – Institut für Polymerforschung Dresden/Germany
Nanostrukturen und Organisation von Polymeren an Oberflächen
June 24, 2004

N. Stolterfoht – HMI Berlin/Germany
Führung hochgeladener Ionen durch Nanokapillare in Nichtleitern
June 17, 2004

B.G. Svensson – Dept. of Physics, University of Oslo/Norway
High purity Si and SiC for radiation detectors: impurity engineering, defects and diffusion
July 8, 2004

H. Winter – Institut für Physik der Humboldt-Universität zu Berlin/Germany
Untersuchung von Oberflächen und ultradünnen Filmen mittels streifender Ionenstreuung
Oct 28, 2004

J. Wrachtrup – 3. Physikalisches Institut der Universität Stuttgart/Germany
Defects in diamond: future hardware for quantum computing?
Dec 9, 2004

M. Zacharias – MPI für Mikrostrukturphysik, Halle/Germany
Nanowire a la carte
Dec 16, 2004

Other Seminars

H. Bernas – CSNSM, Université d'Orsay/France
Dynamics of irradiation/implantation: what in situ TEM teach us
Dec 15, 2004

F.M. Braz Fernandez – CENIMAT, New University of Lisboa/Portugal
Thermal and mechanical interactions with phase transformations
Sept 29, 2004

L.C. Brunel – National High Magnetic Field Laboratory, Florida State University, Tallahassee/USA
A future for electron magnetic resonance: high frequency time domain spectroscopy with application to quantum information processing
Oct 14, 2004

J. Bundesmann – HMI Berlin/Germany
CODIAN, ein Kontrollsystem für Ionenquellen
Feb 2, 2004

D. Citrin – Georgia Institute of Technology, Atlanta, Georgia/USA
Terahertz properties of Semiconductors
June 22, 2004

D. Depla – Dept. for Solid State Sciences, University Ghent/Belgium
Effects of reactive ion implantation during magnetron sputtering
Jan 14, 2004

F.M. El-Hossary – Physics Dept., South Valley University, Sohag/Egypt
Surface modification of Titanium by Rf plasma nitriding
Jan 16, 2004

C. Foerster - University of Ilmenau/Germany
Technology for 3C-SiC/Si heterostructures for sensor applications
June 8, 2004

F. Hudert – TU Ilmenau/Germany
Optische Spektroskopie an $CuInS_2$
Nov 12, 2004

J. Kono – Rice University, Houston, Texas/USA
Extreme nonlinear optics in semiconductors with small energy photons
June 15, 2004

O. Liepack – Jet Propulsion Laboratory, Pasadena/USA
Overview over the Mars exploration rover mission
Nov 10, 2004

V. Rigato – Laboratori Nazionali di Legnaro, Padova/Italia
On the importance of Ion Beam Analysis for the investigation of multilayers with nanometric periodicity
March 4, 2004

A. Schreyer – Institut für Werkstofforschung, GKSS Geesthacht/Germany
Materialforschung mit Neutronen- und Synchrotronstrahlung bei GKSS: Von Schweißnähten zum Nanomagnetismus
June 22, 2004

S. Zhou – Institut vor Kern- en Stralingsfysica, University of Leuven/Belgium
Defects and strain in epitaxial ZnO and GaN thin films
Sept 23, 2004

Projects

04/2000 – 03/2004 Deutsche Forschungsgemeinschaft DFG
Ion beam synthesis of doped diamond-SiC-heterostructures
Dr. V. Heera Tel.: 0351 260-3343 v.heera@fz-rossendorf.de

10/2000 – 01/2005 European Union, Marie-Curie-Program EU
Stays at Marie-Curie Training Site
Dr. A. Kolitsch Tel.: 0351 260-3348 a.kolitsch@fz-rossendorf.de

02/2001– 01/2004 European Union, Growth Project EU
Nanoclusters for Electronics (NEON)
Dr. K.-H. Heinig Tel.: 0351 260-3288 k.h.heinig@fz-rossendorf.de

04/2001 – 06/2004 Sächsisches Staatsministerium für Wirtschaft und Arbeit SMWA
Erhöhung der Funktionssicherheit dünner Barrieren auf Ta-Basis für Kupfer-Metallisierungssysteme, Teilthema: Plasma-Immersions-Ionenimplantation
Dr. J. von Borany Tel.: 0351 260-3378 j.v.borany@fz-rossendorf.de

04/2001 – 06/2004 Bundesministerium für Bildung und Forschung BMBF

Zusammenhang zwischen Plasmaparametern und Schichteigenschaften beim MF-Puls-Magnetronsputtern
Dr. A. Kolitsch Tel.: 0351 260-3348 a.kolitsch@fz-rossendorf.de

10/2001 – 12/2004 Bundesministerium für Bildung und Forschung Auftrag
Hochenergie-Ionenimplantation in Si-Wafer für Bauelemente der Leistungselektronik
Dr. J. von Borany Tel.: 0351 260-3378 j.v.borany@fz-rossendorf.de

11/2001 – 10/2004 Boston Scientific Ltd. Auftrag
Hafnium coatings on medical devices
Dr. E. Richter Tel.: 0351 260-3326 e.richter@fz-rossendorf.de

04/2002 – 06/2005 European Union EU
Flash lamp supported deposition of 3C-SiC films
Dr. W. Skorupa Tel.: 0351 260-3612 w.skorupa@fz-rossendorf.de

07/2002 – 05/2004 Deutsche Forschungsgemeinschaft DFG
Infrarotspektroskopie an Quantenkaskadenstrukturen
Prof. M. Helm Tel.: 0351 260-2260 m.helm@fz-rossendorf.de

07/2002 – 06/2004 North Atlantic Treaty Organization NATO
Combined time- and frequency-domain study of superconductors and manganites
Dr. T. Dekorsy Tel.: 0351 260-2880 t.dekorsy@fz-rossendorf.de

09/2002 – 08/2005 WTZ with Russia WTZ
Dynamische Bestrahlungseffekte in metastabilen Legierungen unter Ionenbeschuss
Dr. E. Richter Tel.: 0351 260-3326 e.richter@fz-rossendorf.de

10/2002 – 09/2005 WTZ with Poland WTZ
Strukturelle Charakterisierung von Heterostrukturen für die Opto- und Mikroelektronik
Dr. F. Eichhorn Tel.: 0351 260-3534 f.eichhorn@fz-rossendorf.de

10/2002 – 09/2006 European Union EU
Synthesis, structure and properties of new fullerene like materials
Dr. A. Kolitsch Tel.: 0351 260-3348 a.kolitsch@fz-rossendorf.de

11/2002 – 11/2005 Deutsche Forschungsgemeinschaft DFG
Phasen- und Strukturdesign von Ti-Al-N-Schichten durch Echtzeit-in-situ-Röntgendiffraktion
Dr. N. Schell Tel.: +33 (0)4.76.88.23.67 schell@esrf.fr

01/2003 – 12/2005 Bundesministerium für Bildung und Forschung BMBF
Substituted hydroxyapatite for improved adsorption of osteoinductive factors
Dr. E. Richter Tel.: 0351-260-3326 e.richter@fz-rossendorf.de

04/2003 – 03/2005 Arbeitsgemeinschaft industrieller Forschungsvereinigungen AiF
Oxidationsschutz für neuartige Hochtemperatur- Leichtbauwerkstoffe durch Ionen-implantation
Dr. E. Richter Tel.: 0351-260-3326 e.richter@fz-rossendorf.de

08/2003 – 04/2005 Applied Materials, ICT GmbH Auftrag
Fabrication and investigation of the parameters of LMIS emitters
Dr. L. Bischoff Tel.: 0351 260-2963 l.bischoff@fz-rossendorf.de

01/2004 – 12/2005 WTZ mit Norwegen DAAD
Ion implantation induced defects in Si-SiGe-based heterostructures

Dr. R. Kögler Tel.: 0351 260-3613 r.koegler@fz-rossendorf.de

01/2004 – 12/2005 DAAD-Acciones Integradas Hispano-Alemanas DAAD
Preparation and characterization of Boron-Carbon-Nitrogen compounds: functional materials for biocompatibility
Prof. W. Möller Tel.: 0351-260-2245 w.moeller@fz-rossendorf.de

03/2004 – 02/2009 European Union EU
Integrating Activity on Synchrotron and Free Electron Laser Science
Prof. M. Helm Tel.: 0351 260-2260 m.helm@fz-rossendorf.de

07/2004 – 06/2006 Deutsche Forschungsgemeinschaft DFG
Theoretische Untersuchungen zu Wachstum, Stabilität und Funktionalität von Nanodrähten
Dr. K.-H. Heinig Tel.: 0351 260-3288 k.h.heinig@fz-rossendorf.de

07/2004 – 06/2006 Deutsche Forschungsgemeinschaft DFG
Synthese von Nanodrähten und Nanoketten mit feinfokussierten Ionenstrahlen
Dr. B. Schmidt Tel.: 0351 260 2726 bernd.schmidt@fz-rossendorf.de

08/2004 – 07/2006 European Union, Marie-Curie-Program EU
Polymer surface modification by ion implantation
Dr. E. Richter Tel.: 0351 260-3326 e.richter@fz-rossendorf.de

09/2004 – 06/2006 Bundesministerium für Bildung und Forschung BMBF
Funktionalisierung der Oberflächen von Polyurethan als Basiswerkstoff für flexible und im Blutkontakt stehende medizinische Implantate und Devices
Dr. E. Richter Tel.: 0351-260-3326 e.richter@fz-rossendorf.de

09/2004 – 08/2006 WTZ with Russia WTZ
Titan im Blutkontakt
Dr. E. Richter Tel.: 0351-260-3326 e.richter@fz-rossendorf.de

10/2004 – 12/2005 AMD Saxony Auftrag
Strukturuntersuchungen an BEOL-Komponenten
Dr. N. Schell Tel.: +33 (0)4.76.88.23.67 schell@esrf.fr

Experimental Equipment

1. Accelerators, Ion Implanters and Ion-Assisted-Deposition

⇒	Van de Graaff accelerator	(VdG)	1,8 MV	*TuR Dresden, D*
⇒	Tandem accelerator	(Td)	5 MV	*NIIEFA, RU*
⇒	Tandetron accelerator	(Tdtr)	3 MV	*HVEE, NL*
⇒	Ion implanter		80 kV	Own construction
⇒	Low energy ion implanter		0.5 – 50 keV	*DANFYSIK, DK*
⇒	High current ion implanter		200 kV, high current	*DANFYSIK, DK*
⇒	High energy ion implanter		500 kV	*HVEE, NL*
⇒	Plasma-immersion ion implantation		5 – 60 keV	Own construction
⇒	Fine focused ion beam		30 keV, 15 nm, 10 A/cm^2	*ORSAY Physics, F*
⇒	Dual beam magnetron sputter deposition			*ROTH & RAU; D*
⇒	Ion beam assisted deposition			
⇒	UHV He-irradiation		0 – 5 keV, Scan 10x10 mm^2	*VG, USA*

2. Ion Beam Analysis (IBA)

A wide variety of advanced IBA techniques are available at the MeV accelerators of the Ion Beam Centre Rossendorf.

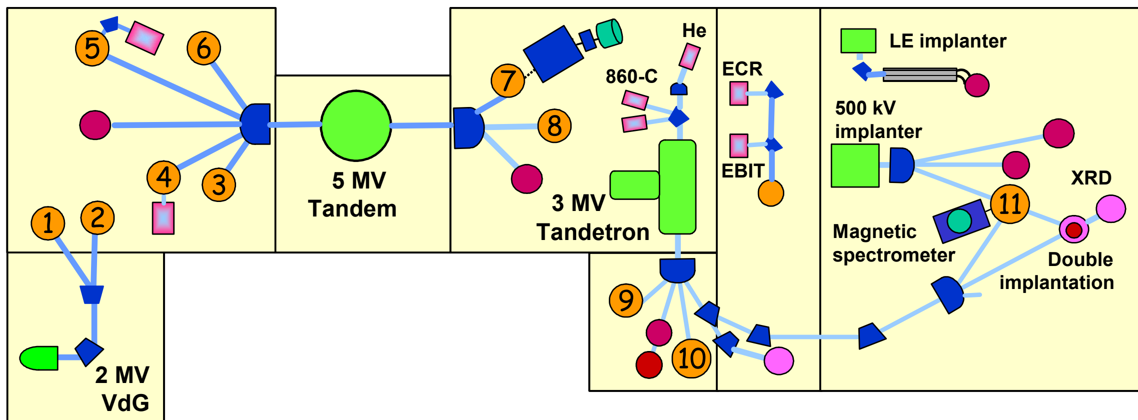

⇒	RBS	Rutherford backscattering	(1), (2), (3), (9)	VdG, Td, Tdtr
⇒	RBS/C	RBS + channelling	(1), (2), (3), (9)	VdG, Td, Tdtr
		High-resolution RBS/C	(11)	Tdtr
⇒	ERDA	Elastic recoil detection analysis	(2), (4), (5)	VdG, Td
⇒		High-resolution ERDA	(7), (8)	Td
⇒	PIXE	Proton induced X-ray emission	(3)	Td
⇒	PIGE	Proton induced γ emission	(3)	Td
⇒	NRA	Nuclear reaction analysis	(4)	Td
⇒	NRRA	Nuclear resonance reaction analysis	(6)	Td
⇒	NMP	Nuclear microprobe	(10)	Tdtr

Some stations are equipped with additional process facilities which enable *in-situ* IBA investigations during ion irradiation, sputtering, deposition, annealing etc.

3. Other Particle Based Analytical Techniques

⇒	SEM	Scanning electron microscope	<1 - 30 keV, EDX	*HITACHI, Jp.*
⇒	TEM	Transmission electron microscope	300 kV	*PHILIPS, NL*
⇒	AES	Auger electron spectroscopy	+ XPS-option	*FISIONS, GB*
⇒	CEMS	Mössbauer spectroscopy	^{57}Fe source	

4. Photon Based Analytical Techniques

⇒	XRD/XRR	X-ray diffraction / X-ray reflection	8.04 keV (Cu-K_{α})	*BRUKER AXS, D*
	XRD/XRR	with Synchrotron radiation	5 – 35 keV	*ROBL-CRG at ESRF, F*
⇒	SE	Spectroscopic ellipsometry	250 - 1700 nm	*WOOLLAM, USA*
⇒	FTIR	Fourier transform infrared spectrometry	600 - 7000 cm^{-1}	*NICOLET, USA*
⇒	FTIR	Fourier transform infrared spectrometry with infrared microscope	50 - 15000 cm^{-1}	*BRUKER, D*
		Ti:Sapphire femtosecond laser		*SPECTRA PHYSICS, USA*
		Femtosecond optical parametric oscillator		*APE, D*
		Ti:Sapphire femtosecond amplifier		*FEMTO LASER, A*
		Femtosecond optical parametric amplifier		*LIGHT CONVERSION, LT*
⇒	Raman	Raman spectroscopy (532 nm, 633 nm)	> 45 cm^{-1} shift	*JOBIN-YVON-HORIBA, F.*
⇒	PL	Photoluminescence	300 – 1500 nm	*JOBIN-YVON-HORIBA, F.*
⇒	EL	Electroluminescence (10-300 K)	300 – 1500 nm	*JOBIN-YVON-HORIBA, F*
⇒		Optical split-coil supercond. magnet	7 T	*OXFORD INSTRUM., UK*
⇒	PR	Photomodulated reflectivity	300 – 1500 nm	*JOBIN-YVON-HORIBA, F.*
⇒	PLE	Photoluminescence Excitation	300 – 1500 nm	*JOBIN-YVON-HORIBA, F.*
⇒	TRPL	Time resolved PL	τ > 5 ns	*STANFORD RESEARCH, USA*

5. Magnetic Analysis

⇒	MOKE	Magneto-Optic Kerr Effect	± 200 Oe	Home-built
			± 3.5 kOe	Home-built
⇒	MFM	Magnetic Force Microscope	~ 50 nm resol.	*VEECO/DI, USA*

6. Other Analytical and Measuring Techniques

⇒	Scanning tunneling microscope (with AFM-option)	*DME, DK*
⇒	Dektak surface profilometer	*VEECO, USA*
⇒	Micro indenter	*SHIMATSU, J*
⇒	Scratch tester	*SHIMATSU, J*
⇒	Spreading resistance profiling	*SENTECH, D*
⇒	Hall-effect equipment	*BIO-RAD, GB*
⇒	I-V and C-V analyzer	*KEITHLEY, USA*
⇒	Wear tester (pin-on-disc)	Own construction

7. Preparation Techniques

⇒	Wet chemical etching and cleaning	including anisotropic selective KOH-etching	
⇒	Photolithographic patterning	5 µm-level	
⇒	Thermal treatment	Room Temperature - 2000°C	
		• Furnace	*INNOTHERM*
		• Rapid thermal annealing	*ADDAX, F*
		• Flash lamp unit (0.5 – 20 ms)	
		• RF-Heating (Vacuum)	*NORDIKO, GB*
⇒	Physical deposition	Sputtering DC / RF, Evaporation	
		Electron beam evaporation system	*LEYBOLD OPTICS*
⇒	Dry etching	Plasma and RIE mode	*SENTECH*
⇒	Bonding techniques	Anodic, Si-Si and Wire Bonding	
⇒	Cutting, grinding, polishing		*BÜHLER, D*
⇒	TEM sample preparation	plan-view and cross-section	
		including ion milling equipment	*GATAN, USA*

Services

The institute serves as a user center and technology transfer point in connection with its many years of experience in the application of ion beams for modification and analysis of solid surfaces and thin films of arbitrary materials.

Ion beam treatment of metallic materials (e.g. light metals like Al, Ti; stainless steel) can be advantageously applied for the improvement of the tribological properties (hardness, wear, corrosion resistance etc.). Using ion beam assisted deposition, hard coatings with special properties are obtained, such as a high adhesive strength and low internal stress. New technologies of high energy ion implantation or focused ion beam techniques result in new applications of electronic devices or microintegrated circuits.

Ion beams are an excellent instrument for the analysis of solid state surfaces. The interaction of the incident ion beam with the surface layer of a material leads to a specific radiation response, which yields information on the elemental composition as function of depth in a quantitative and essentially non-destructive way.

Additional means of preparation and diagnostics are available to fulfill the needs of users from different industrial branches. Do not hesitate to contact our experienced team.

Main areas of competence:

- Development and fabrication of sensors and detectors for charged particle spectroscopy
- Deposition of functional coatings using ion-assisted physical vapor deposition
- Fabrication of wear protection layers on metallic materials or alloys
- Deposition of blood compatible layers (i.e. TiO_x) on different materials
- Ion implantation in a broad range of ion energy (~ 200 eV to ~ 50 MeV) and substrate temperature
- Advanced ion beam technologies (high energy ion implantation, focused ion beam) for microelectronic applications
- Application of high energy ion implantation for power devices and laser structures
- Doping of semiconductors, in particular wide bandgap semiconductors
- Surface analysis of solid materials with high energy ion beams
- Computer simulation of ion beam interaction with materials
- Optical characterization of materials (luminescence, FTIR, Raman)

Offers:

- Consultation and problem evaluation for ion beam applications
- Process development for ion beam treatment of different materials (metals, ceramics, semiconductors)
- Process development in ion-assisted deposition of thin films
- Preparation and treatment of material samples, tools or complex parts of devices
- Ion implantation and ion beam analysis services
- Ion implantation into semiconductor materials for applications in microsystems and micro- and power electronics,
- Preparation / fabrication of semiconductors or silicon radiation sensors under clean room conditions
- Structural diagnostics of materials surfaces including e-beam- (SEM, TEM, AES) and X-ray techniques (XRD, XRR with both Cu-K and Synchrotron (5-35 keV) radiation).

Examples:

- Improvement of wear resistance of austenitic stainless steels using plasma immersion ion implantation
- High energy ion implantation for power semiconductor devices,
- Micro- and nanoengineering with focused ion beams
- Non-destructive quantitative hydrogen analysis in materials

- Non-destructive ion beam analysis of art objects
- Doping of wide-bandgap-semiconductors (SiC, diamond)
- Nuclear microprobe for ion beam analysis with high spatial resolution
- Synchrotron radiation analysis of materials at the ROBL Beamline in Grenoble.

Contact:

Please direct your inquiry about the application of ion beams for modification and analysis of materials to one of the following experts:

Field of application	**Name**	**Phone / Fax**	**E-mail**
Ion implantation (metals, ceramics, polymers, biomaterials)	Dr. Edgar Richter	3326 / 2703	e.richter@fz-rossendorf.de
Ion implantation (semiconductors, in particular high energy)	Dr. Johannes von Borany	3378 / 3438	j.v.borany@fz-rossendorf.de
Thin film deposition	Dr. Andreas Kolitsch	3348 / 2703	a.kolitsch@fz-rossendorf.de
High energy ion beam analysis	Dr. Rainer Grötzschel	3294 / 2870	r.groetzschel@fz-rossendorf.de
Semiconductor preparation Detector / Sensor fabrication	Dr. Bernd Schmidt	2726 / 3285	bernd.schmidt@fz-rossendorf.de
Focused ion beams	Dr. Lothar Bischoff	2963 / 3285	l.bischoff@fz-rossendorf.de
Structural diagnostics	Dr. Johannes von Borany	3378 / 3438	j.v.borany@fz-rossendorf.de
Synchrotron radiation beamtime at ROBL (ESRF)	Dr. Norbert Schell	2367 / 2371	schell@esrf.fr
Optical materials characterization	Dr. Stephan Winnerl	2880 / 3285	s.winnerl@fz-rossendorf.de

For all phone/ fax-numbers choose the country / local code: ++ 49 351 260 (for FZR)
++ 33 47 688 (for ROBL)

The abbreviations are explained in the Glossary (see page 71).

The institute also recommends to visit the homepages of its spin-off companies

- "GeSiM mbH" www.gesim.de
- "APT Dresden" www.apt-dresden.de
- "nanoparc GmbH" www.nanoparc.de

Forschungszentrum Rossendorf e.V.

Institute of Ion Beam Physics and Materials Research (IIM)

Postfach 51 01 19
D-01314 Dresden

Tel.: 0351 260 2245
Fax: 0351 260 3285
www.fz-rossendorf.de

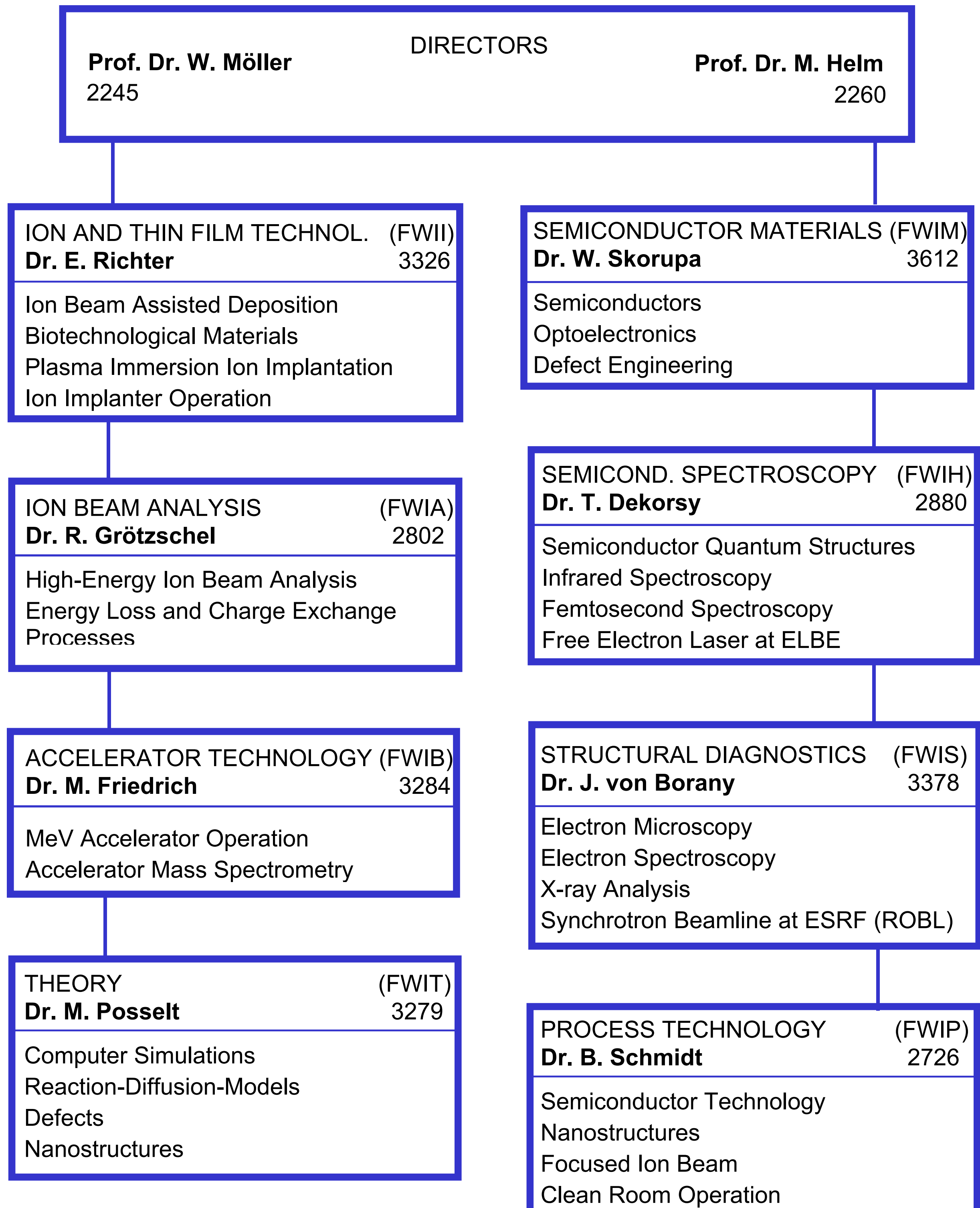

List of Personnel

Directors: Prof. W. Möller, Prof. M. Helm
Office: I. Heidel, S. Kirch

Scientific Staff:

Permanent:

Dr. L. Bischoff
Dr. J. von Borany
Dr. W. Bürger
Dr. T. Dekorsy
Dr. F. Eichhorn
Dr. S. Facsko
Dr. J. Faßbender
Dr. M. Friedrich
Dr. R. Gago
Dr. D. Grambole
Dr. J. Grenzer
Dr. R. Grötzschel
Dr. V. Heera
F. Herrmann
Dr. K.-H. Heinig
Dr. H.-U. Jäger
Dr. R. Kögler
Dr. A. Kolitsch
Dr. U. Kreißig
Dr. A. Mücklich
Dr. C. Neelmeijer
Dr. D. Panknin
Dr. M.T. Pham
Dr. M. Posselt
Dr. F. Prokert
Dr. H. Reuther
Dr. E. Richter
Dr. N. Schell
Dr. B. Schmidt
Dr. W. Skorupa
Dr. M. Voelskow
Dr. S. Winnerl

Post Docs:

V. Cantelli
Dr. M. Maitz
Dr. K. Potzger
Dr. J. Sun

Projects:

Dr. G. Abrasonis
W. Anwand
Dr. G. Brauer
A. M. Cardoso
Dr. N. Georgiev
M. Krenz
Dr. A. Lebedev
Dr. M. Mäder
R. Martins
Dr. T. Oates
M. Peikert
Dr. W. Pilz
Dr. A. Rogozin
Dr. M. Seidel
Dr. N. Shevchenko
Dr. H. Weishart
Dr. R. Yankov

PhD Students:

B. Abendroth
C. Akhmadaliev
M. Beckers
A. Dreyhaupt
H. Geßner
D. Güttler
D. Kost
M. O. Liedke
T. Müller
J. Potfajova
L. Röntzsch
S. Sinning
D. Stehr

Diploma Students:

R. Heller
R. Henry
M. Kreller
H. Lange
S. Menzel
S. Mucke
G. Voigtländer

Technical Staff:

Permanent:

R. Aniol
G. Anwand
W. Boede
K.-D. Butter
E. Christalle
H. Felsmann
K. Fukarek
B. Gebauer
H.-J. Grahl
G. Grunert
P. Hartmann
J. Haufe
G. Hofmann
S. Klare
J. Kreher
A. Kunz
U. Lucchesi
M. Mißbach
C. Neisser
E. Quaritsch
A. Reichel
B. Richter
M. Roch
B. Scheumann
G. Schnabel
A. Schneider
J. Schneider
A. Scholz
H. Seifert
K. Thiemig
S. Turuc
A. Vetter
A. Weise
J. Winkelmann
G. Winkler
I. Winkler

Projects:

F. Ludewig
T. Schumann
M. Steiner
I. Skorupa